FACULTY OF SCIENCE
UNIVERSITY OF COPENHAGEN

Master's thesis

Cavity Enhanced Spectroscopy on Ultra Cold Atoms

Martin Romme Henriksen

Niels Bohr Institutet
August 2014

Cavity Enhanced Spectroscopy on Ultra Cold Atoms

Prepared by
Martin Romme Henriksen

Academic advisor
Jan W. Thomsen

Quantum Optics and Ultracold Atoms Group
Niels Bohr Institute
University of Copenhagen
Blegdamsvej 17
DK-2100 København Ø
Denmark

Abstract

The stability of the current state of the art optical atomic clocks are limited due to the frequency noise of the interrogation oscillator. The low linewidth of such an interrogation oscillator is currently achieved by locking to an optical reference cavity. The improvement of the reference cavity's linewidth is associated with great technical difficulties, where cryogenic cooling and vacuum systems are used [1]. This work describes a set-up where the possibilities of using cavity enhanced FM spectroscopy of ^{88}Sr to produce an error signal is investigated. In this strongly coupled atom-cavity system we observe motion-dependent non-linear dispersion. So far we have not yet seen evidence of collective effects, i.e. where the atomic dipoles synchronise. An extensive analysis of the so-called NICE-OHMS detection technique is given, and a procedure for absolute atomic induced phase measurement is found. The development of a ECDL system and a laser shutting system is also presented.

Resumé

Stabiliteten af de aktuelt bedste optiske atomure er begrænset på grund af frekvensstøj i ures oscillator. Oscillatorens smalle linjebredde bliver i disse systemer opnået ved at låse frekvensen til en optisk kavitet. Forbedringer af sådanne kaviteter er forbundet med store tekniske vanskeligheder, hvor både kryogenisk nedkøling og vakuumkamre bliver brugt [1]. Denne afhandling omhandler et system hvor kavitetsforstærket FM spektroskopi af ^{88}Sr blive undersøgt. Dette med henblik på at generere et signal der kan bruges til at låse frekvensen af en oscillator. I vores system observerer vi hastighedsafhængige ikke-lineær dispersion. Vi har dog ikke observeret tegn på kollektive effekter baseret på synkronisering af atomers dipoler. Der er i denne afhandling også givet en grundig gennem gang af den såkaldte NICE-OHMS teknik og jeg finder en metode til at måle den absolutte atominducerede fase. Udviklingen af et ECDL-system og af et system til at blokere laserstråler er også beskrevet.

Acknowledgments

First I would like to thank my supervisor Jan W. Thomsom for the great effort he has put into my master's project from day one. It has truly been a joy to work with a highly enthusiastic physicist. Jan has together with my co-workers in the laboratory, Bjarke Takashi Røjle and Stefan Alaric Petersen, created an inspirational and interesting work environment. Bjarke, who is a Ph.D. student in the group also deserves a great thanks for all his guidance and patience when ever it was needed.

During my past year I have collaborated a great deal with the technicians at the Niels Bohr Institute. I would especially like to thank Axel Boisen and Jimmy Cali Hansen for always having an open door and a cheerful comment (and occasionally cake!).

More specificity in relation to this thesis, I would like to thank Julie Trope Hansen and Laurits Nielsen for their help with proofreading. Last, and in this case least, I have to thank Christoffer Dahl-Jørgensen for his always entertaining interpretation of the Doppler effect.

Contents

List of Figures

Lidt of Abbreviations

ADC	Analogue to Digital Converter.
AOM	Acousto-Optic Modulator.
DAC	Digital to Analogue Converter.
ECDL	External Cavity Diode Laser.
EOM	Electro-Optic Modulator.
FSR	Free Spectral Range.
FWHM	Full Width Half Maximum.
GPS	Global Positioning System.
GT	Glan-Thompson.
MOT	Magneto-Optical Trap.
NICE-OHMS	Noise-Immune Cavity-Enhanced Optical Heterodyne Molecular Spectroscopy.
OBE	Optical Bloch Equations.
PGA	Programmable Gain Amplifier.
PM	Photo Multiplier.
QED	Quantum Electrodynamics.
RF	Radio Frequency.
ULE	Ultra Low Expansion.
VCO	Voltage Controlled Oscillator.

Chapter 1

Prologue

1.1 Introduction

The keeping of time has been of great interest to society and its industrial evolution since sailors set off in search of new trade routes across the great oceans. Back then sailors face a problem of navigating at sea, since the only way to navigate was by looking at the stars, which only provided information about their latitude. In the year 1530 Regnier Gemma Frisius from the Netherlands is the first to propose using a precise clock to find ones longitude. In his book he writes [2]:

> "... it must be a very finely made clock which does not vary with change of air."

In 1567 king Philip II of Spain is the first to offer a reward for a method to solve the longitude problem. In 1714 the British Government offers a similar reward and in 1765 the carpenter John Harrison succeed in creating a clock precise enough to collect the price. This was achieved by making the arm of the pendulum of two different metals, in such a way that the difference in the thermal expansion coefficients canceled out, resulting in a frequency reference unaffected by temperature change. The development of precise frequency standards is thus a field of study that began in the 16th century and still continues today.

Frequency standards are generally characterized by two parameters. Accuracy and stability. Accuracy describes how large the deviation of a frequency is with respect to some reference frequency. It is a measure of how well the frequency can be reproduced. For a clock maker making pendulum clock, the accuracy depends upon how large a deviation the length of his pendulum arm has and thus how great a deviation the frequency of the pendulum has compared to other clocks. Stability says something about how the frequency changes over time, also called precision. It is a measure of how well you can predict the frequency some time into the future, or in the clock makers point of view, how much does the pendulum-arms length change over time. One way this can be illustrated is as F. Riehle has done in [3]. This is shown in figure 1.1.

Precise clocks are still used in navigation, though it is not in regard to the longitude problem. Today atomic clocks are used in the satellites that make up the Global Positioning System (GPS). Here they are used to synchronize the signals being broadcast to earth, making it possible for a ground receiver to calculate the difference in distance to several satellites.

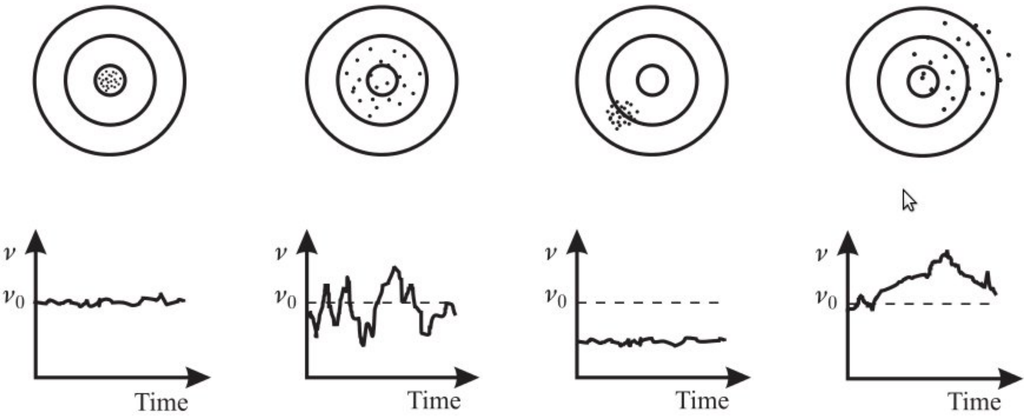

(a) *Precise and accurate.* (b) *Not precise but accurate.* (c) *Precise but not accurate* (d) *Not precise or accurate.*

Figure 1.1: *Illustration of the terms precision and accuracy. Taken from [3].*

1.1.1 The Atomic Clock

Every clock can be simplified down to two things, a local oscillator and a counter. Starting on a large scale we have the earth orbiting around the sun. The oscillator in this case is the earth oscillating with a frequency of 1/year. Or we can have the earth's own revolution as the oscillator, where the frequency would be 1/day. In these cases we would see ourselves as being the counter by keeping track of how many year ago Jesus was born or by ripping a day off the calender. In a pendulum clock the pendulum is the oscillator swinging from one side to the other once a second, and the clockwork and indicators are counting the time. The pendulum clock, so to say, divides up time into pieces of one second by keeping track of where the pendulum is. In our hankering for more precise timekeeping the pendulum begins to fall short. By only dividing time up in pieces on the order of one second, it becomes difficult to precisely measure the stability of our clock without measuring for a very long time. Imagine splitting up time into smaller and smaller pieces using the same pendulum frequency. Already at a tenth of a second it becomes very difficult to relate the pendulums position to this timespan. It will likewise become very difficult to measure on the timescale of milliseconds because it becomes difficult to keep track of the pendulums position. But what if we had a pendulum that was swinging 1000 times in a second or even 10^9 times in a second. It is here the atom comes into the picture. By using the electrons' transitions between two energy levels in an atom as an oscillator, thus dividing the second into even smaller pieces, there is a possibility to reach several hundreds of terahertz of oscillation frequency.

In 1967 it was decided that the ^{133}Cs atom should be a primary frequency standard and the second was redefined [4]:

> "The second is the duration of 9 192 631 770 periods of the radiation corresponding to the transition between the two hyperfine levels of the ground state of the caesium 133 atom".

As of today the precision of Cs clocks has reached the order of 10^{-16} fractional level at one second of integration time. This corresponds to knowing what time your clock will show 30 millions years in the future with an uncertainty of one second.

The current state-of-the-art microwave atomic clock uses cryogenically cooled

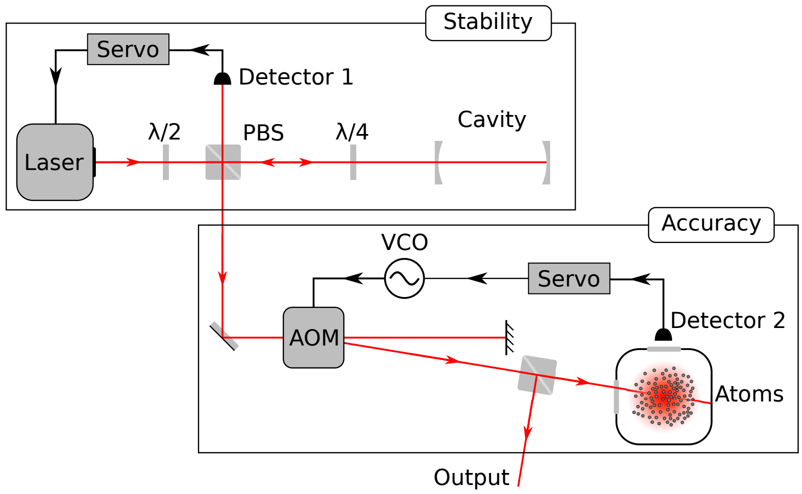

Figure 1.2: *Basic schematic of a stabilization and accuracy scheme for a local oscillator. The laser light is split up into two using a polarizing beamsplitter (PBS), one part interacts with a cavity and is reflected dependent on how close to resonance the light and cavity is. The frequency of the laser is then corrected according to the intensity on detector 1 which insures a precise frequency. The second part of the light through the PBS continues through an AOM that shifts the frequency of the light according to a signal from a VCO. The frequency shifted light through the AOM is directed at atoms where Detector 2 registers the scattering of the light if at resonance. Via a servo the VCO is adjusted so that the final output is always on resonance with the atoms and in that way accuracy is achieved.*

high finesse cavities to generate laser light with high stability and uses atoms to achieve high accuracy [1, 5]. Figure 1.2 shows a schematic of a basic set-up of a local oscillator. The idea is to lock the laser to a cavity with a very low linewidth in such a way that the laser stays on resonance with the cavity. By constantly pulling the laser frequency towards the cavity's resonance, the linewidth of the laser will decrease if the servo system is fast enough. This leads to a high stability or precision. To ensure that a clock in Denmark and a clock in Japan is actually counting based on the same oscillator frequency, the laser light is subsequently locked to an atomic transition. Based on the assumption that, for example, all Cs atoms in the universe are identical, this ensures a high accuracy dependent on the natural linewidth of the atomic transition. At the present time there are prospects for other atoms to become primary frequency standards. This is based on the argument made earlier, that the higher the frequency the greater the potential for a precise measurements. The energy levels used in Cs corresponds to frequencies in the microwave range (gigahertz), so by using atoms that have a level structure allowing for interaction in the optical domain, a significant improvement is possible. There is however a limit to how precise a frequency that can be achieved. In studying quantum mechanics theorists have predicted a lower limit called the quantum noise limit. This in turn leads to maximum achievable stability.

To achieve the ultimate stability, future optical clocks will have to produce a light source with frequency stability at 10^{-17} fractional level or below at 1 second of interrogation time. In order to achieve this, a number of technical challenges has be overcome. This being frequency noise due to the Dick effect and Brownian thermal noise of the reference cavity mirrors. Recently, a stability at the lower 10^{-16} fractional level has been achieved by using a cavity constructed from single silicon

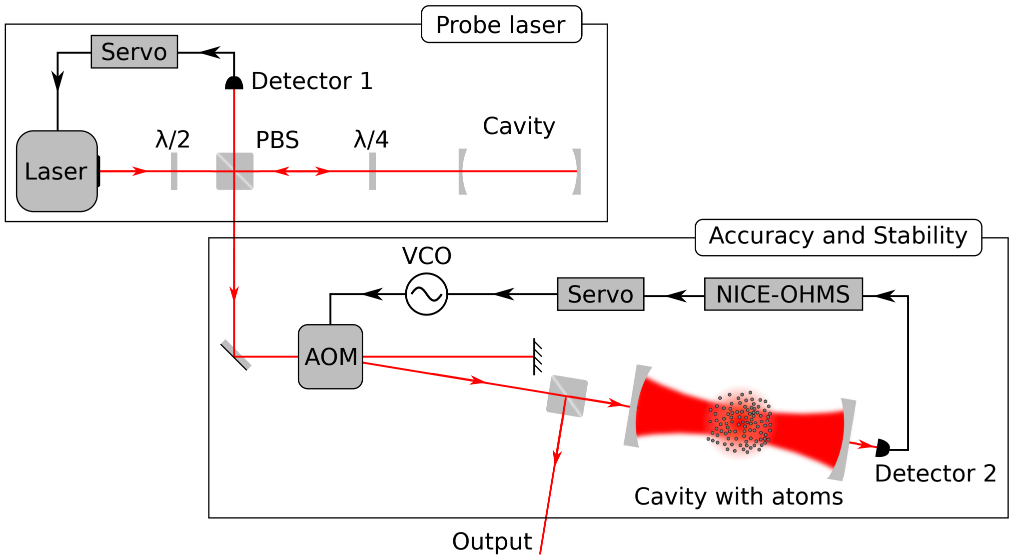

Figure 1.3: *Basic schematic of a stabilization and accuracy scheme for a local oscillator. Compared to figure 1.2 the stability is now achieved by interrogating a narrow linewidth optical transition of atoms. This is done through phase detection of the cavity transmitted light using a noise canceling technique called NICE-OHMS.*

crystal, which has been placed in a vacuum and cryogenically cooled to 124 K [1].

1.1.2 This Thesis

The work this thesis is based on follows the work of M. J. Martin, D. Meiser, J. W. Thomsen, Jun Ye and M.J. Holland [6], where a stabilization scheme using ultra narrow optical transitions of atoms placed in a cavity is proposed. The idea is to use an ultranarrow atomic transition to achieve both stability and accuracy using many-atom cavity Quantum Electrodynamics (QED). A basic schematic of such a set-up is shown in figure 1.3. Going from the set-up shown in figure 1.2 to the setup shown in figure 1.3, greatly reduces the requirements for the cavities because the atomic linewidth will dominate the system. Doing spectroscopy on an ultra narrow transition will cause an almost unavoidable saturation of this transition, but through the application of a cavity the atoms experiences collective interaction, which should enhance the slope of the dispersion signal [6] making it ideal for a very tight locking scheme. This signal is produced by means of the so-called Noise-Immune Cavity-Enhanced Optical Heterodyne Molecular Spectroscopy (NICE-OHMS) technique [7], which is a technique that provides a superior signal-to-noise ratio through detection of the phase shift caused by an atom cloud in a cavity. It is thus possible to interrogate very narrow atomic transitions as the atom-light interaction is enhanced by an order of the finesse.

The goal of our set-up however, is not to make an atomic clock. It is a pure atomic spectroscopy set-up for the purpose of investigating an atom-cavity system and trying to understand what processes are happening and how best to utilize them in future set-ups. We investigate different parameters for the purpose of generating an error signal for a future locking scheme utilizing an ultra-narrow optical transition in strontium.

1.2 Thesis Outline

The thesis is organized as follows. In chapter 2 I discuss of the elements in the experimental set-up. The level structure and characteristics of the Strontium atom is described. A review of the cooling and trapping mechanisms used is given. The cavity used to perform the cavity enhanced spectroscopy is described along with the Hänsch-Couillaud locking scheme. The laser system used to interrogate the atoms is stabilized using the Pound-Drever-Hall locking technique. The implementation of this technique is described along with a characterisation of the laser system's frequency stability though a calculation of the Allan deviation.

In chapter 3 I present the developments I have made to the experimental set-up. Among these are an ECDL with a digital temperature controller, different laser shutting techniques and a discussion of a set-up to digitally control the AOMs in the experimental set-up.

In chapter 4 I present a detail description of the spectroscopy technique used. This is done from two different perspectives as to gain the a clear picture of what we actually measure. On the bases of the what is found in chapter 4, chapter 5 present the measured data along with theoretical considerations. A discussion of the consequences of having a thermal system is given, along with considerations of whether collective effects are present in the atom-cavity system.

Chapter 2

Experimental Setup

The key part of the experiment is the atoms and taking a look at the experimental set-up it can be seen that a majority of the components that form the set-up plays a part in cooling and trapping the atoms. Figure 2.1 shows a simplified layout of the general set-up, where an oven heats up a lump of Strontium, releasing atoms into the vacuum chamber. The atoms high thermal velocity is slowed down in the Zeeman slower making it possible to trap and cool them in a Magneto-Optical Trap (MOT). Spectroscopy is then preformed with light from a probe laser stabilized to an Ultra Low Expansion (ULE) cavity. As it is a very narrow transition being probed, the atom-light interaction is rather difficult to detect. By using a cavity around the trapped atoms, the interaction is enhanced by an order of the cavity finesse.

The first part of this chapter describes the ^{88}Sr atoms chosen for this experiment, starting with why they are interesting. A review of the techniques used to cool and trap the atoms is also given. Following this is a section on the cavity which makes it possible to perform the atomic spectroscopy. The spectroscopy is done by probing the atoms with laser light. This laser system is also described. Finally the detection scheme used to obtain the spectroscopy data is described.

2.1 The Atoms

As mentioned in the introduction the goal is to make a locking scheme for an ultra narrow laser source by the use of cavity enhanced spectroscopy on atoms. By introducing atoms with a narrow transition into a cavity, the atomic linewidth will dominate the system. The choice of ^{88}Sr atoms was made because of the ultra narrow ^{1}S$_0$ - ^{3}P$_1$ intercombination line at 689 nm (Γ = 7.6 kHz) and because the cooling transition can be driven by commercial available diode lasers using well known technologies.

2.1.1 Strontium

The energy levels of ^{88}Sr of interest are shown in figure 2.2 and described by the Russell-Saunders notation of $^{2S+1}L_J$, where S is the total spin of the electrons being either 0 or 1, L is orbital angular momentum ($S = 0,\ P = 1,\ D = 2$) and J is the total angular momentum of the state. The ^{1}S$_0$ - ^{1}P$_1$ transition marked as 1 on figure 2.2 is the transition that is used for cooling and trapping. A problem arises because the $5s4d\ ^1$D$_2$ energy level is located below the $5s5p\ ^1$P$_1$ level, which results in a decay first to the ^{1}D$_2$ and subsequently to the metastable $5s5p\ ^3$P$_1$ and $5s5p\ ^3$P$_2$

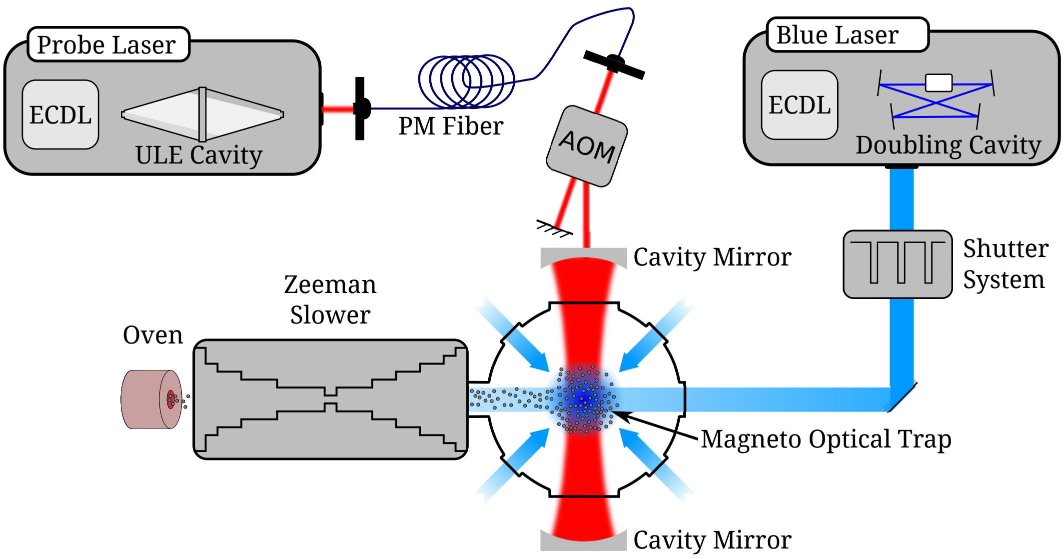

Figure 2.1: *The general experimental set-up consisting of an oven, Zeeman slower and a MOT. The blue laser used to cool and trap is generated by frequency doubling of an infra-red ECDL. Cavity spectroscopy is perform on the atoms with a Probe laser stabilized to a ULE cavity.*

1	$\Delta J = 0,\ \pm 1$	$(J = 0 \ll\neq\gg J' = 0)$
2	$\Delta M_J = 0,\ \pm 1$	$(M_J = 0 \ll\neq\gg M_{J'} = 0$ if $\Delta J = 0)$
3	Parity changes	
4	$\Delta l = 0,\ \pm 1$	One electron jump
5	$\Delta L = 0,\ \pm 1$	$(L = 0 \ll\neq\gg L' = 0)$
6	$\Delta S = 0$	

Table 2.1: *Selection rules for electric dipole transitions in the LS-coupling scheme [9].*

levels. This is a problem because the atoms populated in these levels can not be cooled and the atoms will be lost, as the $^1S_0$ - $^1P_1$ transition can not be driven. In [8] they report that the trap loss rate per atom populated in $^1P_1$ level is $\approx 1.29 \times 10^3$ s^{-1}.

The transitions 3 and 4 occur despite the selection rules for electric dipole transitions (see table 2.1), though with a very low decay rate. It is clear to see that the $^1S_0$ - $^3P_2$ transition and the $^1S_0$ - $^3P_0$ transition are double forbidden according to rule 1 and 6 in table 2.1, whereas the $^1S_0$ - $^3P_1$ only contradicts rule 6. This leading to the conclusion that the decay rate for the $^1S_0$ - $^3P_1$ transition is the highest of the three. By driving transition 5 and 7, the population decay from the ^3P levels can be drastically increased thereby decreasing the loss of atoms from the trap. The transitions (5) and (7) are called the repumper transitions as they are used to pump atoms from the metastable states to the ground state through the $^3P_1$-state.

The transitions forbidden by the selection rules can occur due to the spin-orbit interaction of the electron. The spin-orbit interaction is caused as the magnetic field of the nucleus exerts torque on the magnetic dipole moment of the spinning electron. This breaks down the spin symmetry and allows transitions other than $\Delta S = 0$ transitions. These weakly allowed transitions are called intercombination lines. The 689 nm $^1S_0$ - $^3P_1$ intercombination line has a linewidth of 7.6 kHz making it ideal

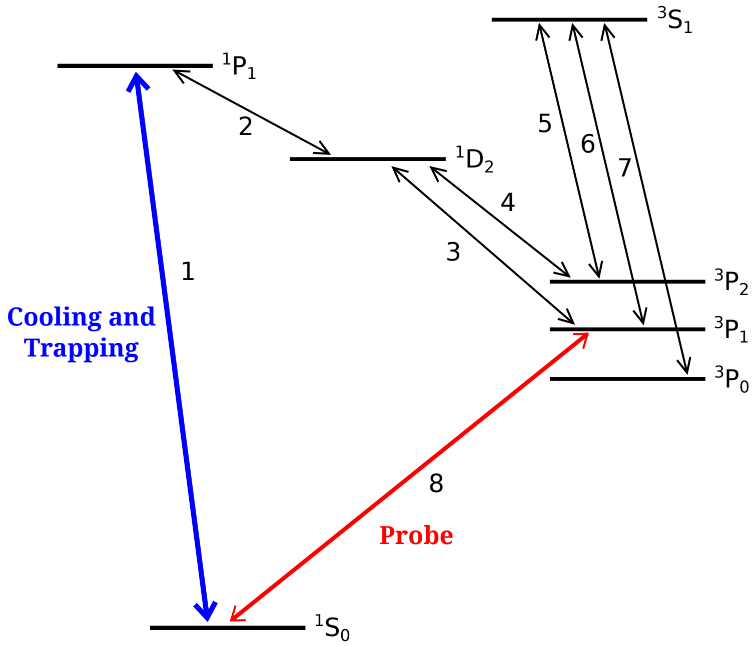

Figure 2.2: *^{88}Sr energy level structure. The $^1S_0$ - $^1P_1$ transition (blue) is used for cooling and trapping the atoms. The $^1S_0$ - $^3P_1$ transition (red) is the probing transition that is on resonance with the cavity. The transitions are numbered in accordance with the values given in table 2.2.*

as a transition for a proof-of-concept set-up for optical clock purposes.

2.1.2 Magneto-Optical Trap

The strontium source for the experimental set-up is placed in an oven where it is heated to about $T \approx 550$ °C producing a jet of strontium atoms exiting from a small hole. The atoms in the jet have a speed determined by the 3D Boltzmann speed distribution

$$f(v) \propto e^{-\frac{m(v_x^2+v_y^2+v_z^2)}{2k_B T}}. \tag{2.1}$$

Here k_B is the Boltzmann constant and m is the mass of the atom. It is reported in previous work [10], that also describes this set-up, that the most probable speed of

No.	λ [nm]	A [s^{-1}]
1	460.73	2.01×10^8
2	6500	3.9×10^3
3	1800	6.6×10^2
4	1900	1.34×10^3
5	707.0	4.2×10^7
6	687.8	2.7×10^7
7	679.1	8.9×10^6
8	689.3	4.69×10^4

Table 2.2: *The transition wavelength and decay rates for the energy levels shown in figure 2.2.*

the atoms was found to be $\approx 400\ \frac{\mathrm{m}}{\mathrm{s}}$. This high speed relative to the laboratory give rise to a number of inconvenient effects.

In the experimental set-up the propagation direction of the jet of atoms is perpendicular to the cavity, meaning that the largest velocity component of the atoms is perpendicular to the interrogating field. Given a cavity waist of d and an atomic velocity of v, there is a limit on the light-atom interaction time $\tau = \frac{2d}{v}$, resulting in a transit-time frequency broadening $\Delta\nu_{tt} \approx \frac{1}{\tau} = 40$ kHz for our set-up, which is large compared to 7.6 kHz of the $^1\mathrm{S}_0$ - $^3\mathrm{P}_1$ transition, we are interested in.

The atoms speed parallel to the cavity also pose a problem due to the Doppler shift given by

$$\omega_0' = \omega_0 + \mathbf{k} \cdot \mathbf{v}, \tag{2.2}$$

where ω_0 is the angular frequency ($\omega = 2\pi\nu$) of the atomic transition in the atoms' rest frame, $\mathbf{k}$ is the cavity field's wave vector, $\mathbf{v}$ is the atoms' velocity with respect to the cavity and ω_0' is the angular frequency of the atomic transition in the cavity's rest frame. Hence, when measuring a transition in a thermal gas of atoms, it is ω_0' that will be measured.

In addition to the frequency shift, the Doppler effect also leads to a linewidth broadening. This is due to the velocity distribution described by the Boltzmann distribution (eqn. (2.1)), that in turn gives a distribution of Doppler shifts resulting in a Gaussian frequency response. This is called Doppler broadening. The Doppler broadened linewidth is given by (Full Width Half Maximum (FWHM))

$$\frac{\Delta\nu}{\nu_0} = 2\sqrt{\ln(2)}\frac{v_0}{c}, \tag{2.3}$$

where $v_0 = \sqrt{2k_B T/M}$ for an atomic mass M and a temperature T.

In order to fully exploit the ultra narrow linewidth of the strontium atoms, these broadening effects have to be minimized. This is achieved by cooling and trapping the atoms using laser cooling. This technique uses radiative forces to slow, trap and cool the atoms.

Scattering Force

Consider a neutral atom with mass m and momentum $\mathbf{p}$ in a monochromatic field with an angular frequency ω. The atom-light interaction is described by a single closed atomic transition between the ground state $|g\rangle$ and the exited state $|e\rangle$ with a transition frequency of ω_0 and a lifetime of $1/\Gamma$. The momentum vector of the atom $\mathbf{p}$ and the wave vector of the field $\mathbf{k}$ are parallel and opposite.

Whenever a photon is absorbed by an atom, the atom's momentum is changed as the total momentum in the system must be conserved. The atoms momentum is thus changed by

$$\Delta\mathbf{p} = \hbar\mathbf{k} \tag{2.4}$$

When an atom in the exited state spontaneously emits a photon the momentum change is reversed. However, the direction of the momentum change is randomly distributed over all possible directions, so for a large number of scattering events the total momentum change from spontaneous emission averages out to zero. The magnitude of the scattering force is thus equal to the rate at which the light field transfers momentum to the atom:

$$\mathbf{F}_{scat} = \mathbf{p}_{photon} R_{scat}. \tag{2.5}$$

Here the scattering rate can be described as $R_{scat} = \Gamma\rho_{ee}$ where ρ_{ee} is the fraction of the population in the exited state given by ([9] sec. 7.5.2)

$$\rho_{\mathbf{ee}} = \frac{\Omega^2/4}{\delta^2 + \Omega^2/2 + \Gamma^2/4}. \tag{2.6}$$

Here δ is the frequency detuning between the atomic transition ω_0 and the light field ω. δ is chosen in such a way that the Doppler shift is counteracted $\delta = \omega - \omega_0 + \mathbf{k}\cdot\mathbf{v}$. The Rabi frequency Ω can be described by the relation $\Omega^2 = \frac{\Gamma^2 I}{2I_{sat}}$, where I is the field intensity and I_{sat} is the atomic transition's saturation intensity given by [9]

$$I_{sat} = \frac{\pi hc}{3\lambda}\Gamma. \tag{2.7}$$

Combining equation (2.5), (2.6) and (2.7) gives a scattering force on the atoms as

$$\begin{aligned} \mathbf{F}_{scat} &= \mathbf{p}_{photon} \times \frac{\Gamma}{2}\frac{I/I_{sat}}{1 + I/I_{sat} + 4\delta^2/\Gamma^2} \\ &= \hbar\mathbf{k}\frac{\Gamma}{2}\frac{I/I_{sat}}{1 + I/I_{sat} + 4\delta^2/\Gamma^2}. \end{aligned} \tag{2.8}$$

Detuning by the Zeemann Effect

As can be seen in equation (2.8) the force slowing the atoms will depend on the atom's velocity through the detuning parameter δ due to the Doppler effect. To slow atoms over a large velocity range it is thus required to apply a ramp of detunings. Changing the light field frequency will result in a non-continuous slowing process, as one would need a time-varying detuning. If you instead made the atomic transition frequency position dependent, the same light field could slow atoms throughout the speed distribution.

By applying a magnetic field the energy levels corresponding to different angular momenta of the electron M_J, splits up. The $^1P_1$ level of the cooling transition splits up into 3 energy levels, one for each value of $M_J = 0, \pm1$, so that the energy differences between $^1\mathrm{S}_0$ and $^1\mathrm{P}_1$ levels are given by

$$\begin{aligned} \Delta E &= E_0 + E_{ZE} \\ &= E_0 + g_J\mu_B B M_J, \end{aligned} \tag{2.9}$$

where B is the magnetic field, μ_B is the Bohr magnetron and g_J is the Landé g-factor given by

$$\begin{aligned} g_J &= \frac{3}{2}\frac{S(S+1) - L(L+1)}{2J(J+1)} \\ &= \frac{3}{2}\frac{0(0+1) - 1\cdot(1+1)}{2\cdot1\cdot(1+1)} = 1, \end{aligned} \tag{2.10}$$

The angular frequency of the atomic transition is then defined by the magnetic field

$$\begin{aligned} \omega_{ZE} &= \frac{(E_0 + E_{ZE})}{\hbar}, \\ &= \omega_0 + \frac{\mu_B B M_J}{\hbar}. \end{aligned} \tag{2.11}$$

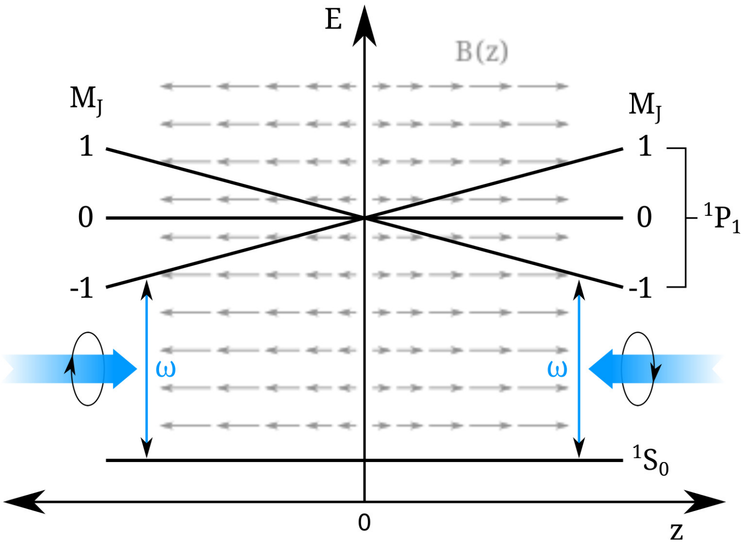

Figure 2.3: *An illustration of the energy levels in a one dimensional MOT. The magnetic field B increases in opposite directions with the distance z to the centre. The helicity of the light ensures that scattering only happens when the atomic transition is perturbed by the magnetic field.*

This means that instead of time-varying atom-light detuning, a spatial varying detuning is possible. By having an increasing magnetic field along the atoms propagation axis, the atom are subject to changing energy shifts of the $M_J \neq 0$ levels, as they move through the magnetic field. If the light field is left-handed circular polarised, momentum conservation ensures interaction only with the $M_J = -1$ level. The detuning can thus be spatially controlled by modelling the magnetic field, making it possible to continuously slow the atoms. This set-up is called a Zeeman slower.

The Trap

Going from slowing atoms to trapping them is in a way just a question of extending the slowing scheme so that the atoms are slowed from all directions. Setting the magnetic field to zero at the trap centre and having it increase in opposite directions as the distance to the trap centre grows, will result in the negative shift to the $^1P_1$ $M_J = -1$ level if the atoms moves to either side. Having counter-propagating beams tuned below the atomic resonance with the same polarization with respect to the k-vector, will result in a scattering force pushing the atoms towards the trap centre. The magnetic field sets the quantisation axis of the atoms to always be parallel and opposite to the laser beam that applies a force towards the trap centre. Thus it is a requirement that the counter-propagating beams have polarity of identical helicity. The laser beam coming in from the right will in this way, due to the circular momentum of the photons, interact with the $M_J = -1$ level only when the magnitic field is opposite in direction to the photons. The atoms to the left of the trap centre can only interact with photons from the right through the $M_J = 1$ level, which is far off resonance. This geometry is illustrated in figure 2.3.

This one dimensional scheme can easily be expanded to three dimensions. The magnetic field is created by the so called anti-Helmholtz coils consisting of two coils with currents running opposite thus generating opposite magnetic fields which cancels out at the centre. At small distances from the centre the atoms will experience a

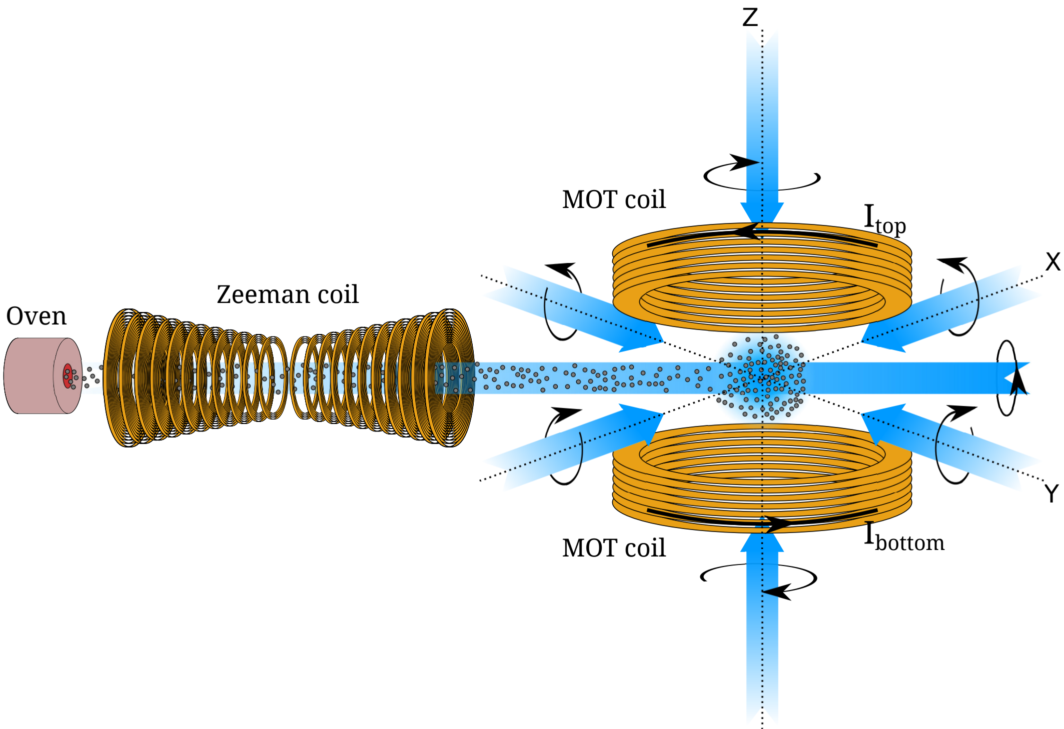

Figure 2.4: *An illustration of a combined Zeeman slower and MOT set-up. The blue beams parallel to the x, y and z axes are the MOT beams. The beam going through the Zeeman coils is the Zeeman slower beam.*

linear increase in the magnetic field strength. This comes from the Maxwell equation $\nabla \cdot \mathbf{B} = 0$ that imply [9]

$$\frac{\mathrm{d}B_x}{\mathrm{dx}} = \frac{\mathrm{d}B_y}{\mathrm{dy}} = \frac{1}{2}\frac{\mathrm{d}B_z}{\mathrm{dz}}.$$

Having counter-propagating beams in both the x, y and z direction will thus make a stable trap capable of cooling atoms to milli-Kelvin temperatures at the trap centre. Figure 2.4 shows a simple illustration of a Zeeman slower and MOT set-up.

The Zeeman slower has to reduce the atoms speed towards the MOT down below the limit where the Doppler shift is less than the cooling transition's width. If the atoms are moving too fast as they come into the MOT, they will be too far from resonance with the MOT beams due to Doppler shift. This means that the scattering force trapping the atoms will be insufficient making MOT unable to trap the atoms. This leads to a maximum capture velocity given by [9]

$$\mathbf{v}_c \leq \frac{\Gamma}{\mathbf{k}}. \tag{2.12}$$

Another important parameter to consider is the saturation intensity given in equation (2.7), which gives the required intensity of the MOT beams for cooling and trapping. It also has this relation to the Rabi frequency:

$$\frac{I}{I_{sat}} = \frac{2\Omega^2}{\Gamma^2}. \tag{2.13}$$

This relation shows that at saturation, the Rabi frequency is comparable with Γ.

When describing a MOT one typically considers some cooling limits. The Doppler limit is the minimum temperature that can be achieved due to the random direction of the spontaneous emission. At the very low end of the energy scale these random kicks give rise to a motion analogous to Brownian motion of microscopic particles. The Doppler limit is given by [9]

$$T_D = \frac{\hbar\Gamma}{2k_B} \tag{2.14}$$

which for the ^{88}Sr using the ^{1}S$_0$ - ^{1}P$_1$ transition is $T_D \approx 0.77$ mK.

Methods for sub-Doppler cooling have been developed and cooling to temperatures below the Doppler limit have been achieved for alkali metals. At these energy scales the recoil of the photon on the atom set a new limit called the recoil limit. This is given by the mass of the atom m and wavelength of the cooling light λ [9]:

$$T_r = \frac{h^2}{m\lambda^2 k_B}. \tag{2.15}$$

This, however, is not a limit we are concerned with, as sub-Doppler cooling of alkali earth atoms such as Strontium only recently has been proven experimentally possible [11].

In the experimental set-up the MOT light is detuned by 35 MHz and the combined intensity of the MOT beam is on the order of $I/I_{sat} \approx 0.17$. With these parameters a temperature of 3 mK has been measured. This was done by time of flight measurements as described in [10].

The Number of Atoms

The number of atoms in the MOT is estimated by measuring the MOT fluorescence using a Photo Multiplier (PM). The PM is placed as shown in figure 2.5. The optical power incident on the PM is related to the PM voltage signal through calibration factor η.

$$P_{PM} = \eta U_{PM} \tag{2.16}$$

This calibration factor has been found by mapping out the PM signal to known optical powers. The optical power emitted from the MOT is the photon scattering rate times the photon energy

$$P_{MOT} = N\rho_{ee}\Gamma\hbar\omega \tag{2.17}$$

where N is the number of atoms, ρ_{ee} is the fraction of atoms in the exited state and $\hbar\omega$ is the energy per photon. As in equation (2.8) ρ_{ee} is given by the intensity of the MOT beams, the saturation intensity and the atom-light detuning. It is only a fraction of the scattered photons that reaches the PM, so the optical power measured by the PM will be

$$P_{MOT} = N\rho_{ee}\Gamma\hbar\omega L_{window}^2 \frac{2\pi r^2}{4\pi R^2} \tag{2.18}$$

where L_{window} is loss due to the vacuum chamber window surfaces. Putting all this together results in an expression for the estimation of the number of atoms in MOT.

$$N = \frac{\eta U_{PM}}{\rho_{ee}\Gamma\hbar\omega L_{window}^2 \left(\frac{r}{2R}\right)^2} \tag{2.19}$$

Typical values for this setup have 3 mW/cm^2 in each MOT beam giving $I = 6 \times 3$ mW/cm^2 and a detuning of $\delta = 35$ MHz, producing a PM signal around 600 mV which corresponds to $N \approx 10^8$ atoms.

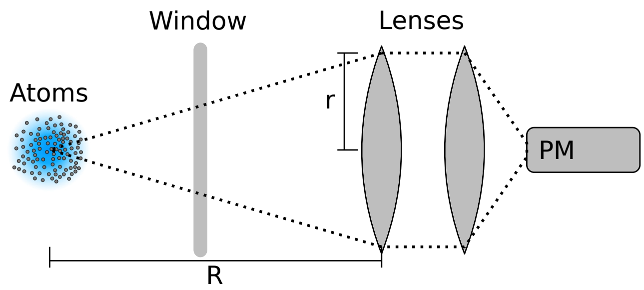

Figure 2.5: *A PM measures the MOT fluorescence through a window in the vacuum chamber.*

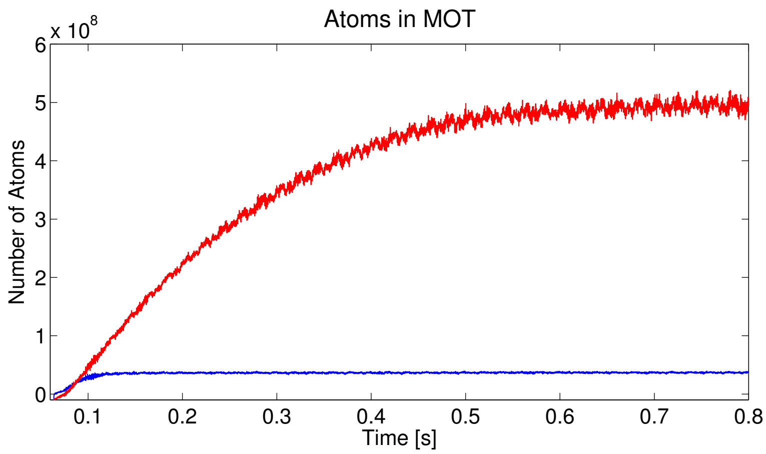

Figure 2.6: *The number of atoms in a MOT with repumpers (red) and without (blue). The MOT beams are turned on at $t = 0$. The gain in atom number from applying repumpers is a factor of 13.4.*

Repumpers

As described earlier the ^{88}Sr level structure (see fig. 2.2) is such that when cooling on the $^1S_0$ - $^1P_1$ transition there is a probability that the atoms decay into the metastable $^3P_2$ level, which means the cooling transition can not be driven and the atoms are lost from the trap. By exciting these atoms from the $^3P_2$ level to the $^3S_1$ level using a 707 nm laser, the $^3P_2$ level can effectively be emptied into the $^3P_1$ level where it then decays into the ground state and into the $^3P_0$ level which is also metastable. Applying another laser at 679 nm this level can likewise be emptied through the $^3S_1$ level and in that way ensuring that all atoms are pumped back into the ground state where they can be cooled. It is clear from looking at the level structure that only applying the 679 nm laser will not have any effect since the $^1D_2$ level can not decay into the $^3P_0$ level. Only applying the 707 nm laser will have an effect but there will still be a significant loss due to decay from the $^3S_1$ level to the $^3P_0$ level.

In figure 2.6 the number of atoms in the MOT is shown starting as the cooling beams are turned on. The plot shows data for both a MOT with the repumper lasers and a MOT without the repumper lasers. The number of atoms is estimated by the method described above. It is clear that the repumper lasers have a vary big effect on the number of atoms in the trap, as the number goes from $\approx 3.6 \times 10^7$ atoms without repumping and up to $\approx 4.9 \times 10^8$ atoms with repumping. The gain factor

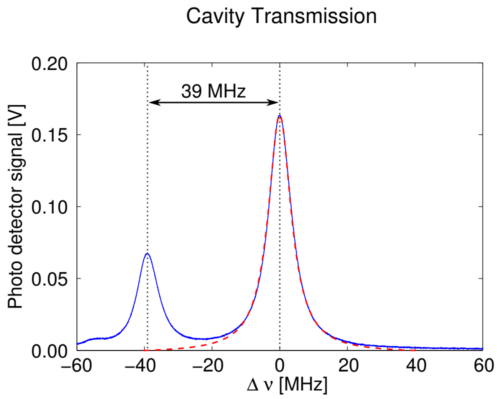

Figure 2.7: *Cavity transmission. The data is taken by detuning the cavity lenght and the distance between the two modes are used for frequency calibration of the x-axis. The red curve is a fit using equation (2.21).*

achieved by employing repumper lasers is thus ≈13.4.

2.2 The Cavity

The cavity consists of two concave mirrors mounted on either side of the vacuum chamber. One of the mirrors is mounted with a piezo electric ring. The piezo-ring is made of a crystal that expands when a voltage is applied. This makes it possible to change the length of the cavity on length scales up to a few wavelength of the probe laser with a resolution much higher than a wavelength. By applying a sawtooth signal on the piezo, the length of the cavity is scanned. Assuming that the displacement of the mirror by the piezo is linear, this will correspond to scanning the frequency of the probe laser. Figure 2.7 shows the intensity of the transmitted light through the cavity as the length of the cavity is changed. The horizontal axis is converted to frequency detuning from resonance using the known spectral distance between the two cavity modes of 39 MHz. This spectral distance has been determined by generating sidebands with a well known frequency, on the cavity field using an Electro-Optic Modulator (EOM). At an EOM modulation frequency of 39 MHz the lower sideband was found to overlap with the second cavity mode. From figure 2.7 the FWHM of the transmission peak is found to be 8.16 MHz. That together with the known Free Spectral Range (FSR) of 500.00 MHz leads to a finesse of

$$F = \frac{FSR}{\delta\nu_{FWHM}} = 61.24. \tag{2.20}$$

The power reflection coefficients R are found by fitting the expression for the transmission

$$I_T = |E_T|^2 = A\frac{(1-R)^2}{1-2R\cos(2\omega L/c)+R^2} \tag{2.21}$$

where ω is the laser frequency, L is the cavity length and A is a scaling parameter. It is assumed that the mirrors have identical reflection coefficients and the cavity loss is neglected. The power reflection coefficient R was found as a fitting parameter to be 0.9694. In this case the fitting was done using a build in function in MATLAB, which later showed to be unreliable as the fitting expression got more advanced.

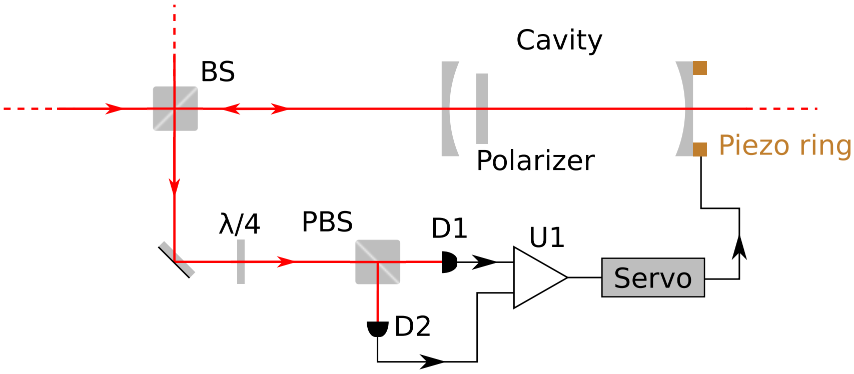

Figure 2.8: *Schematic of the Hänsch-Couillaud locking method. The two different polarities of the cavity reflected light is detected by D1 and D2. U1 is a differential amplifier that gives the difference of the signals on D1 and D2 to the servo circuit which generates a voltage for the Piezo electric ring that controls the cavity's length.*

2.2.1 The Hänsch-Couillaud Cavity Locking Method

During the spectroscopy measurements of the atoms, the cavity resonance is locked to the probe laser frequency. This is done using the Hänsch-Couillaud cavity locking method. This technique was originally developed by T.W. Hänsch and B. Couillaud in 1980 to lock a laser frequency to a cavity [12]. In this set-up it is reversed so that the cavity length is locked to resonance with the probe laser. Figure 2.8 shows a schematic of the locking method.

The light incident on the set-up has a polarization that can be described as a combination of parallel $E_{\|}$ and perpendicular $E_{\perp}$ polarization with respect to some given plane. If these two components are in phase the resulting field will be linear polarized at an angle determined by their mutual amplitude. If they on the other hand are out of phase it will result in an elliptically polarized field.

A linear polariser is placed inside the cavity, making it possible for only the parallel part of the light to resonate in the cavity, as the other polarization is extinguished. This means that reflection of the perpendicular part is independent of the cavity leading to

$$E_{\perp r} = rE_{\perp}. \tag{2.22}$$

As we shall see in chapter 4, a cavity imparts both amplitude and phase to a field dependent on the detuning making the reflection of the parallel part

$$E_{\| r} = E_0 r - E_0 \frac{(1-r)^2 r e^{-i2\omega L/c}}{1 - r^2 e^{-i2\omega L/c}}. \tag{2.23}$$

From this expression the reflection intensity and the phase response is given by the absolute square and the argument respectively. The phase change to $E_{\|}$ makes the combined polarization slightly elliptic, where the helicity is determined by cavity detuning as the phase change is anti-symmetric around resonance. In order to use this effect as an error signal we have to detect whether the combined field reflected from the cavity is σ^- or σ^+ polarized.

By having circular polarized light going through a $\lambda/4$-plate the component parallel with the plate axis is phase shifted by $\pi/2$ (corresponding to a quarter of a wavelength). The combined light is then linearly polarized with an angle at $\pm 45°$ with respect to the $\lambda/4$-plate axis depending on whether it was σ^- or σ^+ polarized.

Having a polarizing beam splitter which axis have a 45° angle to $\lambda/4$-plates axis will split up the light in different directions according to the original helicity.

The differential amplifier in the set-up gives the difference between detector 1 and 2, thus showing whether the cavity-light resonance is positively or negatively detuned. This signal is an anti-symmetric error signal which is fed through a servo-circuit controlling the cavity length.

2.3 The Probe Laser

The probe laser is an ECDL locked to a high finesse ULE cavity using the Pound-Drever-Hall locking technique [13]. The stability of the laser have been estimated by measuring the in-loop Allan deviation of the lock.

2.3.1 Pound-Drever-Hall Locking Technique

The Pound-Drever-Hall scheme uses a hetrodyne sideband method to detect the phase response of cavity reflected light in order to generate an error signal. Using a stable high finesse cavity the spectral width of the laser can be significantly reduced by this technique.

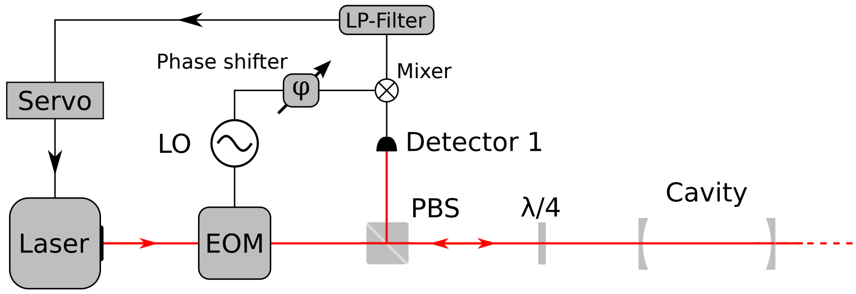

Figure 2.9: *Schematic of Pound-Drever-Hall stabilization technique.*

As shown in figure 2.9 the linear polarized light from the laser undergoes modulation by an EOM. Modulation with a frequency of Ω generates sidebands at $\omega \pm \Omega$. The field can be expressed in terms of the Bessel functions of the first kind $J_n(\delta)$ under the assumption that no residual amplitude modulation takes place.

$$E = E_0 \left[J_0(\delta) e^{i\omega t} + J_1(\delta) e^{i(\omega+\Omega)t} - J_1(\delta) e^{i\omega t} \right] \tag{2.24}$$

Here the minus of the last term account for phase difference of π on the lower sideband. The PBS and the quarter-wave-plate that comes next in the setup are there to split off the light reflected from the cavity. When the field has interacted with the cavity the expression changes to

$$E_r = E_0 \left[r_c(\omega) J_0(\delta) e^{i\omega t} + r_c(\omega+\Omega) J_1(\delta) e^{i(\omega+\Omega)t} - r_c(\omega-\Omega) J_1(\delta) e^{i\omega t} \right]. \tag{2.25}$$

Each term now has a complex reflection coefficient r_c describing their amplitude and phase. This coefficient can be found by considering a Fabry-Pérot interferometer as done in section 4.2.

$$r_c(\omega) = \frac{E_r}{E} = \frac{r\left(1 - e^{-i2\omega L/c}\right)}{1 - r^2 e^{-i2\omega L/c}}. \tag{2.26}$$

By Taylor approximation around $\Delta\omega = \omega - \omega_n$, where ω_n is the n'th resonance frequency of the cavity, we have [3]

$$r_c = \frac{\Delta\omega(\Delta\omega + \Gamma/2)}{(\Gamma/2)^2 + \Delta\omega^2}. \tag{2.27}$$

At this point the reflected fields intensity is measured by detector 1. The intensity is given by

$$\begin{aligned} I = |E_r|^2 = E_0 \big[& |r_c(\omega)|^2 J_0^2(\delta) + |r_c(\omega+\Omega)|^2 J_1^2(\delta) + |r_c(\omega-\Omega)|^2 J_1^2(\delta) \\ & + J_0 J_1 \left(r_c(\omega) r_c^*(\omega+\Omega) + r_c^*(\omega) r_c(\omega-\Omega) \right) e^{-i\Omega t} \\ & + J_0 J_1 \left(r_c(\omega) r_c^*(\omega-\Omega) + r_c^*(\omega) r_c(\omega+\Omega) \right) e^{i\Omega t} \\ & + J_1^2 r_c(\omega+\Omega) r_c^*(\omega-\Omega) e^{i2\Omega t} + J_1^2 r_c^*(\omega+\Omega) r_c(\omega-\Omega)) e^{-i2\Omega t} \big] \end{aligned} \tag{2.28}$$

This intensity which is proportional to the signal from the diode have three frequency components, a DC-component, a component oscillating at Ω and a component oscillating at 2Ω. Demodulating the signal at Ω by using a mixer results in a DC-signal proportional to the amplitude of the component oscillating at Ω. The components of interest for us can be written as[1]

$$\begin{aligned} I \propto 2J_0 J_1 \, [& \Re \{ r_c(\omega) r_c^*(\omega+\Omega) - r_c^*(\omega) r_c(\omega-\Omega) \} \cos(\Omega t) \\ & + \Im \{ r_c(\omega) r_c^*(\omega-\Omega) - r_c^*(\omega) r_c(\omega+\Omega) \} \sin(\Omega t)] . \end{aligned} \tag{2.29}$$

The imaginary part contains the information about the phase. By changing the phase between the detector signal and the local oscillator the sine-term is chosen by the mixer and is used as the error signal. By inserting equation 2.27 in the sine-term we get an expression for the error signal:

$$\epsilon(\Delta\omega) = -\frac{4\Omega^2 \Delta\omega((\Gamma/2)^2 - \Delta\omega^2 + \Omega^2)\Gamma/2}{(\Delta\omega^2 + (\Gamma/2)^2)((\Delta\omega+\Omega)^2 + (\Gamma/2)^2)((\Delta\omega-\Omega)^2 + (\Gamma/2)^2)} \tag{2.30}$$

In figure 2.10a a measurement from the setup of the error signal as a function of detuning is shown. The modulation frequency is 10 MHz. Equation 2.30 is fitted to the measurement, shown as the red curve. The fit shows Γ to be 0.269 MHz. Figure 2.10b shows a measurement of the cavity transmitted light.

2.3.2 Allan Deviation

In order to determine the stability of the probe laser the error signal is used as an in-loop frequency measurement. This is not the optimal way to perform such a measurement, as overall system fluctuations of the lock will not be detected. The ideal way to determine the stability of a laser would be by beating the output light against another laser with a well known high stability. The frequency stability is described by computing the Allan deviation.

The measured error signal is actually a measure of the detuning between the laser frequency and the ULE cavity. To convert the signal from Volts to Hertz a conversion factor is required. By modulating the laser frequency with a low frequency sawtooth signal, we get the error signal as a function of the detuning as shown in figure 2.10a

[1] By using the relation $Ae^{-x} + A^* e^x = 2a\cos(x) + 2b\sin(-x)$, where $A = a + ib$.

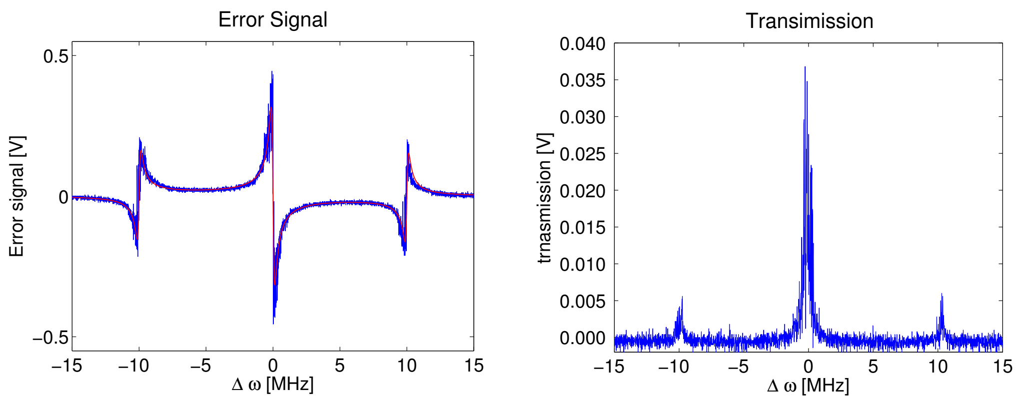

(a) *The Error signal with a modulation frequency at 10 MHz. The measured signal is shown in blue and a fitted curve of equation 2.30 is shown in red.*

(b) *The cavity transmission.*

Figure 2.10: *Pound-Drever-Hall measurements.*

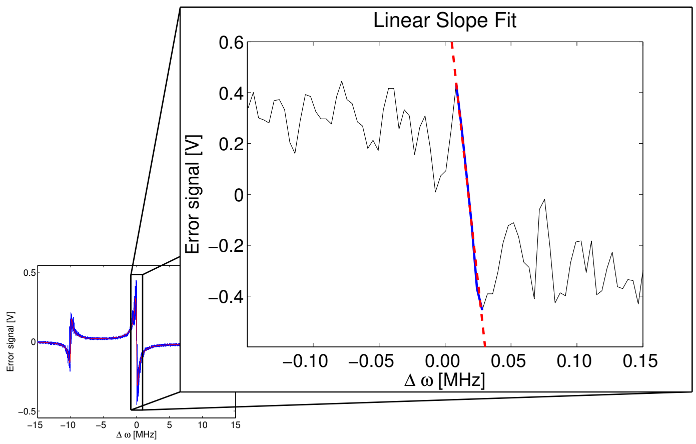

Figure 2.11: *Fit to the centre slope of the error signal scan shown in figure 2.10a to be used for voltage to hertz conversion factor.*

and by fitting equation (2.30) to this signal we get a number of parameters describing the system. One is the ULE cavity linewidth Γ which comes out as 269 kHz relating through a cavity length of 10 cm to a ULE cavity finesse of approximately 5600. Another parameter in equation (2.30) is the modulation frequency Ω. As it is a well known parameter of the EOM in the set-up, this parameter can be used to convert the units of the x-axis.

The servo system uses the slope in the error signal around $\Delta\omega = 0$ to correct for frequency drifts of the laser. This means that a given voltage of the error signal corresponds to a frequency detuning, meaning the slope of the error signal around $\Delta\omega = 0$ can be used as a direct conversion from voltage to Hertz of the error signal when the laser is locked. A measurement of the error signal is thus a measurement of the lasers frequency detuning compared to the ULE cavity.

The Allan deviation shows averages of the frequency deviation over different time-scales. This is computed by averaging frequency deviation over a timespan of τ, 2τ, 3τ and so on. By doing this we get a good picture of how the noise cancels out for

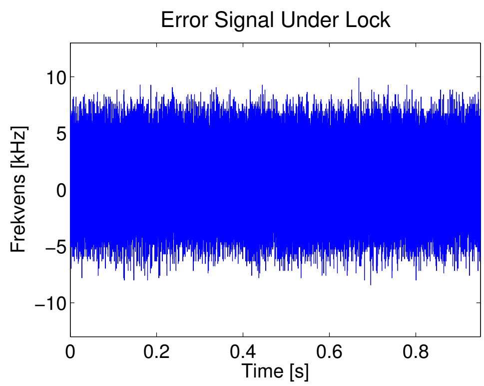

Figure 2.12: *Error signal measurement taken while the laser frequency is locked to the cavity. The signal has been converted to Hertz using the linear fit in figure 2.11.*

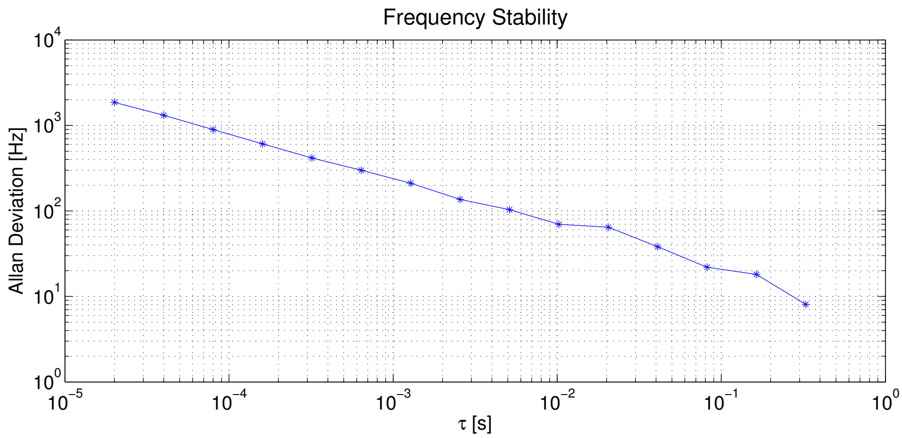

Figure 2.13: *Allan deviation plotted for data from 10 consecutive 0.1 second measurements of the error signal for the probe laser under lock.*

longer averaging times. The Allan variance (the square of the deviation) is given by

$$\sigma_y^2 = \frac{1}{2}\langle(\bar{y}_2 - \bar{y}_1)^2\rangle, \tag{2.31}$$

where $\bar{y}_i$ is the mean of the measured frequency deviation over the time τ:

$$\bar{y}_i = \frac{1}{\tau}\int_{t_i}^{t_i+\tau} y(t)\mathrm{d}t. \tag{2.32}$$

In figure 2.13 the Allan deviation of a composition of ten 0.1 second consecutive measurements are shown. A deviation of 800 Hz is found for 100 μs of integration time. This can be related to a spectroscopy resolution of 800 Hz when interrogating the atoms for 100 μs. When we do spectroscopy on the atomic transition with a linewidth of 7.6 kHz, with an integration time of 100 μs as is commonly used in our experiments, we see clear structures over a few hundred kilo Hertz, supporting the claim of a spectral resolution at or below a couple of kilo Hertz.

The MATLAB-scripts used to make the fits and calculate the Allan deviation is given in appendix A.

2.4 The Detection Scheme

I have now described the atoms, the cavity and the probe laser. Now I will describe the detection scheme that is used to perform the spectroscopy. The cavity enhanced spectroscopy set-up is shown in figure 2.14. In this set-up the probe laser is fed in through a fiber and injected into a slave diode for amplification, this is not included in figure 2.14. After the amplification it is sent through an AOM which allows for frequency tuning of the diffracted beam. This beam is then modulated by an EOM generating sidebands at the cavity's FSR. As described above (section 2.2), the cavity is locked to resonance with the probe laser at all times, ensuring that when the laser frequency scans the atomic transition, the cavity follows the probe laser and maintains standing waves. The cavity mirrors are placed on the outside of the vacuum chamber containing the atoms. The cavity transmitted light is recorded by detector D1 and D2. Detector D1 is an avalanche photodiode. The computer uses the signal from D1 to calculate the normalized transmittance of the cavity, thus generating an signal equivalent the atomic absorption. Detector D2 is a fast avalanche photodiode capable of detecting intensity oscillation up to 1 GHz. As shown on figure 2.14 the probing light is modulated with a frequency at the cavity FSR which is 500 MHz. Detector D2 can thus detect the 500 MHz modulated signal that afterwards is filtered and demodulated. Detecting and amplifying the signal at 500 MHz is a great advantage as the amount of electrical and mechanical noise is very low at such high frequency. Demodulating the 500 MHz signal results in DC-signal proportional to the cavity fields phase response to the atoms. This set-up is called the NICE-OHMS technique and will be described in detail in section 4.1.

The set-up is operated in a cyclic manner where the atoms are captured and cooled in the MOT. The MOT light is then shut off before the signal from the detectors is recorded and integrated over a period of 100 μs. The MOT beams are shut off in order to avoid AC-stark shift to the energy levels that are probed. As shutting off the laser beams require a finite time, a delay of typically a 100 μs is in between shutting the MOT beams and detection. Another thing to keep in mind regarding the detection delay is whether or not the atom-light interaction has reached steady state at the time of recording. This will be discussed in chapter 5. At each step in the cycle the frequency of the probe laser is shifted using the AOM in such a way that a new data point for the atomic spectrum is recorded. Figure 2.15 shows the steps in the measurement cycle.

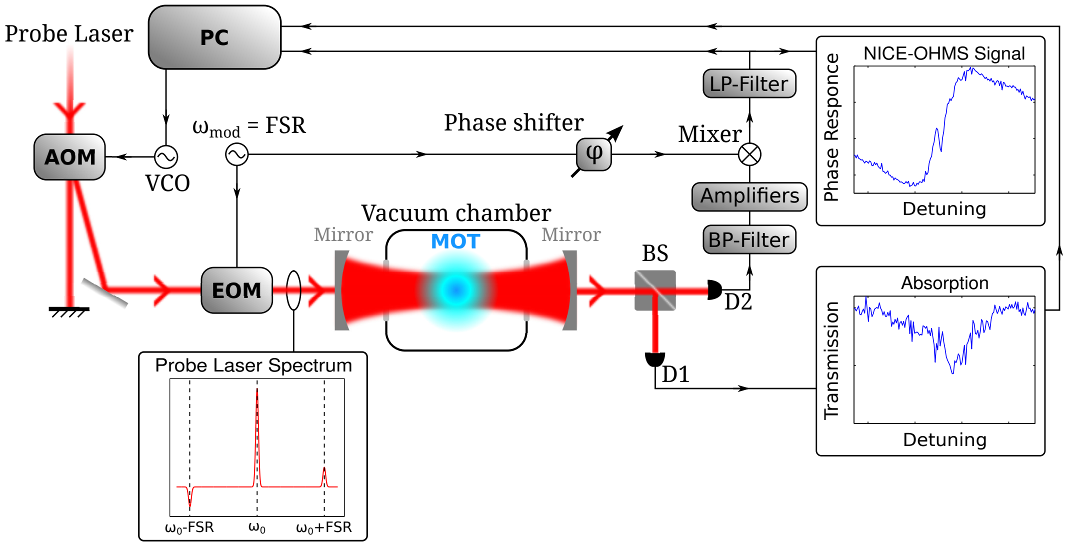

Figure 2.14: *The cavity enhanced spectroscopy part of the experimental set-up. The probe laser is modulated by an EOM with a frequency equal to the cavity FSR. The probe laser interacts with the cavity-atom-system inside of a vacuum chamber. The* ^{88}Sr *atoms are cooled and trapped by a MOT inside a cavity. The probe laser is detected by detector D1 and detector D2. Detector D2 is a fast photo diode with a bandwidth greater than the modulation frequency. The signal from detector D2 is filtered, amplified and demodulated using a mixer. An RF phase shifter is used to maximize the mixer signal.*

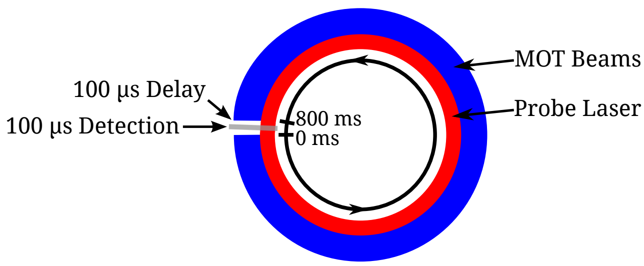

Figure 2.15: *The detection cycle. The probe laser is on throughout the cycle. The MOT beams are shut off after reaching a maximum of atoms in the trap, typically after 800 ms. A 100 μs detection of the probe light is done after a 100 μs delay after the MOT beams have been shut off.*

Chapter 3

Experimental Development

This chapter is a review of the different elements of the experimental set-up that I have worked on with the purpose of improving different aspects. A new laser system to drive the $^3P_2$ - $^3S_1$ repumper transition has been developed. To that account, a description of an ECDL using the Littman-Metcalf scheme is given, along with a review of the development of a digital temperature stabilization system using the Raspberry Pi mini computer.

As part of this thesis an investigation was done into the time-evolution of the atom-cavity system. This required fast shutting time and well known shutting efficiency for the MOT light beams. Three different shutting systems are investigated consisting of AOM shutting, shutting using a Pockels cell and a mechanical shutting system utilizing the actuator found in hard disk drives.

The frequency stability of the probe laser has direct influence on the atom-light interaction we are investigating. Doing our work in the laboratory we found that the VCO driving the AOM in the experimental set-up caused significant drifts in the light frequency. A digital synthesizer chip is investigated in order to determine if it can be used to drive multiple AOM using one stable oscillator.

3.1 Repumper

When running the experiment and doing the measurements a lot of effort is put into having stable systems. In the current stage of this experiment we are trying to investigating the dependencies of the system on different parameters. Having a parameter such as the number of atoms fluctuating during a measurement, gives rise to signal noise and thus clouds the physics we are hoping to see. The old repumpers in the set-up have caused great problems with keeping a constant number of atoms over the timespan of one measurement. In order to remedy this problem a new set of repumper lasers have been developed. In this section construction of a 707 nm ECDL will be described.

3.1.1 External Cavity Diode Laser

The External Cavity Diode Laser (ECDL) is a laser set-up that usually consists of a semiconductor diode laser, a collimator for the diode output and an external cavity as a mode-selection filter. Because of the commercial available broad spectrum laser diodes the ECDL can, by spectral mode selection with an external cavity, obtain a large tuning range compared to other laser systems. Typically a diffraction grating is used to build the external cavity. The external cavity resonance frequency can hence be controlled by both grating angle and cavity length.

Making a Narrow Linewidth Laser

The basic build of a laser consists of a gain medium inside a cavity. The electrons in the gain medium are put into excited states resulting in spontaneous emitted light that bounces back and forth in the cavity causing accumulation of coherent stimulated emission. If the gain medium's amplification of the intra cavity photon is greater than the cavity loss, coherent light is produced and lasing is said to occur. Achieving steady state lasing sets a lower limit on the population ratio of excited states in the gain medium. This is known as the threshold. The frequency and spectral width of the light is determined by the electrons' transition options and the surrounding cavity. In a laser diode the cavity is made by polishing the gain crystal's surface resulting in a very low finesse and very short cavity. The small cavity length leads to a very high spectral distance between possible cavity modes, but the low finesse leads to high loss and thus a high threshold.

In a semiconductor diode the gain medium is composed of n and p-doped silica crystals giving rise to an energy structure that can be modelled as quantum wells. The energy of an electron in a well is can be written as [14]

$$E_n = \frac{n^2\pi^2\hbar^2}{2m_e d^2}, \tag{3.1}$$

where m_e is the effective mass of the electron, d is the width of the well and $n = 1, 2, 3, ...$ is the energy state of the electron. The photon in such a diode is emitted when an electron jumps from the conductance band E_c to the valance band E_v, shown in figure 3.1. The energy of the photon is defined by the electron jump and the photon frequency ν is thus given by

$$h\nu = E_g + \frac{n^2\pi^2\hbar^2}{2d^2}\left(\frac{1}{m_e} + \frac{1}{m_h}\right). \tag{3.2}$$

where m_h is the effective mass of a hole[1] in the valance band. Photons from the diode gain medium have frequencies spread over the different energy states E_n of the electrons with an overall dependence on gab-energy E_g. This leads to a very wide gain profile which means that despite the small cavity length, multi mode lasing can occur.

Putting the diode in an external cavity lowers the overall loss of photons and reduces the spectral width. Combining the gain mediums frequency profile with the different components of the ECDL, gives a narrow frequency range where lasing is possible. The laser diodes own cavity enhances a frequency range within its own gain profile, the external cavity and the angle of the diffraction grating does likewise. Figure 3.2 illustrates a combination of gain and mode profiles. This combination inhibits mode jumps, since the distance between the possible mode overlaps are large compared to the gain medium.

The different gain and mode profiles have different tuning parameters, meaning that it is possible to move each gain curve up and down the frequency axis more or less independent of each other. The diode medium changes with the diode current, as the voltage over the crystal changes E_g in equation (3.2). The internal cavity

[1] "Hole" describes the lack of an electron in the crystal structure.

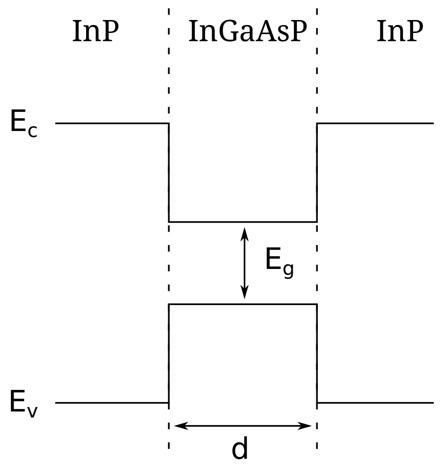

Figure 3.1: *Energy band diagram showing quantum wells for a InGaAsP doped crystal.*

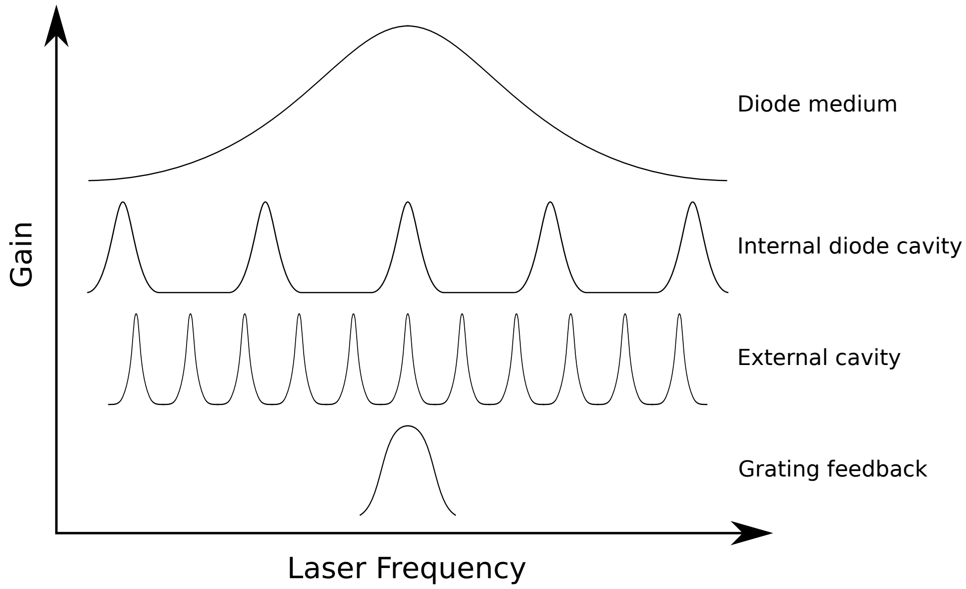

Figure 3.2: *A sketch of the individual frequency response of the different components that makes up an ECDL. The output profile will be the combination of all four.*

changes with diode temperature, due to the thermal expansion of the diode. The external cavity length can be changed simply by translation of whatever constitutes the external cavity mirror. Finally the diffraction grating's angle determines the feedback frequency.

The Littman-Metcalf Scheme

The Littman-Metcalf configuration (figure 3.3) uses a grating in a grazing-incidence configuration. The external cavity is a three mirror set-up consisting of the rear facet of the laser diode, a diffraction grating and a mirror. The geometry is such that the first order diffraction of the light is reflected back into the laser diode. Tuning is done by moving the mirror around a pivot point, so that the refraction angle and cavity length support the same frequency and mode. The output beam is the direct zeroth-order reflection from the laser diode. This configuration has a relatively high

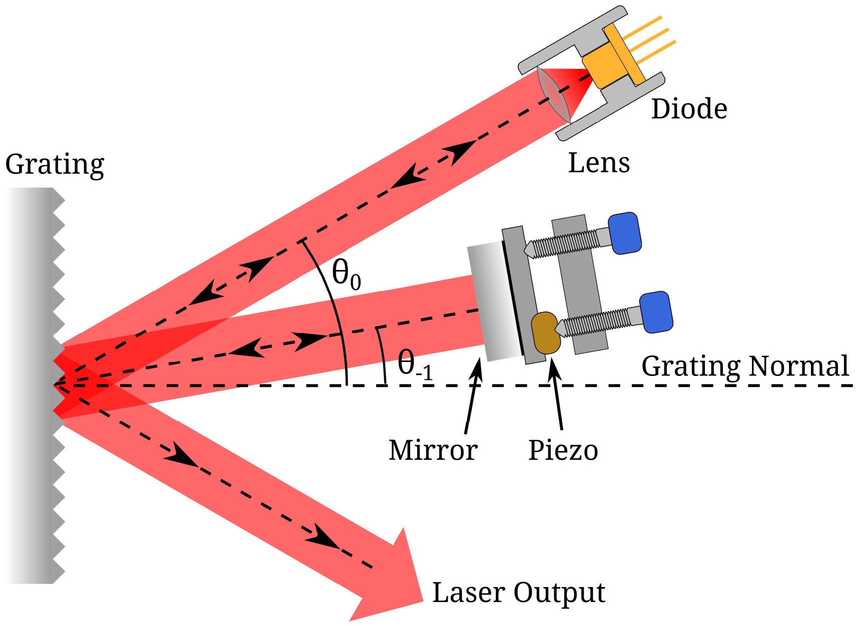

Figure 3.3: *Schematic of the Littman-Metcalf configuration. Light from the laser diode is collimated so that the beam is slightly convergent. First order diffraction of the light is reflected back into the diode thus making a cavity.*

spectral tuning resolution and has the great advantages that the output beam does not move when the laser is tuned.

The spectral width of a configuration like this is given by [14]

$$\frac{\Delta\lambda}{\lambda} = \frac{\lambda}{\pi w \sin(\theta_0)}, \tag{3.3}$$

where λ is the output wavelength, $\Delta\lambda$ is the half width half maximum of the output spectral distribution, w is the width of the grating area illuminated by the beam and θ_0 is the angle of the incident beam with respect to the grating normal. From this equation it is clear that the greater the beam width and the angle θ_0, the better.

The Collimation Lens

The light from the diode has a large divergence making the feedback into to the diode impossible, thereby creating the external cavity. In order to have a stable cavity the light from the diode has to be converging with a focal point at no less than the half the cavity length. In equation (3.3) the width of the beam is shown to be proportional to the spectral width of the output, resulting in an optimal focal point at infinity.

The laser diode and collimation lens is placed in a Thorlabs collimation tube where a thread on the inside allows for tuning of the distance between the laser diode and the lens. Using an aspheric lens with a focal length of 4.03 mm a focal point at 1 to 2 meters was obtained.

The Diffraction Grating

When choosing the diffraction grating for this set-up, one has to consider the general geometry. Through the collaboration with Jun Ye's laboratories at JILA in Boulder,

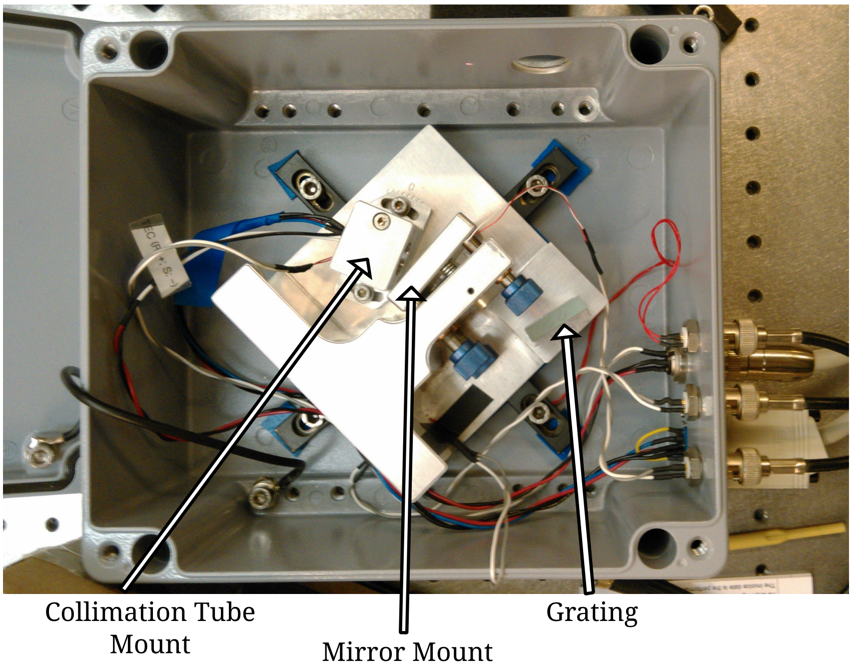

Figure 3.4: *A picture of the ECDL. The mount is placed inside metal case mounted to an optical table through the bottom. The output beam exits the case through a anti-reflection coated window, seen in the upper part of the picture.*

Colorado, we got drawings of a Littman-Metcalf ECDL mount to be milled out of only three pieces of metal. The workshop at the Niels Bohr Institute machined five mounts in aluminium. Figure 3.4 is a picture of this mount. The three pieces constitute a base, a collimation tube mount and a mirror mount attached with springs and screws. Due to the way the mount is constructed the difference between the zeroth and first order reflections have to be within a few degrees of 22 degrees.

There are two parameters to consider when choosing a grating. One is the number of grooves per millimetre which can be determined from the general grating equation

$$\lambda n = d(\sin(\theta_0) + \sin(\theta_n)), \tag{3.4}$$

where n is the diffraction order, θ_n is the diffraction angle and θ_0 the angle of the incident beam. The desired wavelength of this laser is 707 nm and by imposing the geometric restriction that $\theta_{-1} \approx 22\ ^\circ$, the grating equation gives a relation between groove density and incident angle. Figure 3.5 shows equation 3.4 under the conditions $n = -1$, $\lambda = 707$ nm and $\theta_{-1} = 22\ ^\circ$. According to equation (3.3) θ_0 should be as large as possible and thus a high groove density is desired.

The other parameter to consider is the diffraction intensity of the grating. It is this that effectively determines the finesse of the external cavity, as the light in the first order diffraction beam constitutes the cavity field. It is therefore also this that determines how much light escapes the cavity. The diffraction intensity is dependent on the blaze angle of the grating and the light's polarization with respect to the grooves. Figure 3.6 is taken from the specification sheet for the Thorlabs GR25-1204 grating and shows the percentage of the incident beam that is diffracted to first order for light polarized parallel, perpendicular or as an average of the two. By choosing this grating the effective power reflection coefficient of the external cavity mirror can be tuned from 0.2^2 to 0.5^2. The diffraction coefficients are the squared, as the

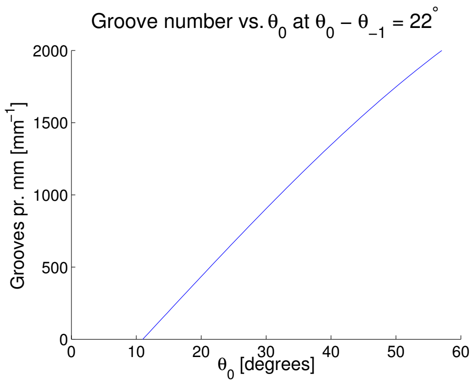

Figure 3.5: *A plot of the general grating equation made to determine the appropriate grating groove density for the JILA mount geometry.*

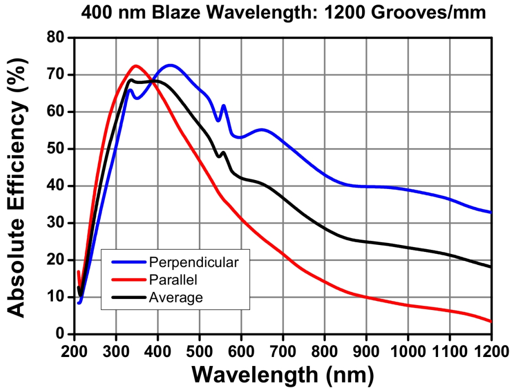

Figure 3.6: *Diffraction efficiency of the GR25-1204 diffraction grating from Thorlabs.*

light passes the grating twice in one cavity round trip. Tuning the polarization is done by physically rotating the diode, and thereby rotating the polarization of the light. The tuning range is reduced by the fact that the diode is not perfectly linearly polarized. For the purposes of the Littman-Metcalf set-up the diffraction have to be in the $n = -1$ order instead of $n = 1$, which can easily be accomplished by rotating the grating 180 ° effectively inverting the blaze structure.

After these considerations a number of different gratings was tried. The grating that gave the best results was the Thorlabs GR25-1204 grating with a groove density of 1200 grooves per millimetre and a blaze angle of 13 ° optimized for a wavelength of 400 nm.

Injection

Injecting an ECDL can be a long and tedious process. Injecting an ECDL is the process of optimizing the external cavity to achieve single mode lasing at the desired wavelength. There is a lot of parameters that can be tuned, in order to change different characteristics of the external cavity, all influencing the injection and thus the laser stability.

The most common way to optimize injection is by trying to lower the laser current threshold as much as possible while at the same time keeping the wavelength close to the desired value. The way to do this in practice is by looking a the laser output intensity while modulating the diode current around the threshold current. Using an oscilloscope you can get a real-time P-I (laser power vs. diode current) plot and thus see the effect of aligning the mirror position and angle on the threshold. After the optimal threshold is found the polarization is slightly rotated, changing the fraction of feedback. The mirror position and angle is then optimized and the process is repeated until the optimal feedback is found. A similar aligning process is done in regards to the focal point of the diode's output.

3.1.2 Temperature Stabilization

The ECDL mount is as mentioned before milled out of three pieces of aluminium. This makes the construction optimized in regard to mechanical tension which can cause drifts to sensitive angles and lengths. Another thing which causes the same problem is temperature fluctuations in the base. In order to reduce this drift a temperature stabilization scheme was developed. This scheme uses a 10 kΩ thermistor inserted into a small hole in the mount base to measure the temperature and a thin flat heating element covering the underside of the base (see figure 3.13). To monitor the mount base's temperature and control the heater, a low bandwidth digital unipolar servo-system was build.

The servo-system is consists of a Raspberry Pi with a Digital to Analogue Converter (DAC) and an Analogue to Digital Converter (ADC). The Raspberry Pi is a low cost mini computer running on an ARM-processor that is characterised by its small size and low energy consumption. The Raspberry Pi is per default running a simplified version of the open source Debian Linux operating system with a full integration of the Python programming language. The Raspberry Pi runs the Python code in appendix C.

The DAC/ADC circuit diagram is shown in appendix B. It has two of both DACs and ADCs making it possible to use as a two channel servo-system so both the 707 nm and 679 nm repumper lasers can be independently temperature controlled by one Raspberry Pi system. The DACs are a MCP4725 chip which have a 12 bit output voltage resolution. The ADCs are a MCP3421 chip which have a 18 bit differential voltage input. Both chips utilizes the I^2C protocol for digital communication. The programming code dealing with the chip communication is given in appendix C.2.

Measuring the Temperature

The MCP3421 chip reads the voltage over its differential input pins, so in order to read the temperature information provided by the thermistor, a conversion from ohm to voltage is needed. This is done through a Wheatstone bridge as depicted in figure 3.7. By applying a constant voltage U, as shown, a change in resistance will lead to a change in voltage over the bridge U_T. The voltage U_T is given by

$$U_T = \left(\frac{R_T}{R_3 + R_T} - \frac{R_2}{R_1 + R_2} \right) U, \tag{3.5}$$

where R_T is the thermistor and R_2 is a variable resistor making it possible to calibrate the output voltage.

The thermistor's resistance is related to its temperature through this equation

$$T = \frac{1}{a + b \ln\left(\frac{R_T}{R_{25\ ^\circ\mathrm{C}}}\right) + c \ln\left(\frac{R_T}{R_{25\ ^\circ\mathrm{C}}}\right)^2 + d \ln\left(\frac{R_T}{R_{25\ ^\circ\mathrm{C}}}\right)^3}, \tag{3.6}$$

where T is in units of Kelvin and the different parameters are given in the Thorlabs specification sheet for the TH10K thermistor shown table 3.1.

The MCP3421 has an internal precision reference voltage at 2.048 V, making the range of the digital voltage conversion ±2.048 V. Furthermore it has a Programmable Gain Amplifier (PGA) capable of a gain of 8, making the voltage measure range ±0.256 V. In the current version of the DAC/ADC-circuit the voltage U in equation (3.5) is the same as the supply voltage which can be chosen to be $V_{DD} = 3.3$ V

$R_{25\ ^\circ\mathrm{C}}$	10 kΩ
a	3.3540170e-3
b	2.5617244e-4
c	2.1400943e-6
d	-7.2405219e-8

Table 3.1: *Thermistor resistance to temperature conversion parameter for equation* (3.6).

	$V_{DD} = 3.3$ V	$V_{DD} = 5.0$ V
Meas. range of R_T [kΩ]	[7.239 ; 13.533]	[8.060 ; 12.158]
Temp. range [°C]	[18.2496 ; 32.5235]	[20.6094 ; 29.9845]
Temp. resolution [μK]	54.450	35.763

Table 3.2: *The theoretical limit for temperature measurement using a TH10K Thorlabs thermistor in a Wheatstone bridge with $R_1 = R_3 = 10$ kΩ, $R_2 = 9.9$ kΩ and a MCP3421 with PGA = 8 and 18 bit ADC resolution.*

or $V_{DD} = 5$ V. Combining this with equation (3.5) and (3.6) the theoretical temperature resolution can be found. The measuring range and resolution is shown in table 3.2.

Changing the Temperature

The heating element used is a Minco HK5178R42.9L12A flexible heater. In contrast to temperature control using a Peltier element this set-up is only able to actively heat and not cool, making it a unipolar servo system. Cooling happens through heat dissipation to the surroundings. For compatibility with our laboratory voltage supply units the heating element is operated with a maximum voltage of 15 V, corresponding to 350 mA. In order to find the optimal operating temperature for such a system, a measurement was made to determine at what temperature the heating and cooling processes are equal. Figure 3.9 shows the heating and cooling rates versus the temperature. To achieve the highest stability the operating temperature is chosen to be at the point where heating and cooling happens at the same rate. The operating temperature is chosen to be 25.1 °C.

The DAC is not able to supply the power to operate the heating element. For this purpose a set of transistors set-up as a Darlington pair (figure 3.8) is connected to the DAC. The idea of this circuit is to have the DAC deliver a very low current in order not to strain the chip, which could lead to an increase in system noise. At the same time it is required to have a transistor that is capable of operating with up to 400 mA continuously thus having to withstand a high energy dispersion in the transistor. The transistor chosen for the high power control is the BD241C with a current gain of $h_{FE} = 25$, and thus a current of $I_B = \frac{350\ \mathrm{mA}}{25} = 14$ mA is needed to fully open the heating circuit. The current is controlled by a BC547C transistor with a current gain of $h_{FE} = 420 \sim 800$ leading to a very low current load on the DAC. Operating at 3.3 V, the required current is on the order of 10 μA. An important fact about transistors is that the voltage over the base and emitter has to be higher than a given saturation voltage. For the BC547 this saturation voltage is 0.66 V leading to a reduction in the heating resolution as a voltage from 0 V to 0.66 V, of the 3.3

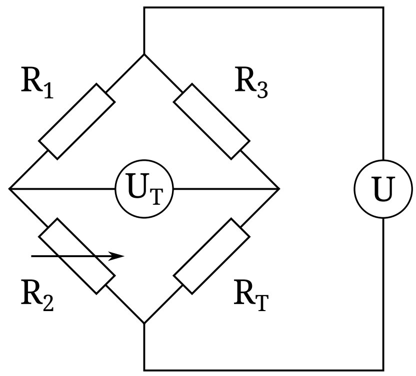

Figure 3.7: *Wheatstone bridge. The resistor R_T is the thermistor and U_T is the voltage dependent on the resistance of R_T and thus the temperature. U is a constant voltage.*

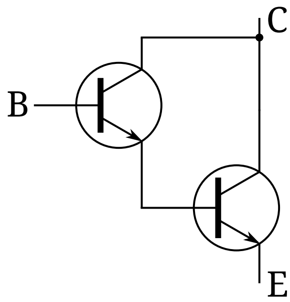

Figure 3.8: *Transistor Darlington pair. The base (B), emitter (E) and collector (C) for the combined transistor are marked.*

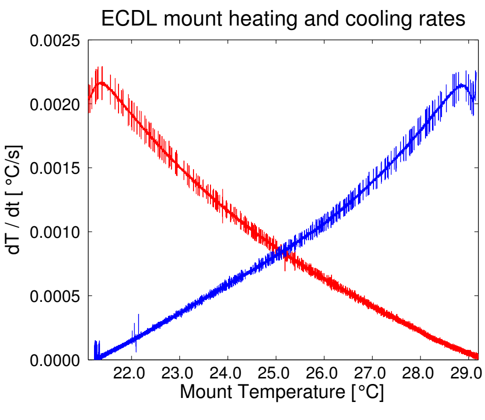

Figure 3.9: *The mount temperature change versus temperature. The heating rate for 15 V over the heating element is shown in red. The cooling rate is shown in blue.*

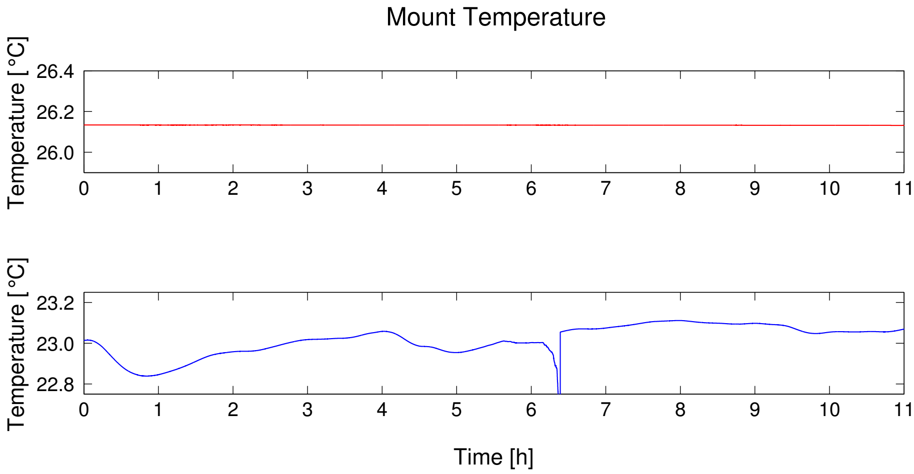

Figure 3.10: *Mount temperature. The red data is taken with active temperature control of the mount. The blue data is taken without any temperature control.*

V control voltage span, have no effect. Optimising of the currents in the Darlington circuit by inserting different resistors, I achieved a resolution of the heater current of a little over 11 bits. The complete circuit is shown in appendix B.

Performance of the Temperature Controller

Figure 3.10 shows the mount temperature over a period of 11 hours. The temperature was measured using a Thorlabs TH10K thermistor and a Agilent 34461A digital multimeter. The measured thermistor resistance was converted using equation (3.6). The red data was taken when the temperature controller was turned on and has a standard deviation of 0.548 mK. The blue data was taken when the temperature controller and heating element was turned off and has a standard deviation of 70.886 mK.

At about 6.4 hours into the measurement without temperature control a temperature jump of 1.09 °C over a period of 0.42 seconds occurred. This is highly unlikely considering the heat capacity of the aluminium mount and must be regarded as a measurement error. This measurement error is omitted for the calculation of the standard deviation.

There is room for optimization of this temperature controller system. The most prominent of which is the Wheatstone bridge. The measurable temperature range is far greater than needed and by increasing the bridge voltage U this is reduced, leading to a greater resolution. Going from 3.3 V to 5 V on the current print (appendix B) requires no more than changing the resistor governing the DAC output current. Going higher would necessitate a new print as the bridge voltage on the current print is connected to the main supply voltage.

It is evident in the histogram in figure 3.11 that there is drift of the temperature. Comparing this to the in-loop measurement shown as a histogram in figure 3.12, where there is no drift and in fact a deviation of $\sigma = 51.9\ \mu$K showing a full utilization of the 3.3 V resolution. This suggests that the drift is in the stabilisation system and a strong correlation with the temperature drift of the potentiometer in the Wheatstone bridge was found. When these measurement where performed, the electronics had not yet been placed in a case. Doing this will most likely reduce this temperature drift.

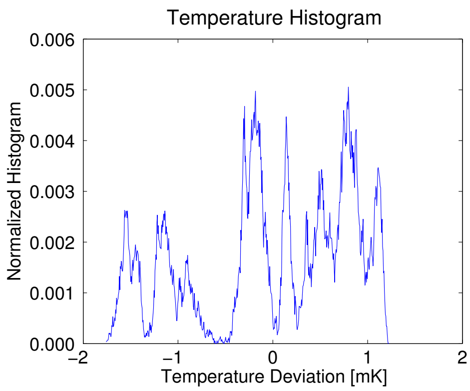

Figure 3.11: *Histogram of the ECDL mount temperature. This histogram shows the same data as the upper plot in figure 3.10.*

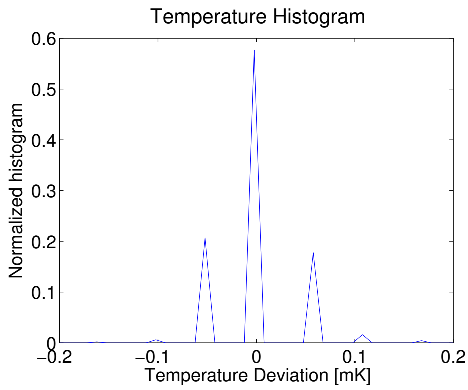

Figure 3.12: *Histogram of in-loop measurement of the ECDL mount temperature.*

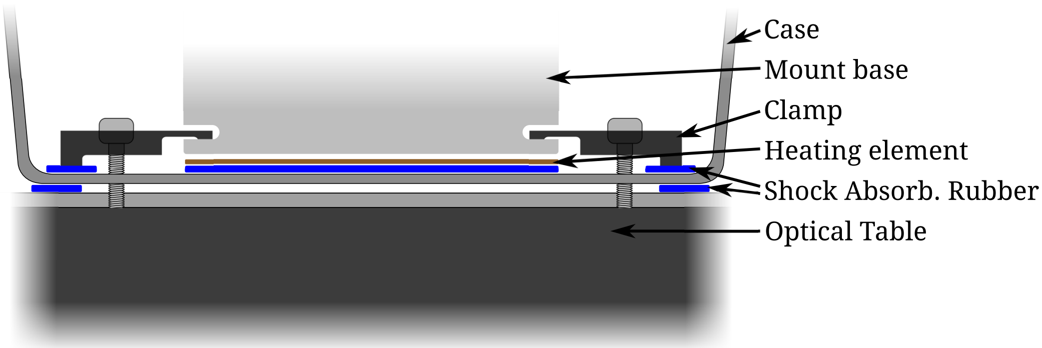

Figure 3.13: *Illustration of how the ECDL mount and case is fastened to the optical table. The blue parts is shock absorbing rubber. The thin brown layer just under the mount is the heating element for the temperature control.*

3.1.3 Vibrations

To minimize vibrations from the optical table a shock absorbing rubber material was placed under the mount base, under the clamps holding the mount and between the case and the optical table. The mount is fastened by four clamps with loosely tightened screws so not to inhibit the shock absorption of the rubber. Figure 3.13 illustrates the vibration retardant set-up.

3.1.4 Performance

The desired wavelength of 707 nm was successfully achieved with the new ECDL. The frequency of both the old ECDL in the experimental set-up and the new ECDL described here was measured with an Ångstrom WSU/2 wavemeter. These measurements where done over a period of 12 hours, to investigate the frequency of mode jumps and their general frequency drift. Figure 3.14 shows the measurement data, where the mode jump free section of both is plotted as a histogram. Within these sections the old ECDL has a constant downward frequency drift making the histogram quite wide. A standard deviation of 143.9 MHz was found over a period of

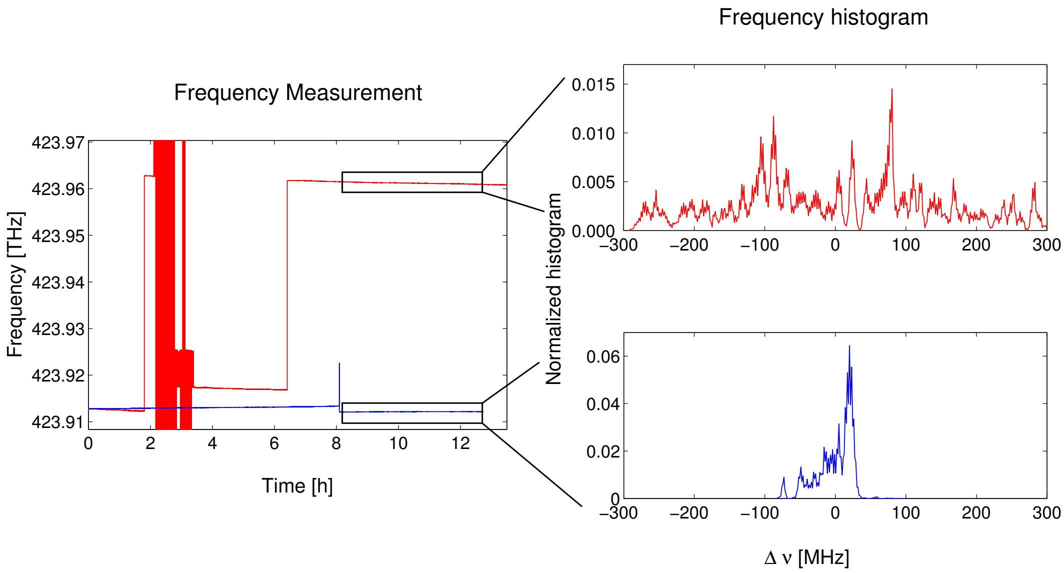

Figure 3.14: *Comparison of the old Littrow ECDL (red) with the new Littman-Metcalf ECDL (blue). The histogram plots are made from a 4.6 hour mode jump free section of the 12 hour measurements. The old ECDL has a standard deviation of 143.9 MHz, where the new ECDL is 25.6 MHz.*

4.6 hours for the old ECDL. The new ECDL also has a drift though much smaller resulting in a more Gaussian looking histogram. A standard deviation of 25.6 MHz was found over a period of 4.6 hours. The old ECDL has a series of mode jumps, whereas the new only experiences one mode jump.

It is worth noticing that the measurement of the new ECDL was started immediately after the injection and temperature control was optimized. A higher stability can possibly be measured if the new ECDL had had a few day to reach mechanical and thermal equilibrium. Furthermore, the measurement was done without an optical isolator making unwanted feedback possible. ECDLs are sensitive to optical feedback and an optical isolator might also improve the stability. Unfortunately it was not possible to make a proper measurement as the wavemeter used was not available at the time.

3.2 Shutter

To avoid A.C. Stark shift to the clock transition, the MOT beams are turned off before the probe signal is recorded. When the MOT beams are turned off the atoms start to evaporate from the trap into the vacuum chamber and within milliseconds there are no more atoms in the cavity. As the signal is dependent on the number of atom we are, for some measurements, interested in having as high a number of atoms in the cavity as possible. Therefore the delay that arises from a finite shutting time before recording of the signal, should be minimized. This sets high demands on the system that shuts off the MOT light. The investigations into the atom-cavity time-evolution does likewise require well known shutting parameters.

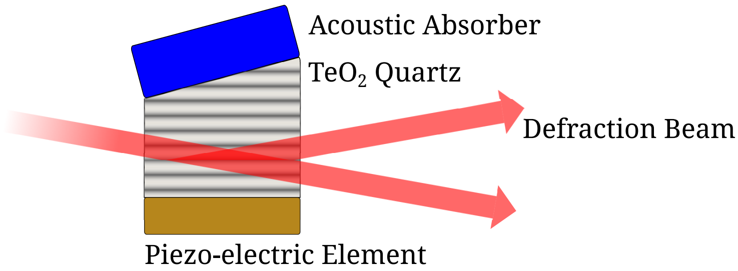

Figure 3.15: *A piezoelectric element creates phonons propagating up through the TeO_2 quartz. The phonons are absorbed by an acoustic absorber. The quartz is cut in an angle to minimize phonon reflection.*

3.2.1 Acusto-optic Modulator

In the experimental set-up the light for the MOT and the Zeeman slower is generated by a laser system consisting of an infra-red ECDL and a frequency doubling cavity. The laser system is locked to the atomic $^1S_0$ - $^1P_1$ transition by using the shoulder of the atomic florescence spectrum from a Sr beam in a reference oven. An AOM is then used to shift the frequency to the required detuning for the MOT and is also used to shut off the MOT light. This is done as the RF-amplifier driving the AOM is turned off by a TTL-pulse generated by the data acquisition computer. Turning off light in this way is extremely fast. There is however a problem with an afterglow.

An AOM exploits the fact that high density change in a crystal reflects light due to the difference in the refractive index. By driving a piezoelectric element with a RF signal, it is possible to generate phonons propagating through the crystal. These phonons can be described as a series of high density sections moving through the crystal. The light that is scattered off these moving planes of high density, will be frequency shifted due to the Doppler effect. Figure 3.15 shows a simple drawing of an AOM.

By abruptly switching the RF signal to the piezoelectric element off, light will cease to be diffracted as the last phonon passes the light beam. The AOM controlling the MOT and Zeeman light is a AA.ST.345/B40/A0.5-vis from Opto-Electronique and according to the specification sheet, the acoustic mode velocity in the crystal is 4200 m/s. The beam width of the light at the point of the AOM is approximately 0.5 mm in diameter. This gives a possible minimum shutting time of

$$t_{AOM} = \frac{0.5 \text{ mm}}{4200 \ \frac{\text{m}}{\text{s}}} = 0.12 \ \mu\text{s} \tag{3.7}$$

The afterglow starts at approximately 10 % of the intensity and dies off exponentially. This is most likely due to phonons in the crystal that live on after the shut-off due to an imperfect absorption. This afterglow is clearly observable on figure 3.16, which shows the measured diffraction intensity. Upon further examination of the plotted data, the shut-off time, neglecting the afterglow, is found to be 0.1 μs, which is well within the uncertainties of the calculation in equation (3.7). The ratio of light in the deflection beam 5 μs after shutting was found to approximately 1/240.

3.2.2 Mechanical Shutter

By inspiration from [15] development of a fast mechanical shutter, made from the insides of a hard disk drive, was started. The insides of a hard disk drive consists

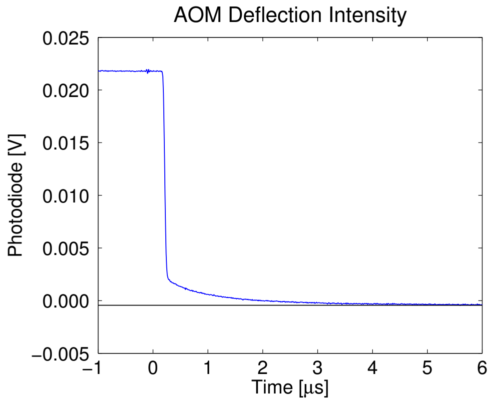

Figure 3.16: *Light intensity during shutting with an AOM. The vertical line indicates the background photodiode voltage.*

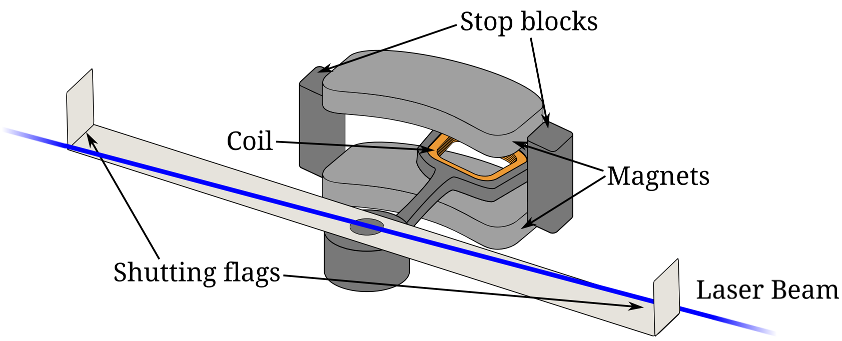

Figure 3.17: *Conceptual design of a mechanical shutter using a hard disk drive voice-coil actuator and a rod with two shutting flags.*

of delicate mechanics capable of moving very fast. This is primarily the actuator moving the reading and writing heads over the magnetic disks. The design of this shutter entails dismantling a hard disk drive and attaching a shutting flag on the actuators. By attaching a rod such that the rod centre is at the actuators pivot point and having shutting flags at both ends of the rod effectively halves the shutting time. A drawing of this set-up is shown in figure 3.17.

The driving circuit for the shutter is a slightly modified version of the circuit used in [15]. A large amount of high speed ceramic capacitors is applied to deliver a high current through the actuator coil very fast. This is accomplished by using a H-bridge, in this case the LMD18200 chip from Texas Instruments. With this H-bridge a TTL input controls which way the current runs through the coil. The capacitors are then connected so that they discharge through the coil when the H-bridge changes the direction of the current. In order to increase the speed of the actuator, the current through the coil needs to increase. This can be done by simply increasing the voltage. Currently, the capacitors set the limit as they can only withstand 25 V, while the H-bridge is designed for 55 V. The circuit schematics is shown in appendix D. Using an actuator from a 2.5 inch hard disk drive with a 3.5 cm shutting rod of aluminium and running the circuit at 25 V, a shutting time of approximately 100 μs was achieved on a laser beam with a diameter of 1 mm.

Due to a long delivery time of the new high voltage ceramic capacitors, the development was halted and the focus shifted towards the Pockels cell set-up. A

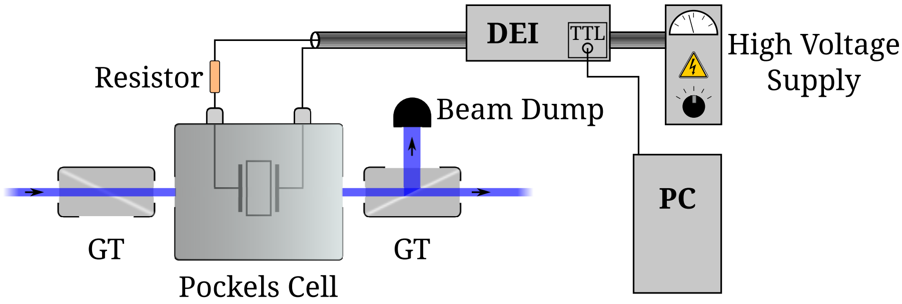

Figure 3.18: *Schematic of the Pockels cell set-up with two GT polarisers. The GT polarisers have their polarisation axis perpendicular to each other. A TTL-controlled pulse generator (DEI) switches the high voltage on and off. When no voltage is applied the second GT polariser sends the light to the beam dump. Turning on the Pockels cell voltage rotates the polarisation and light passes through the set-up.*

number of things can be done to decrease the shutting time of this set-up. First of all is the development of a 55 V driving circuit which could increase the current through the coil. Secondly an optimization of the shutting rod's dimensions could also decrease the shutting time. A 3D-printer can be used to produce a light weight plastic shutting rod with an optimised length. I believe that there is a great potential for this shutter design. However, it is unlikely that it will ever become faster than shutting with an AOM.

3.2.3 The Pockels Cell Set-up

Another set-up for fast light shutting is by use of a Pockels cell and Glan-Thompson (GT) polarisers that have a polarization extinction rate of $1/10^5$. Such a set-up using two GT polarisers and a Pockels cell should be able to achieve shutting with a $1/10^{10}$ extinction ratio in just 50 ns (according to Thorlabs specification), assuming zero polarization pollution from the Pockels cell. The set-up works as follows. The incoming light goes through a GT polariser, insuring a linear polarisation at a ratio of $1/10^5$. Next it goes through the Pockels cell that rotates the polarisation depending on the applied voltage. Then the light goes through the second GT polariser which has its polarisation axis perpendicular to the first GT polariser, giving an extinction ratio of $1/10^{10}$ if the Pockels cell is inert and does not rotate the polarisation. The voltage applied to the Pockels cell is controlled by a pulse generator from DEI designed to drive a capacitive load such as a Pockels cell. It is capable of switching from zero to 3500 V in $\leq$25 ns on a 50 pF load, according to the operations manual.

The Pockels cell works on the basis of the Pockels effect that was discovered by Friedrich Pockels in 1893. What he discovered was that certain transparent materials have an optical dependency on applied electric fields. In this case the material is an anisotropic KH_2PO_4 (KDP) crystal from Thorlabs. This electro-optical effect arises because the electric field causes changes in the material's crystal structure thus changing the reflective index along the crystal axis parallel to the electric field. The Pockels effect is a linear electro-optic effect where the change in the reflective index is proportional to the applied field. The function of the reflective index $n(E)$ can according to [16] be expanded as a Taylor approximation around $E = 0$.

$$n(E) = n - \frac{1}{2} r n^3 E \tag{3.8}$$

Here r is the so called Pockels coefficient, n is the unperturbed reflective index and E is the electric field strength. Typical values for r lie between 10^{-12} and 10^{-10} m/V [16]. In materials such as KDP the higher order terms are negligible, including the second order term, the Kerr effect, which is a quadratic electro-optic effect.

A light beam traversing any material will experience a phase shift due to the change in light speed. This phase shift is given as

$$\phi_0 = 2\pi \frac{nL}{\lambda_0}, \tag{3.9}$$

where λ_0 is the wavelength in free space, n is the refractive index of the material and L is the length of the material. One property of the Pockels cell is that the crystal is anisotropic, meaning that there are different refractive indexes of each axis. By applying the electric field along one axis, the crystal becomes an adjustable wave plate as the phase between different oriented linear polarisations of light can be controlled. Inserting equation (3.8) into the phase expression, we get an expression for the phase shift of the polarisations along two axes of the crystal.

$$\phi_{\parallel} = \phi_0 - \pi r E \frac{n^3 L}{\lambda_0}. \tag{3.10}$$

$$\phi_{\perp} = \phi_0. \tag{3.11}$$

Here $\phi_{\parallel}$ is the phase of light with a polarisation parallel to the applied electric field and $\phi_{\perp}$ is the the phase of light with polarisation perpendicular to the electric field. The phase difference between the two polarisations is then

$$\phi = \phi_{\perp} - \phi_{\parallel} = \pi r E \frac{n^3 L}{\lambda_0}. \tag{3.12}$$

For the crystal to function as a half-wave plate which is the goal in this set-up, the phase difference needs to be $\phi = \pi$. With the electric field being $E = U/d$, the required voltage is then given by

$$U_{\lambda/2} = \frac{d\lambda_0}{Lrn^3}. \tag{3.13}$$

For the Thorlabs EO-PC-550 Pockels cell used in this set-up the halfwave voltage was experimentally optimized to $U_{\lambda/2} = 2.6$ kV.

The Pockels cell has a capacitance of 8 pF, so switching between 0 and 2.6 kV with the DEI pulse generator in less than 25 ns should not be a problem and according to Thorlabs the Pockels cell should have a rise time on the order of 50 ns. This, however showed not to be achievable as the fast switching caused phonons to resonate in the crystal, causing pulses of light to be transmitted following the shut-off. This is shown in figure 3.19. The solution was to implement a resistor in series with the Pockels cell as shown in figure 3.18. This prolongs the switching time making the blow to the crystal softer. In order to minimize the effects of these crystal phonons and still achieve a fast switching time, a number of different resistance values was tried and an optimal resistance of 220 kΩ was found. This together with careful alignment led to a great reduction of crystal phonons and a shutting time of approximately 2.9 μs with an extinction rate of approximately 1/26.5 at 5 μs.

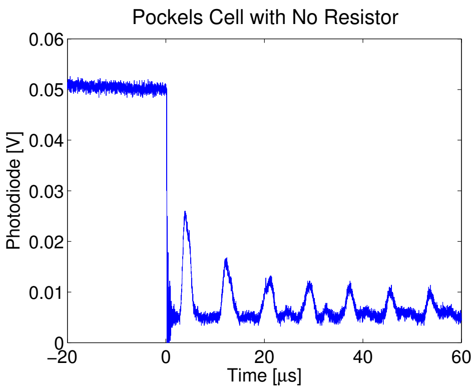

Figure 3.19: *Light intensity during shutting with a Pockels Cell in a set-up as shown in figure 3.18, where the resistor is 0 Ω and* $U_{\lambda/2} = 2.6\ kV$.

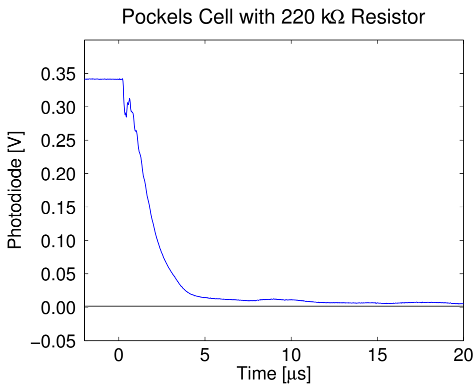

Figure 3.20: *Light intensity during shutting with a Pockels Cell in a set-up as shown in figure 3.18, where the resistor is 220 Ω and* $U_{\lambda/2} = 2.6\ kV$.

3.2.4 Shutter Implementation

The Pockels cell set-up was implemented into the experimental set-up, so that shutting is now done by both the Pockels cell and the AOM. This combination gives an extinction ratio of $1/(240 \times 26.5) = 1/6360$ at 5 μs. With the typical experimental values this would correspond to a Rabi frequency of

$$\Omega = \sqrt{\frac{\Gamma^2 I/6360}{2I_{sat}}} = 47.920\text{kHz}. \tag{3.14}$$

By using

$$P_e = \frac{1}{2}\frac{\Omega^2}{\Omega^2 + \delta^2} \tag{3.15}$$

from [17], which gives the Rabi oscillation amplitude. From this we get an estimation of the highest possible population fraction of the atom in the $^1P_1$-state for a given intensity. 5 μs after shutting, we can expect a maximum of 9.4×10^{-5} % of the cold atoms to be in the $^1P_1$-state, neglecting the effects of the cavity field.

3.3 AOM Stability

One of the contributions to the frequency noise of the probe laser is the AOMs in our set-up. The frequency noise of the VCOs that drives the AOMs is written on the light through the AOM. This problem have been solved by using highly stable HP signal generators to drive the AOMs. These signal generator are used for many purposes in the laboratory and are very expensive. A system where a HP signal generator drives a direct digital synthesizer chip with four channels, allows not only for a high exploitation of the signal generator but also control over the AOMs' mutual phase.

3.3.1 AD9959 Digital Synthesizer

Among the choices on the market of digital synthesizers the most suitable is the AD9959 from Analog Devices. It has 4 individual channels where the phase, amplitude and frequency can be controlled. It is sold as an evaluation kit where the

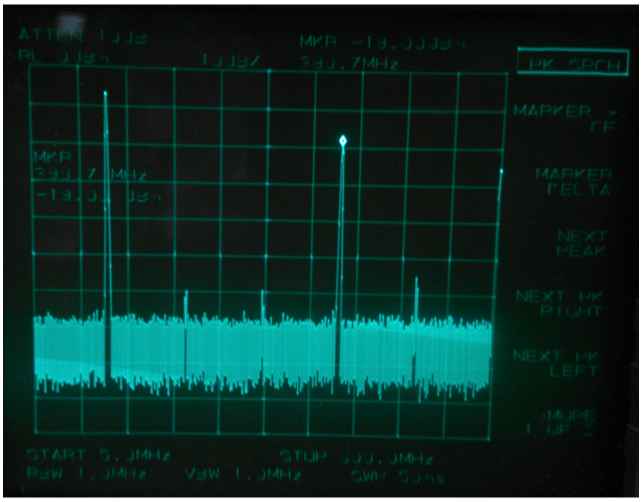

Figure 3.21: *The spectrum of the unfiltered output from the AD9959 chip set to 100 MHz with a 500 MHz chip sampling frequency. The two peaks are at 100 MHz and at 400 MHz. The frequency axis of spectrum is goes from 5 MHz to 600 MHz.*

chip is placed on a board containing all the required electronics for USB interface control through the included software. The software and the USB firmware is only supported by the obsolete Windows XP operating system.

The main disadvantage with this chip is that it only supports a chip clock frequency of up to 500 MHz meaning that according to Nyquist the maximum output is 250 MHz. This is insufficient as the AOM's have to be driven with a frequency between 350 and 400 MHz. The first approach was simple over-clocking where the hope was, that by driving the chip with a 1 GHz chip clock and actively cooling it, would be sufficient to achieve a nice single mode sinusoidal output signal. The over-clocking however showed to create substantial amount of noise throughout the spectrum.

When sampling frequencies, as done by this digital synthesizer, an effect called aliasing occurs. This means the sampled frequency has an "alias" that is mirrored around the Nyquist frequency. By running the chip clock at 500 MHz, the Nyquist frequency will be 250 MHz. Setting a sampling frequency at 100 MHz generates frequency components at both 100 MHz and 400 MHz. The spectrum from AD9959 with these settings is shown on figure 3.21. In hopes of exploiting this characteristic, bandpass filters around the frequency range needed was ordered. Unfortunately there have been some difficulties with the delivery of these filters, resulting in that this set-up has not yet been tested.

In order to ensure that the AD9959 chip do not contribute to much frequency instability, a long term measurement over 11 hours was made. The measurement set-up consisted of two HP8648A frequency generators, which previously was beaten against each other showing a frequency deviation over 5 hours of approximately 5 Hz. In the measurement set-up they were locked together through their 10 MHz reference ports, insuring that their contribution to the frequency deviation was well below 5 Hz. One of the HP frequency generator supplied the 500 MHz chip clock for the AD9959. The output from the AD9959 was set to 100 MHz and sent through the AD9959 evaluation boards 200 MHz low-pass filter and then beaten against the other HP frequency generator at 100.01 MHz. The resulting 10 kHz beat signal was

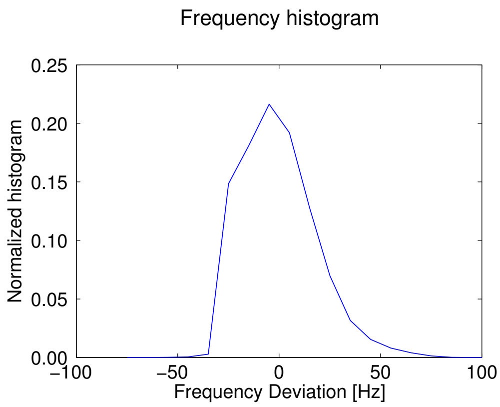

Figure 3.22: *Frequency histogram of a measurement of the AD9959 frequency stability. The frequency standard deviation was found to be 18.5 Hz.*

measured using a Agilent 34461A digital multimeter. Figure 3.22 shows a histogram of this measurement. The frequency standard deviation was found to be 18.5 Hz.

These preliminary investigations into the AD9959 chip shows a great potential for driving all AOMs with one frequency reference.

Chapter 4

Cavity-Enhanced Spectroscopy Using the NICE-OHMS Technique

In this chapter the NICE-OHMS technique is described and the theoretical foundation for analysis of the experimental data is made. This is done through an analysis of the Fabry-Pérot interferometer and considerations on how the atom-light-interaction affect light, ending up with a suggestion for a way to relate the experimental signal voltage to an atom induced phase shift.

4.1 The NICE-OHMS Technique

Light transmitted through a cavity is subject to a substantial amount of noise. This noise is dominated by acoustic vibrations and thermal fluctuation of the cavity mirrors and the medium the mirrors are on. When performing cavity-enhanced spectroscopy on atoms, the cavity noise is directly written on the atoms, meaning the signal from the atom-light-interaction contains this noise. By adding additional light in the cavity, separated in frequency from the original field by the cavity's FSR, the cavity will then contain two standing waves where only one is on resonance with the atoms. This can be described as two cavity fields oscillating as $\cos(\omega_0 t + \phi_a)$ and $\cos((\omega_0 + \Omega)t)$, where ω_0 is the resonance frequency of the atoms and the cavity, Ω is one FSR and ϕ_a is the phase shift due to the atoms. The transmitted light trough such a system will have an intensity that can be interpreted as a beating of the two fields.

Beating of two oscillating signals is a technique that is widely used. It can be described as a multiplication of two signals.

$$S1 = A\cos(\omega_0 t + \phi_a) \qquad\qquad S2 = B\cos((\omega_0 + \Omega)t)$$

Beating these two will give[1]

$$\begin{aligned} U &= S1 \times S2 \\ &= \frac{AB}{2}\left(\cos((2\omega_0 + \Omega)t + \phi) + \cos(\Omega t + \phi_a)\right) \end{aligned} \tag{4.1}$$

The outcome is a signal containing two components, one oscillating with the difference of the two frequencies and one oscillating with the sum of the two frequencies.

[1] Using $\cos(A) \times \cos(B) = \frac{1}{2}(\cos(A-B) + \cos(A+B))$

In the case of the atom-cavity system, it means that the intensity of the transmitted light will have a frequency component with a frequency of one FSR. But more than that, the cavity noise disappears. This is due to the fact that the two waves experience same cavity noise. Beating the two waves and filtering out the high frequency component will result in a signal containing the difference between the waves and the only difference between the waves is the effects of the atoms. This is a simple description of the NICE-OHMS technique. A more rigorous investigation will follow.

As described in chapter 2, an EOM is generating sidebands at one FSR on either side of the probe lasers frequency in the experimental set-up. Therefore the cavity contains three standing waves, which changes the picture. This will be discussed in section 4.3.

4.2 The Fabry-Pérot Interferometer

In order to get a simple but still reasonable description of the cavity, it is assumed that the cavity mirrors are flat and parallel. Furthermore we assume that it is only the inside of the mirrors that reflect the light. The mirrors are characterized by the fraction of field amplitude that is reflected r_1 and r_2 and the transmitted amplitude fraction t_1 and t_2. With these assumptions and simplifications, the cavity reduces to a Fabry-Pérot interferometer, as illustrated in figure 4.1.

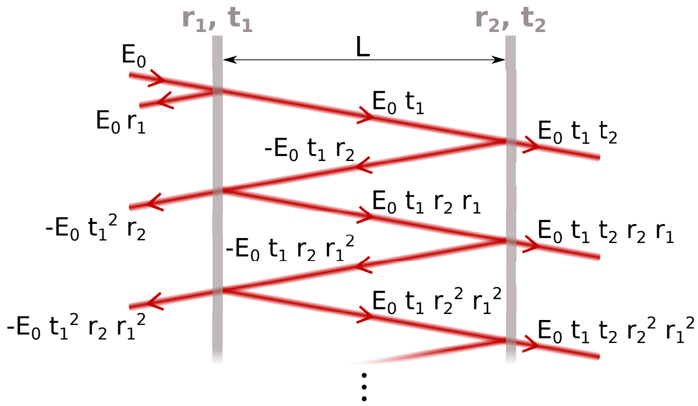

Figure 4.1: *Representation of light on a Fabry-Pérot interferometer. Two flat and parallel mirrors each with reflective (r_1, r_2) and transmittance (t_1, t_2) amplitude coefficients. The amplitude of the incident wave is E_0.*

When performing NICE-OHMS measurements it is the transmitted light that is measured and therefore the most interesting in our case. As shown on figure 4.1 the transmitted wave consists of an infinite number of fractions of the incident wave. The fraction of light that is transmitted directly through has travelled the length of the cavity L and has therefore acquired a phase factor of $\exp(-i\omega L/c)$ upon leaving the cavity compared to the incident wave. We thus define the ligth-cavity phase to be

$$\phi = \omega \frac{L}{c} \tag{4.2}$$

The second largest fraction has travelled a distance of $3L$ and has acquired a phase factor $\exp(-i3\phi)$, and so on and so forth. Thus, the transmitted wave can be written as

$$\begin{aligned} E_T &= E_0 t_1 t_2 e^{-i\phi} + E_0 t_1 t_2 r_2 r_1 e^{-i3\phi} + E_0 t_1 t_2 r_2^2 r_1^2 e^{-i5\phi} + E_0 t_1 t_2 r_2^3 r_1^3 e^{-i7\phi} + \cdots \\ &= E_0 t_1 t_2 e^{-i\phi} \left(1 + r_2 r_1 e^{-i2\phi} + r_2^2 r_1^2 e^{-i4\phi} + r_2^3 r_1^3 e^{-i6\phi} + \cdots \right) \end{aligned} \tag{4.3}$$

The series in the brackets can be rewritten using

$$\sum_{n=0}^{\infty} q^n = \frac{1}{1-q} \qquad \text{where} \qquad q = r_2 r_1 e^{-i2\phi}. \tag{4.4}$$

This results in an expression for the transmitted field

$$E_T = E_0 \frac{t_1 t_2 e^{-i\phi}}{1 - r_2 r_1 e^{-i2\phi}} \tag{4.5}$$

In the case of the experimental set-up the cavity mirrors have the same reflective and transmittance amplitude coefficients, we thus define $r_1 = r_2$, $t_1 = t_2$, $r_1^2 = r_2^2 = R$ and $t_1^2 = t_2^2 = T$. This reduces the expression to

$$E_T = E_0 \frac{T e^{-i\phi}}{1 - R e^{-i2\phi}}. \tag{4.6}$$

The amplitude of this expression is a representation of the intensity of the transmitted light and the angle in the imaginary plane is a representation of the phase shift of the transmitted light. The intensity and phase response of light through a Fabry-Pérot interferometer is shown in figure 4.2.

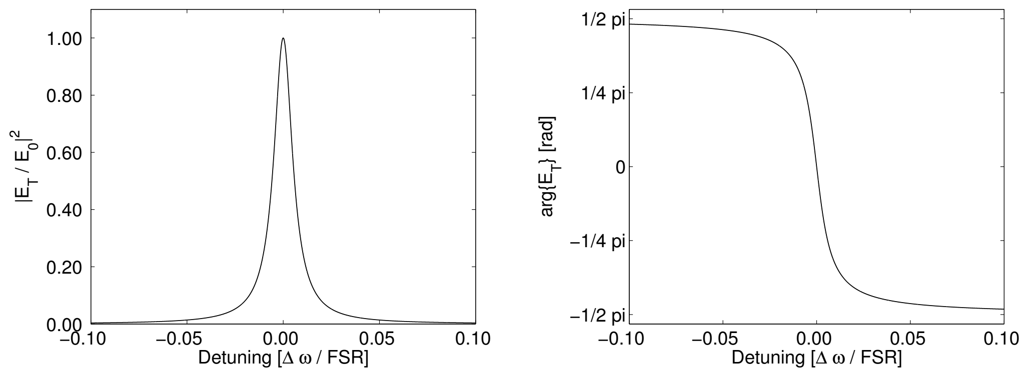

(a) *Intensity factor of the transmitted wave around cavity resonance.*

(b) *Phase shift of the transmitted wave around cavity resonance.*

Figure 4.2: *These plots are for a system where R = 0.96375, T = 1-R and FSR = 500 MHz.*

4.3 Phase Detection

As described in chapter 2 the interest of this study is of a narrow line-width atom in a cavity and as stated just above, the NICE-OHMS technique is used to create a low noise signal of the phase shift of light near atom resonance.

If atoms are introduced into the cavity described, the light will acquire a phase shift as it passes through the atom cloud. This atom induced phase shift is equivalent

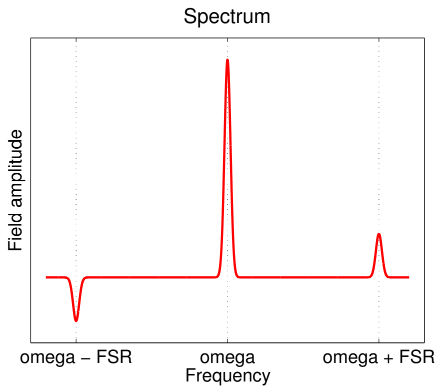

Figure 4.3: *The spectrum of the light incident on the cavity. For visual purposes the line-width and mutual magnitude is exaggerated compared to the experimental values.*

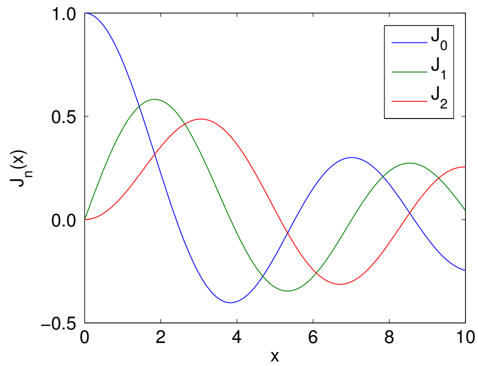

Figure 4.4: *The Bessel functions of the first kind J_0, J_1 and J_2 as a function of the modulation index x. For our EOM the modulation index is about $x = 0.25$.*

to a small change in the effective path length of the light in the cavity. Thus by applying the same logic used in section 4.2, we see that the atomic induced phase shift simply ads to the cavity phase given an expression dependent on atom induced phase shift

$$E_T = E_0 \frac{Te^{-i(\phi+\theta)}}{1 - Re^{-i2(\phi+\theta)}}. \tag{4.7}$$

Here ϕ is the overall cavity phase and θ is an additional phase that the light picks up inside the cavity. If the light is on resonance with the atoms, θ will be the phase shift induced by the atoms.

In our system the light is modulated with an EOM at a frequency equal to the cavity FSR, making the light in the cavity a sum of three different fields, the spectrum of this field is shown in figure 4.3. By assuming that no residual amplitude modulation takes place, the electric field is given by

$$E(t) = E_0 \left[J_0(x)e^{-i\omega t} + \sum_{n=1}^{\infty} (-1)^n J_n(x)e^{-i(\omega+n\Omega)t} \right] + c.c.. \tag{4.8}$$

where $J_n(x)$ is the Bessel function of the first kind. Here x is called the modulation index and it describes how efficiently the EOM generates sidebands. This modulation index depends on the EOM crystal and how RF-voltage is applied. The EOM is basically a crystal with electrodes attached making it a capacitative load of the RF electronics to drive. This means that the EOM together with the BNC cable forms a RC-circuit that has to be optimized in order to achieve a maximum applied RF voltage amplitude across the crystal. By doing this it is possible to achieve a modulation index of about $x = 1$. In our set-up we have no specially optimize electronics driving the EOM, thus giving us a modulation index of about $x = 0.25$ at 500 MHz of modulation frequency. This corresponds to approximately 3 % of the total intensity to be in the first two sidebands.

With a modulation index of $x = 0.25$ we can neglect the higher order Bessel function and by adding the effect of the cavity from equation (4.6) the complex cavity transmitted field can be written as

$$E(t) = E_0 \left[t_c(\phi_0)J_0e^{-i\omega t} + t_c(\phi_{+1})J_1e^{-i(\omega+\Omega)t} + t_c(\phi_{-1})J_1e^{-i(\omega-\Omega)t} \right] + c.c.. \tag{4.9}$$

Here $t_c(\phi_n)$ is the transmitted fraction of the light through the cavity. It is given by

$$t_c(n) = \frac{E_T}{E_0} = \frac{Te^{-i(\phi_n+\theta_n)}}{1 - Re^{-i2(\phi_n+\theta_n)}}, \tag{4.10}$$

The phase ϕ_n is dependent on the light frequency and is now defined with respect to the carrier frequency ω. This frequency is defined as $\omega = 2\pi n FSR$, where $n = c/(\lambda \cdot FSR) = 870827$ and by using $FSR = c/(2L)$ we end up with a phase given as

$$\phi_0 = 2\pi n \frac{L + \Delta L}{L}, \tag{4.11}$$

$$\phi_{-1} = 2\pi(n-1)\frac{L + \Delta L}{L}, \tag{4.12}$$

$$\phi_{+1} = 2\pi(n+1)\frac{L + \Delta L}{L}. \tag{4.13}$$

We have three phase expressions corresponding to the frequencies ω, $\omega - FSR$ and $\omega + FSR$. The parameter ΔL represents a change in the cavity length. This is chosen because when we scan the frequency response of the cavity, the probe laser is fixed in frequency and the cavity length is changed by modulating the piezo-voltage controlling one of the cavity mirrors position. Mathematically and physically there is no difference between scanning by frequency or cavity length. Having $n = 870827$ result in the carrier at frequency ω to be on resonance with the atoms making θ_0 the parameter of interest, where θ_{-1} and θ_{+1} are set to be zero as they are far from resonance with the atoms.

The three frequency components inside the cavity generate a beat signal. To detect this signal the intensity of the transmitted light is measured. In order to determine the signal dependence on the atom induced phase an expression for the intensity must be known. The intensity is given by

$$\begin{aligned}
I(t) =& |E(t)|^2 \\
=& E_0^2 \big[t_c(\phi_0)t_c^*(\phi_0)J_0^2 + t_c(\phi_{+1})t_c^*(\phi_{+1})J_1^2 + t_c(\phi_{-1})t_c^*(\phi_{-1})J_1^2 + \\
& t_c(\phi_0)t_c^*(\phi_{+1})J_0J_1e^{i\Omega t} + t_c(\phi_0)t_c^*(\phi_{-1})J_0J_1e^{-i\Omega t} + \\
& t_c^*(\phi_0)t_c(\phi_{+1})J_0J_1e^{-i\Omega t} + t_c(\phi_{+1})t_c^*(\phi_{-1})J_0J_1e^{-i2\Omega t} + \\
& t_c^*(\phi_0)t_c(\phi_{-1})J_0J_1e^{i\Omega t} + t_c(\phi_{-1})t_c^*(\phi_{+1})J_0J_1e^{i2\Omega t} \big] \\
\\
=& E_0^2 \big[t_c(\phi_0)t_c^*(\phi_0)J_0^2 + t_c(\phi_{+1})t_c^*(\phi_{+1})J_1^2 + t_c(\phi_{-1})t_c^*(\phi_{-1})J_1^2 + \\
& \left(t_c(\phi_0)t_c^*(\phi_{+1}) + t_c^*(\phi_0)t_c(\phi_{-1})\right) J_0J_1e^{i\Omega t} + \\
& \left(t_c^*(\phi_0)t_c(\phi_{+1}) + t_c(\phi_0)t_c^*(\phi_{-1})\right) J_0J_1e^{-i\Omega t} + \\
& t_c(\phi_{+1})t_c^*(\phi_{-1})J_1^2e^{-i2\Omega t} + t_c(\phi_{-1})t_c^*(\phi_{+1})J_1^2e^{i2\Omega t} \big]
\end{aligned} \tag{4.14}$$

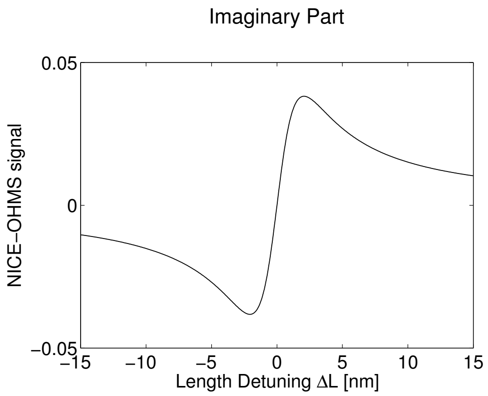

(a) *The imaginary part of the NICE-OHMS signal as the cavity length is scanned.*

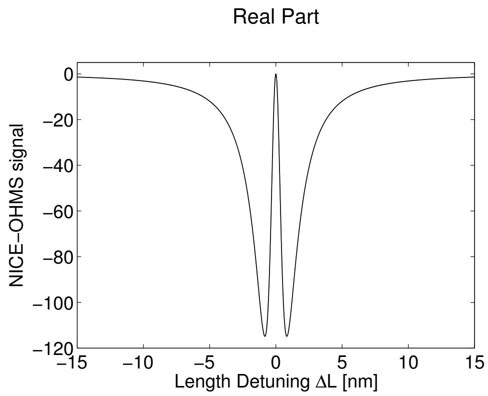

(b) *The real part of the NICE-OHMS signal as the cavity length is scanned.*

Figure 4.5: *These plots are for a system where R = 0.96, T = 1-R and FSR = 500 MHz. The y-axis is in some arbitrary unit due to some numerical computation scaling off-set.*

The intensity consists of three components. First there is a number of constant terms, secondly there are two terms oscillating at the modulation frequency Ω and thirdly there are two terms oscillating at 2Ω. This intensity is what is incident on the photo detector and the signal must thus be proportional to this expression. At this point in the set-up a band-pass filter filters out frequencies around the modulation frequency. Thus it is safe to assume that all other components than those oscillating with Ω are filtered out. The terms left are rewritten by using that if $A = a + ib$ then $Ae^{i\Omega t} + A^*e^{-i\Omega t} = 2a\cos(\Omega t) - 2b\sin(\Omega t)$.

$$I(t) = E_0^2 J_0 J_1 2 \left[\mathrm{Re}\{t_c(\omega)t_c^*(\omega+\Omega) + t_c^*(\omega)t_c(\omega-\Omega)\}\cos(\Omega t) - \mathrm{Im}\{t_c(\omega)t_c^*(\omega+\Omega) + t_c^*(\omega)t_c(\omega-\Omega)\}\sin(\Omega t)\right] \quad (4.15)$$

This expression describes the signal from the diode that is put into the mixer as shown in chapter 2 figure 2.14. The function of the mixer is to demodulate the signal by beating it against the modulation frequency as described by equation (4.1). By changing the phase between the diode signal and the modulation frequency, either the cosine part or the sine part of equation (4.15), or some combination of the two, can be chosen. Another way to look at it, is to say that we choose whether to see the real part or the imaginary part of this expression. Figure 4.5 shows plots of the imaginary and real part of the NICE-OHMS signal as the cavity length is scanned and with $\theta = 0$.

The resulting signals from a locked cavity scanning the atomic induced phase looks to be identical, though a thorough investigation of this have not yet been done due to numerical difficulties when computing these equations. The output signal from the mixer is chosen on the basis of pure convention as the experimental parameters originally set a mixer phase choosing the imaginary part. I continue the analysis with the imaginary part that is given by

$$\begin{aligned} S =& \mathrm{Im}\{t_c(\phi_0)t_c^*(\phi_{+1}) + t_c^*(\phi_0)t_c(\phi_{-1})\} \\ =& \mathrm{Im}\left\{\frac{Te^{-i(\phi_0+\theta_0)}}{1-Re^{-i2(\phi_0+\theta_0)}}\frac{Te^{i\phi_{+1}}}{1-Re^{i2\phi_{+1}}} + \frac{Te^{i(\phi_0+\theta_0)}}{1-Re^{i2(\phi_0+\theta_0)}}\frac{Te^{-i\phi_{-1}}}{1-Re^{-i2\phi_{-1}}}\right\} \\ =& \mathrm{Im}\left\{\frac{T^2e^{-i(\phi_0-\phi_{+1}+\theta_0)}}{(1-Re^{-i2(\phi_0+\theta_0)})(1-Re^{i2\phi_{+1}})} + \frac{T^2e^{i(\phi_0-\phi_{-1}+\theta_0)}}{(1-Re^{i2(\phi_0+\theta_0)})(1-Re^{-i2\phi_{-1}})}\right\} \end{aligned} \tag{4.16}$$

In order to utilize this equation for data analysis it is a requirement the it can be plotted and fitted to data. But as the ϕ_n parameters have very large values it is difficult for a computer to do numerical calculations. To circumvent this problem a Taylor approximation is done. To this accord the ϕ_n parameters are replaced by $\delta\phi_n$ which is defined as the phase detuning thus moving the values to be around zero:

$$\delta\phi_0 = 2\pi n\frac{L+\Delta L}{L} - n\pi, \tag{4.17}$$

$$\delta\phi_{-1} = 2\pi(n-1)\frac{L+\Delta L}{L} - n\pi, \tag{4.18}$$

$$\delta\phi_{+1} = 2\pi(n+1)\frac{L+\Delta L}{L} - n\pi. \tag{4.19}$$

Note that the difference between ϕ_0 and ϕ_{-1} and ϕ_0 and ϕ_{+1} remains the same through this transformation. The Taylor approximation can then be done around $\delta\phi_0 = 0$:

$$\begin{aligned} S \approx& \mathrm{Im}\left\{\frac{T^2(1-i(\delta\phi_0-\delta\phi_{+1}+\theta_0))}{(1-R(1-i2(\delta\phi_0+\theta_0)))(1-R(1+i2\delta\phi_{+1}))}+\right. \\ & \left.\frac{T^2(1+i(\delta\phi_0-\delta\phi_{-1}+\theta_0))}{(1-R(1+i2(\delta\phi_0+\theta_0)))(1-R1(-i2\delta\phi_{-1}))}\right\} \end{aligned} \tag{4.20}$$

This is a very poor approximation as only $\delta\phi_0$ is close to zero. However, by expanding the approximation to second order it is possible to fit the equation to our data. Figure 4.6 shows the NICE-OHMS signal as the cavity length is scanned. The fit was achieved with the parameters in table 4.1 where A is an overall scaling parameter and the parameter dl is correcting for drifts in the cavity length L by being inserted as

$$\delta\phi_n = 2\pi n\frac{L+dl+\Delta L}{L+dl} - n\pi. \tag{4.21}$$

Using these fitting parameters the second order Taylor approximation of equation (4.16) can now be plotted as a function of the atom induced phase. As done by the Hänsch-Couillaud cavity lock the expression is locked to resonance by setting $\Delta L = 0$. Figure 4.7 shows this plot with a linear fit to the centre, which can be used as a direct conversion between the measured voltage out of the mixer to the atom induced phase

$$\theta_0 = \frac{U - 0.01315\ \mathrm{V}}{6.242\ \mathrm{V/rad}}, \tag{4.22}$$

where U is the measured voltage out of the mixer. Through this procedure is thus possible to find the absolute phase induces by a cloud of atoms in a cavity.

A	1.383758
R	0.961253
y-offset	0.013134205459493
Loss	0.001284
dl	48.055869×10^{-9}

Table 4.1: *The fitting parameters used in the fit shown in figure 4.6, where A is an overall scaling parameter, dl is a parameter to account of cavity length drift and T = 1 - R - Loss.*

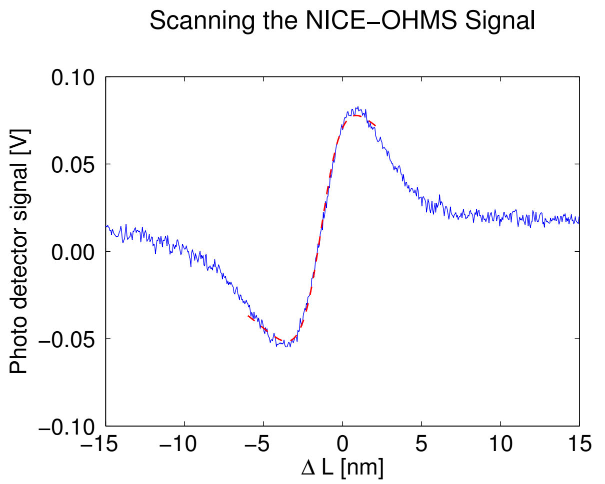

Figure 4.6: *A scan of the NICE-OHMS signal by modulating the cavity length. The red curve is a fit to a second order Taylor approximation of equation* (4.16).

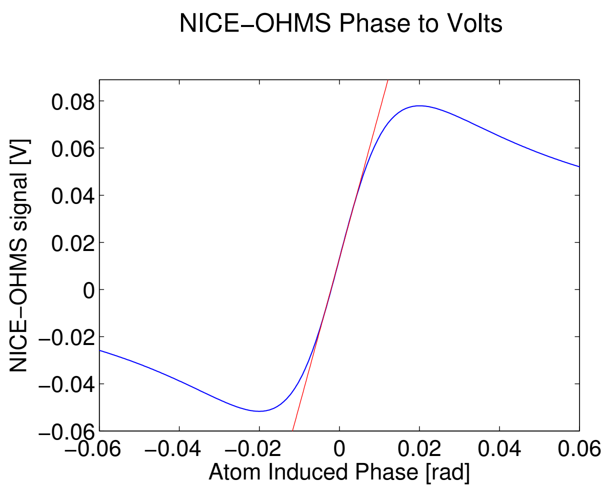

Figure 4.7: *The second order Taylor approximation of equation (4.16) plotted against the atom induced phase with the parameters in table 4.1. The red line is linear fit giving a voltage to phase conversion factor.*

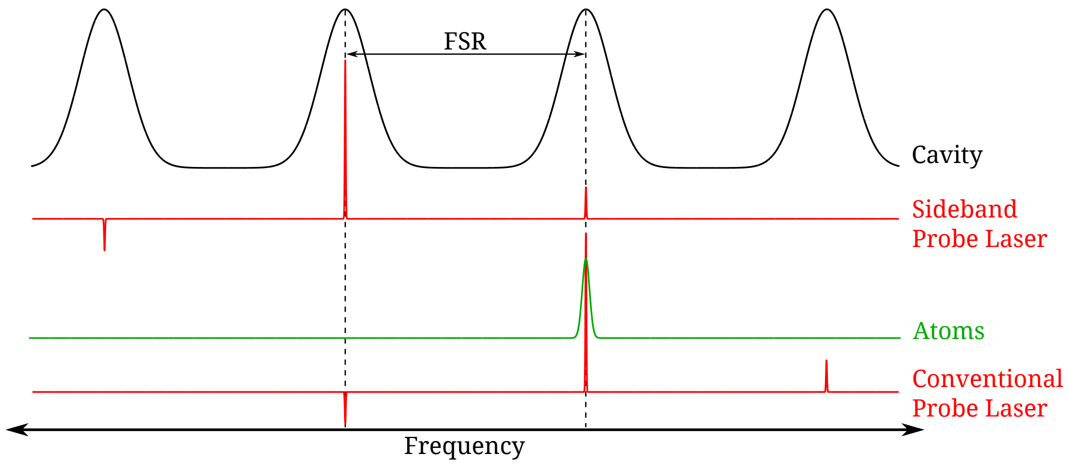

Figure 4.8: *Spectral overview of the NICE-OHMS measurement. Showing both conventional carrier probing and sideband probing. The spectral widths of the spectra are exaggerated for visual purposes. The magnitude of the sidebands on the probing laser is approximately 1.5 % of the carrier.*

4.3.1 Sideband Measurements

One of the parameters that have shown to be of interest is the intensity of the cavity field. In order to achieve a greater range of cavity probing power a scheme where the whole probing spectrum is moved down one cavity FSR have been configured. In doing this it becomes a sideband that is on resonance with the atoms instead of the carrier. In this way the effective cavity field as seen by the atoms is reduced as the intensity of the sidebands is about 1.5 % of the carrier intensity. The cavity is still lock to the carrier, making it possible to maintaining a tight cavity lock at low interrogation intensities. A spectral overview comparing this configuration to the conventional probing configuration is shown in figure 4.8. For such a system the absolute phase can be found by the same procedure as just described with only small changes to equation (4.16). These follows from the fact that it is the upper sideband that interacts with the atoms, meaning that θ_{+1} now is the parameter of interest and θ_{-1} and θ_0 is set to be zero. This changes equation (4.16) to

$$S = \mathrm{Im}\left\{\frac{T^2 e^{-i(\phi_0-\phi_{+1}+\theta_{+1})}}{(1-Re^{-i2\phi_0})(1-Re^{i2(\phi_{+1}+\theta_{+1})})} + \frac{T^2 e^{i(\phi_0-\phi_{-1})}}{(1-Re^{i2\phi_0})(1-Re^{-i2\phi_{-1}})}\right\}, \tag{4.23}$$

where the phase parameters ϕ_n change to

$$\phi_0 = 2\pi(n-1)\frac{L+\Delta L}{L}, \tag{4.24}$$

$$\phi_{-1} = 2\pi(n-2)\frac{L+\Delta L}{L}, \tag{4.25}$$

$$\phi_{+1} = 2\pi(n)\frac{L+\Delta L}{L}. \tag{4.26}$$

With these changes the procedure to find the absolute phase is the same as with conventional probing, where a conversion factor is found through fitting a scan of the cavity length and then using the fitted parameters in equation (4.23).

4.4 Conventional NICE-OHMS Analysis

By looking at the system when the cavity is locked to resonance, i.e. the probe laser frequency, the expression describing the NICE-OHMS signal simplifies significantly. The following analysis will make it more transparent what we really measure and what parameters the measurements depend on. We still have a system where the modulation frequency is one FSR, giving us three standing waves in the cavity. The following analysis is similar to the description in [18] and it will make it clearer exactly what information can be extracted from our system using the NICE-OHMS technique.

4.4.1 Probing with the Carrier

Having the carrier on resonance with the atoms means that only the J_0 component in equation 4.8 will be attenuated and phase shifted. Thus, after the electric field have interacted with the atoms it can be written as

$$\begin{aligned} E(t) &= E_0 \left(J_0 e^{-\alpha_0} e^{-i(\omega t - \theta_0)} + J_1 e^{-i(\omega+\Omega)t} - J_1 e^{-i(\omega-\Omega)t} + c.c. \right) \\ &= 2E_0 \left(J_0 e^{-\alpha_0} \cos(\omega t - \theta_0) + J_1 \cos((\omega+\Omega)t) - J_1 \cos((\omega-\Omega)t) \right). \end{aligned} \tag{4.27}$$

Here α_0 and θ_0 are the atomic induced field attenuation and phase shift respectively. In the experimental set-up the intensity of this field is measured by the fast photo diode detector D2 (see figure 2.14). The RF signal out of the detector is proportional to the intensity given by

$$\begin{aligned} S_{D2} \propto 4E_0^2 \big[& J_0^2 e^{-2\alpha_0} \cos(\omega t - \theta_0)^2 + J_1^2 \cos((\omega+\Omega)t)^2 + J_1^2 \cos((\omega-\Omega)t)^2 \\ & + 2J_0 J_1 e^{-\alpha_0} \cos((\omega+\Omega)t) \cos(\omega t - \theta_0) \\ & - 2J_0 J_1 e^{-\alpha_0} \cos((\omega-\Omega)t) \cos(\omega t - \theta_0) \\ & -2J_1 J_1 \cos((\omega+\Omega)t) \cos((\omega-\Omega)t) \big]. \end{aligned} \tag{4.28}$$

By using the trigonometric relation $\cos(A)\cos(B) = \frac{1}{2}(\cos(A-B) + \cos(A+B))$, the expression can be rewritten as

$$\begin{aligned} = 4E_0^2 \big[& J_0^2 e^{-2\alpha_0} \cos(\omega t - \theta_0)^2 + J_1^2 \cos((\omega+\Omega)t)^2 + J_1^2 \cos((\omega-\Omega)t)^2 \\ & + J_0 J_1 e^{-\alpha_0} \left(\cos(\Omega t + \theta_0) + \cos((2\omega+\Omega)t - \theta_0) \right) \\ & - J_0 J_1 e^{-\alpha_0} \left(\cos(-\Omega t + \theta_0) + \cos((2\omega-\Omega)t - \theta_0) \right) \\ & -J_1 J_1 \left(\cos(2\Omega t) + \cos(2\omega t) \right) \big]. \end{aligned} \tag{4.29}$$

At this point in the experiment we beat the detector signal and the RF signal driving the EOM through a mixer as described in section 4.1. This corresponds to demodulating the signal in equation (4.29) at the frequency Ω. The phase between the

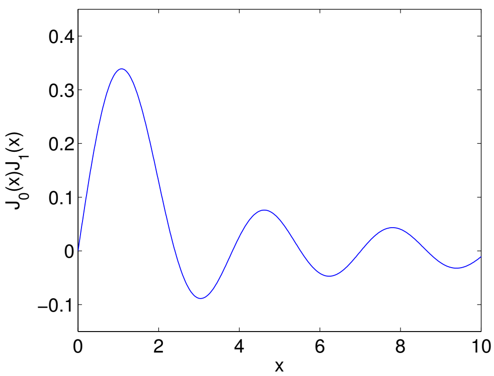

Figure 4.9: *A plot of the product of the Bessel functions J_0 and J_1 as a function of the modulation index. The maximum of this product is obtained for a modulation index of* $x = 1.1$.

EOM signal generator and the detector signal is optimized and the high frequency components are filtered out. This gives a signal out of the mixer:

$$
\begin{aligned}
S_M &\propto S_{D2} \times \cos(\Omega t + \phi_M) \\
&= 2E_0^2 \left[J_0 J_1 e^{-\alpha_0} (\cos(\theta_0 - \phi_M) + \cos(2\Omega t + \theta_0 - \phi_M)) \right. \\
&\quad - J_0 J_1 e^{-\alpha_0} (\cos(\theta_0 + \phi_M) + \cos(2\Omega t - \theta_0 + \phi_M)) \\
&\quad \left. - J_1 J_1 (\cos(\Omega t - \phi_M) + \cos(3\Omega t + \phi_M)) \right]
\end{aligned} \tag{4.30}
$$

$$\Downarrow$$

$$\text{Low-pass filter and } \phi_M = -\pi/2$$

$$\Downarrow$$

$$= 4E_0^2 J_0 J_1 e^{-\alpha_0} \sin(\theta_0) \tag{4.31}$$

The measured signal is thus a product of the field attenuation and sine of the phase shift. For the weak transition we probe here we assume $e^{-\alpha_0} \simeq 1$ and as the phase shift induced by the atoms is small $\sin(\theta_0) \approx \theta_0$. The signal measured is thus through these approximations a measure of the phase shift induced by the atoms.

The factor of $J_0 J_1$ in the signal expression gives a way to optimize the signal through the modulation index. Figure 4.9 shows $J_0 J_1$ as a function of the modulation index, where a maximum is found at a modulation index of $x = 1.1$. Currently we have a modulation index of only 0.2 due to low efficiency of the EOM at 500 MHz. This modulation index corresponds as previous stated to 1.5 % of the carrier power in each sideband.

4.4.2 Probing with Low Power Using a Sideband

By shifting the probe laser one FSR down in frequency is becomes a sideband that is on resonance with the atoms. This results in a reduction of the probing power to approximately 1.5 % of carrier power. We can thus achieve a low interaction intensity without any cost to our signal strength, while maintaining a tight cavity lock to the strong carrier. The field when probing with the upper sideband is

$$E(t) = 2E_0 \left(J_0 \cos(\omega t) + J_1 e^{-\alpha_0} \cos((\omega+\Omega)t - \theta_0) - J_1 \cos((\omega-\Omega)t)\right). \quad (4.32)$$

The signal on the photo diode then becomes proportional to:

$$\begin{aligned} S_{PD} \propto 4E_0^2 \big[&J_0^2 \cos(\omega t)^2 + J_1^2 e^{-2\alpha_0} \cos((\omega+\Omega)t-\theta_0)^2 + J_1^2 \cos((\omega-\Omega)t)^2 \\ &+ 2J_0 J_1 e^{-\alpha_0} \cos((\omega+\Omega)t-\theta_0)\cos(\omega t) \\ &- 2J_0 J_1 \cos((\omega-\Omega)t)\cos(\omega t) \\ &- 2J_1 J_1 e^{-\alpha_0} \cos((\omega+\Omega)t-\theta_0)\cos((\omega-\Omega)t)\Big]. \end{aligned} \quad (4.33)$$

By using the trigonometric relation $\cos(A)\cos(B) = \frac{1}{2}(\cos(A-B) + \cos(A+B))$ we can rewrite it to

$$\begin{aligned} = 4E_0^2 \Big[&J_0^2 e^{-2\alpha_0} \cos(\omega t - \theta_0)^2 + J_1^2 \cos((\omega+\Omega)t)^2 + J_1^2 \cos((\omega-\Omega)t)^2 \\ &+ J_0 J_1 e^{-\alpha_0} (\cos((2\omega+\Omega)t-\theta_0) + \cos(\Omega t - \theta_0)) \\ &- J_0 J_1 (\cos((2\omega-\Omega)t) + \cos(-\Omega t)) \\ &- J_1 J_1 e^{-\alpha_0} (\cos(2\omega t - \theta_0) + \cos(2\Omega t + \theta_0))\Big]. \end{aligned}$$

And again filtering out the high frequency components gives

$$= 4E_0^2 \left[J_0 J_1 (e^{-\alpha_0} \cos(\Omega t - \theta_0) - \cos(-\Omega t)) - J_1 J_1 e^{-\alpha_0} \cos(2\Omega t + \theta_0)\right]. \quad (4.34)$$

Then the demodulation by use of the mixer

$$\begin{aligned} S_M &\propto S_{D2} \times \cos(\Omega t + \phi_M) \\ &= 2E_0^2 \big[J_0 J_1 \big(e^{-\alpha_0}(\cos(-\theta_0 - \phi_M) + \cos(2\Omega t - \theta_0 + \phi_M)) \\ &\qquad\qquad - (\cos(-2\Omega t - \phi_M) + \cos(\phi_M)\big) \\ &\qquad - J_1 J_1 e^{-\alpha_0} (\cos(\Omega t + \theta_0 - \phi_M) + \cos(3\Omega t + \theta_0 + \phi_M))\,\big] \quad (4.35) \\ &\qquad \Downarrow \\ &\quad \text{Low-pass filter and } \phi_M = \pi/2 \\ &\qquad \Downarrow \\ &= 2E_0^2 J_0 J_1 e^{-\alpha_0} \sin(\theta_0) \quad (4.36) \end{aligned}$$

If we compare this to the case where the carrier was on resonance with the atoms, the signal has dropped by a factor of two. This is because only one of the sidebands are contribution to the signal. However, in the analysis of the signal so far we have neglected the potential importance of the finite absorption. This may be to crude an approximation.

If we shift the phase between the RF signal driving the EOM and the photo diode detector by 90 degrees so that $\phi_M = \pi$ the signal then becomes

$$S_M \propto 2E_0^2 J_0 J_1 (1 - e^{-\alpha_0} \cos(\theta_0)) \tag{4.37}$$

If we as before assume the atom induced phase θ_0 to be small, then $\cos(\theta_0) \approx 1$ and the signal is thus proportional to the absorption. In this way the NICE-OHMS technique should be able to give a transmission signal with the same signal-to-noise ratio as the phase signal.

Chapter 5

Experimental Results

As described in chapter 2 it is the complex amplitude of the cavity transmitted field consisting of phase and transmission profiles induced by the atoms that constitutes our measured observables. Experimentally, we explore the phase response of the atoms as a function of atom-cavity detuning at 3 mK sample temperature. Based on the desire for a better understanding of our measurements at finite temperature, we have collaborated with Murry Holland and his theory group at JILA, University of Colorado. The outcome of this new theory and consideration in comparing this with our previous understanding is discussed in this chapter.

A presentation of some of the experimental data is given. This including a discussion of different system parameters. Here the dependence on the cavity input power and on the number of atoms in the cavity field are investigated.

In the theoretical model developed at JILA, an assumption of steady-state interaction has been made. In order to investigate the accuracy of this assumption I have taken data showing the time-evolution of the system. I also calculate the time evolution of the density matrix describing a three level system using the Optical Bloch Equations (OBE). This three level system contains both the $^1S_0$ - $^1P_1$ cooling transition and the $^1S_0$ - $^3P_1$ probing transition, so to include effects of the MOT beams on the probing transition.

5.1 Theory

The theoretical models describing systems such as ours have previously assumed a non-thermal atom cloud of zero temperature [6], where collective effects among the atoms is dominant in describing the system and thus in considerations on how to optimize an error signal for laser stabilisation. Recently Murray Holland and his theory group at JILA, University of Colorado, has developed a more extensive model describing atoms with finite temperatures, where the behaviour of the system is completely different from the $T = 0$ case.

5.1.1 Collective Atomic Interaction

The idea for our experiment was originally based on the theoretical model describing a system in the limit $T = 0$ with a zero temperature atom cloud and a low cavity field intensity. Here several solutions for a steady-state cavity field exists [6]. This is known as optical bi-stability and arises due to a collective coupling between the atoms and the cavity field. The degree of atom-light coupling is given by the dimensionless

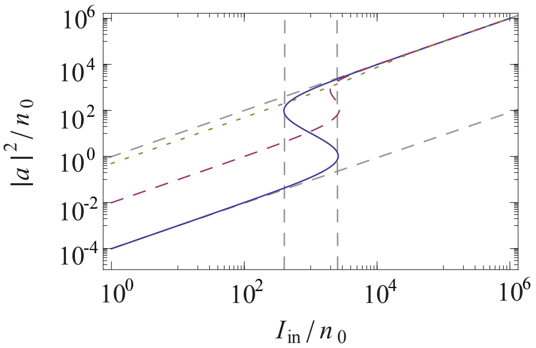

Figure 5.1: *The intra-cavity photon number $|a|^2$ versus the cavity input intensity for a cooperativity $C = 100$ and atom-cavity detuning $\Delta = 0$ (blue line), $\Delta = 10T_2^{-1}$ (purple dashed line) and $\Delta = 100T_2^{-1}$ (yellow dotted line). Here T_2^{-1} is the atomic dipole decay rate, n_0 is the saturation photon number. (Taken from [6]).*

number $C = NC_0 = Ng^2/(\Gamma\kappa)$, where g is the coupling constant and Γ and κ are the decay rate of the atomic dipole and the cavity field respectively.

In figure 5.1 the intra-cavity photon number is shown in relation to cavity input field intensity. This can be divided op into three different domains. The case where $I_{in} < 4C$ the far detuned field $\Delta > \Gamma$ shows little reduction in the intra-cavity field as the atom-cavity interaction is very weak. For $\Delta \approx 0$ the intra-cavity intensity is reduced by a factor of $1/C^2$ compared to an empty cavity. Increasing the input intensity and going to $I_{in} > C^2/4$, the atoms becomes saturated and thus transparent to the cavity field. The solution is thus similar to an cavity. In domain between these two intensities $4C < I_{in}C^2/4$ a new behaviour of the intra cavity field emerges as three distinct solutions for the cavity field exists. Here two of the solution are stable; the low intensity branch where the atomic transition is unsaturated and a high intensity branch where it is saturated.

Utilizing the collective effect that exists in this system, it is shown in [6] that a laser stabilization to the non-linear resonance feature can reach a linewidth on the range of 1 mHz when using ^{87}Sr. However, it turns out to be impossible to operate in this region where $T = 0$. For finite temperature, as in our case, the bi-stability disappears [19], making it possible utilize these collective effects.

5.1.2 The Murray Holland Theory

When changing to a finite temperature the picture changes significantly as the optical bi-stability ceases above a critical temperature. For our parameters this critical temperature is on the order of a few hundred nK, where our experiment operates at a few mK. We are thus far from a system where optical bi-stability exists and therefore we adopted a model describing a thermal system.

The model developed by Murray Holland describes a collection of thermal two-level atoms inside a single mode optical cavity. The Hamiltonian $\hat{H}$ describing the coherent evolution of N atoms with a given velocity v_j coupled to a cavity field mode is given as

$$\hat{H} = \underbrace{\frac{\hbar\Delta}{2}\sum_{j=1}^{N}\hat{\sigma}_j^z}_{\text{Atomic state}} + \underbrace{\hbar\eta(\hat{a}^\dagger + \hat{a})}_{\text{Cavity state}} + \underbrace{\hbar\sum_{j=1}^{N} g_j(t)(\hat{a}^\dagger\hat{\sigma}_j^- + \hat{\sigma}_j^+\hat{a})}_{\text{Coupling}}, \tag{5.1}$$

where $\Delta = \omega_0 - \omega_c$ is the detuning between the atoms and the cavity field, $\sigma_j^{+,-,z}$ is the Pauli spin matrices, η is the classical drive amplitude and $\hat{a}$ is the cavity mode annihilation operator. As mentioned, this model includes the motional effect of the atoms through the Doppler effect, it also include the spatial distribution of both the atoms and the cavity field. The model dose not include the momentum change of the atoms as they absorb or emit photons. As multi-photon scattering events dependent on the atomic velocities are believed to take place for low velocity atoms, the velocity groups involved these scattering events could after a finite time period be emptied. This is due to the atomic momentum change exerted by the photons involved in these low velocity scattering processes. As this is not accounted for in this theory, it is possible that the picture in the theory is incomplete.

5.1.3 Dopplerons

The non-zero velocity of the atoms gives rise to multi-photon scattering where so-called Doppleron resonances take place [19, 20]. An atom with a finite velocity component parallel to the cavity field will, in its own reference frame, experience a bi-chromatic field due to the Doppler effect. At a given detuning the atoms can undergo a non-linear process in which they absorb $(p + 1)$ photons from one direction and emit p photons in the opposite direction, thus leaving the atom in the exited state. It can be described as follows. In an atom's rest frame the cavity will contain two waves, one oscillating with $\omega_+ = \omega_l + kv$ and one oscillating with $\omega_- = \omega_l - kv$, where ω_l is the cavity field frequency in the laboratory rest frame and v is the velocity component parallel to the cavity field. For an atom moving toward the right cavity mirror the photons in the field with frequency ω_+ will be travelling towards the left cavity mirror and the photons in the field with frequency ω_- will be travelling towards the right cavity mirror. The Dopplerons are created when the atom absorbs $(p + 1)$ photons from one direction and emits p photons into the other direction. In figure 5.2 the case of $p = 1$ is shown. At some given detuning $\Delta = \omega_0 - \omega_l$ the atom absorbs two photons from the ω_+ field and emits one photon in the ω_- field. For energy conservation to be fulfilled we must have

$$\omega_0 = (p + 1)\omega_+ - p\omega_- \tag{5.2}$$

from which we get

$$\begin{aligned}
\omega_0 =& p(\omega_l + kv) + \omega_l + kv - p(\omega_l - kv) \\
\omega_0 =& 2pkv + kv + \omega_l \\
\Delta =& (2p + 1)kv \\
v =& \pm \frac{\Delta}{(2p + 1)k}.
\end{aligned} \tag{5.3}$$

This equation gives specific resonance velocities for the atoms at a given detuning as it was originally reported in [20]. Later it was reported in [21], that having the generalized Rabi frequency instead of the detuning will give a more accurate modelling of the Doppleron resonances. We see that in the zero order case of $p = 0$ we are left with the standard Doppler effect, but in the first order case for $p = 1$ sidebands are generated to the cavity field at $\omega_l \pm kv$, where v is given by equation (5.3). As the order of the Dopplerons increase the process becomes more and more unlikely to occur.

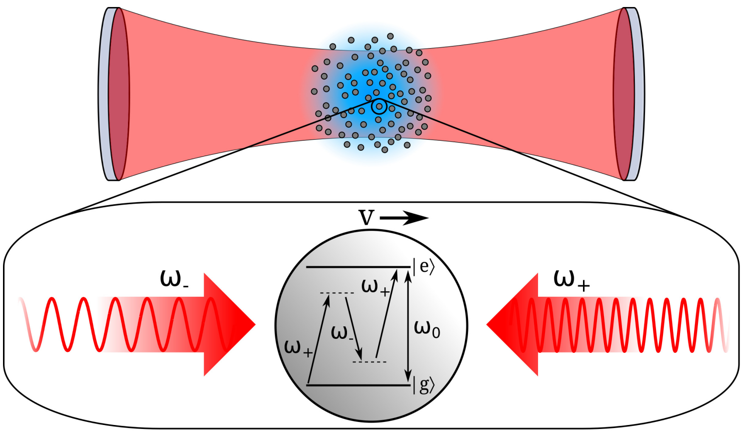

Figure 5.2: *An atom travelling at a velocity v parallel to the cavity field can experience a non-linear multi photon scattering process where Dopplerons are created. Here $\omega_+ = \omega_l + kv$ and $\omega_- = \omega_l - kv$.*

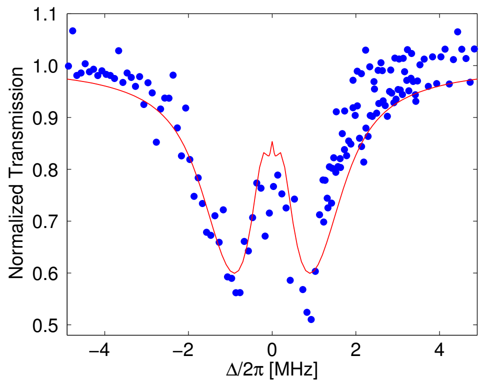

Figure 5.3: *A comparison between the theoretical transmission and measured transmission data with a total number of atoms in the MOT of 4.4×10^8 at a temperature of 4.7 mK and a cavity input power of 975 nW.*

These Doppleron resonances changes the transmitted field amplitude around resonance. A plot of the transmitted field simulated on basis of the theory is shown in figure 5.3. This plot is from a simulation with 4.4×10^8 atoms at a temperature of 4.7 mK and a cavity input power of 975 nW. With these parameters there are three spectral features that can be identified. The broad feature, approximately 3 MHz wide, is the zero order Doppler broadening consistent with an atomic temperature of a 4.7 mK. The central region, with a width of 1 MHz, is due to an enhanced transmission as the atomic sample saturates. Finally, there is a small feature just around resonance. This is the Doppleron contribution from the atoms with small velocities parallel to the cavity field. Exactly on resonance the Doppleron contribution vanishes and the signal is controlled mostly by usual saturated absorption.

5.2 Data

Data from a typical measurement is shown in figure 5.4. The cavity transmission signal from detector D1 (see fig. 2.14) is shown in figure 5.4a and the NICE-OHMS

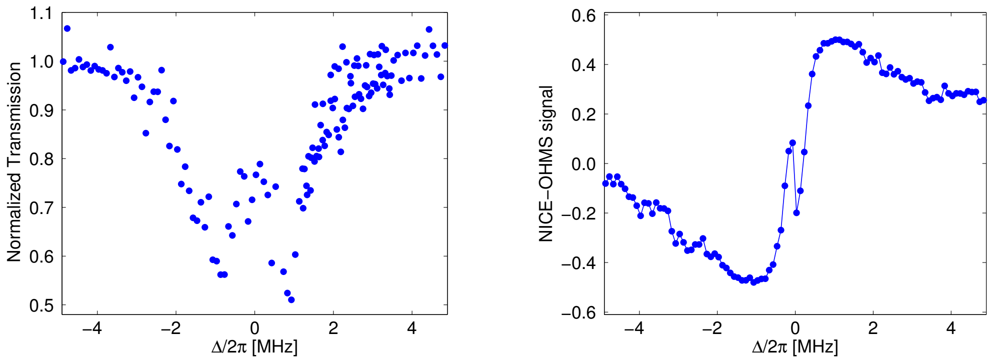

(a) *Transmission signal from detector D1 in the experimental set-up.*

(b) *NICE-OHMS signal (phase) using the fast detector D2 in the experimental set-up.*

Figure 5.4: *Data from a typical frequency scan without any averaging. These data are for an input probe power of 975 nW and a total number of atom in the MOT of 4.4 $\times$ 10^8.*

signal as described in section 4.4 is shown in figure 5.4b. The directly measrured transmission is found to a signal-to-noise ratio of 400 at one second of intergration. The NICE-OHMS signal is far superior in this aspect as the signal-to-noise ratio is 7000 at one second of intergration.

5.2.1 Power Dependence

To characterise the physical system experimentally we have performed a series of measurements to map out the dependence of the cavity input power for a fixed number of atoms. Figure 5.5 shows the power evolution of the transmission and phase response as described by the theoretical model. We see that for high input powers the saturation of the transition leads to power broadening. This power broadening occurs because the saturation of the atoms is far greater on resonance than off resonance, leading to a flattening of the Lorentzian absorption profile resulting in an effective linewidth broadening. This is evident in the phase response, where the slope of the central feature enhances as the input power is gradually lowered. We are thus able to optimize the slope without any reduction in the signal-to-noise ratio through an easily accessible parameter.

Interestingly, one would expect the highest slope of the central phase response feature to be obtained at the lowest cavity power. This is not the case as will be shown below. As the system is highly non-linear the input power has a optinum value at which the slope is highest. For laser stabilisation purposes this slope is what should be optimized as it gives rise to a tighter lock.

In order to test this hypothesis we have taken some preliminary data for a wide range different probe powers using both conventional and sideband probing. The subsequent data analysis yielded the plot in figure 5.6. Each point is based on data from three frequency scans. A larger number of measurements are required to achieve better statistics. For comparison with the theoretical plot in figure 5.7, these measurement must be taken with a fixed number of atoms, which have been a challenge in the current experimental set-up. The implementation of the new repumper described in section 3.1, will thus contribute greatly to further power dependence measurements. In comparing figure 5.6 and 5.7 a similar trend is visible. However, the understanding of how to get an absolute phase calibration was at the time of these measurements inadequate. In order to fully compare the experimental data and theory, the absolute phase calculation in both cases have to be understood better.

5.2.2 Number Dependence

The original theory presented in [6], where $T = 0$, was based on non-linear effects involving a collective coupling of the atoms to the cavity field. Here the atomic dipoles acquired a global phase as they synchronize. This would entail a strong dependence of the phase response on the number of atoms, perhaps even a slope scaling of going as N^2. Exactly how this collective synchronisation affects the phase response is still an open question in our case. Never the less we have investigated the phase response as a function of the number of atoms in the cavity.

Figure 5.8 shows the central phase feature for four different numbers of atoms in the cavity mode N_{cav}. In the plots the experimental data have been scaled to fit the theoretical plots by multiplying the experimental data with an arbitrary conversion factor. The phase signal has a strong dependence on the number of atoms as cavity light experience greater phase shift as the number of atom increases. This leads to a larger slope around resonance. This scaling is linear and thus scales as usual saturated absorption, so any conclusions of collective effects can not by drawn. At the same time we can not conclude that collective effect are not present, as it is not yet clear how these effects manifests themselves in the phase response. The number of atoms is not an obvious optimization parameter as it associated with some technical difficulties to enhanced the number of atoms significantly.

5.2.3 Absolute Phase Calibration

In order to convert the NICE-OHMS signal into an absolute atom induced phase, a scan of the empty cavity is needed as described in chapter 4. The alignment of the cavity mirrors have great influence on the finesse of the cavity, which the NICE-OHMS signal very sensitive to. Due to primarily temperature drifts the finesse and other characteristics of the cavity undergo subtle changes over the course of a few hours. For an accurate phase calibration an empty cavity scan is thus required for every measurement session for a given set of system parameters.

Figure 5.9 shows data from the NICE-OHMS signal that has been converted to an absolute atom induced phase through the method described in section 4.3. Figure 5.10 shows the theoretical model's output for similar parameters. These two plot is in that way an absolute comparison of theory and data. It is evident that the amplitude of phase signal do not agree, as we see approximately a factor of 10 difference between the experimental data and the theory. This inconsistency can be based on different assumptions and approximations. As mentioned in section 4.3, the Taylor approximation greatly alters the sideband terms in equation (4.16). This could indeed have an effect on the slope used to determine the calibrations factor. If we compare figure 4.7 and 5.9 we see a clear indication that this calibration model is deficient. The calibration model calculates the possible output signal from the NICE-OHMS set-up to a minimum of -0.05 V and a maximum of 0.07 V corresponding to a phase of ± 0.02 radians. The raw data from the NICE-OHMS signal ranges from -0.2 V to 0.2 V, which is much greater than what the calibration model gives. Whether or not this all comes down to the Taylor approximation is hard to say.

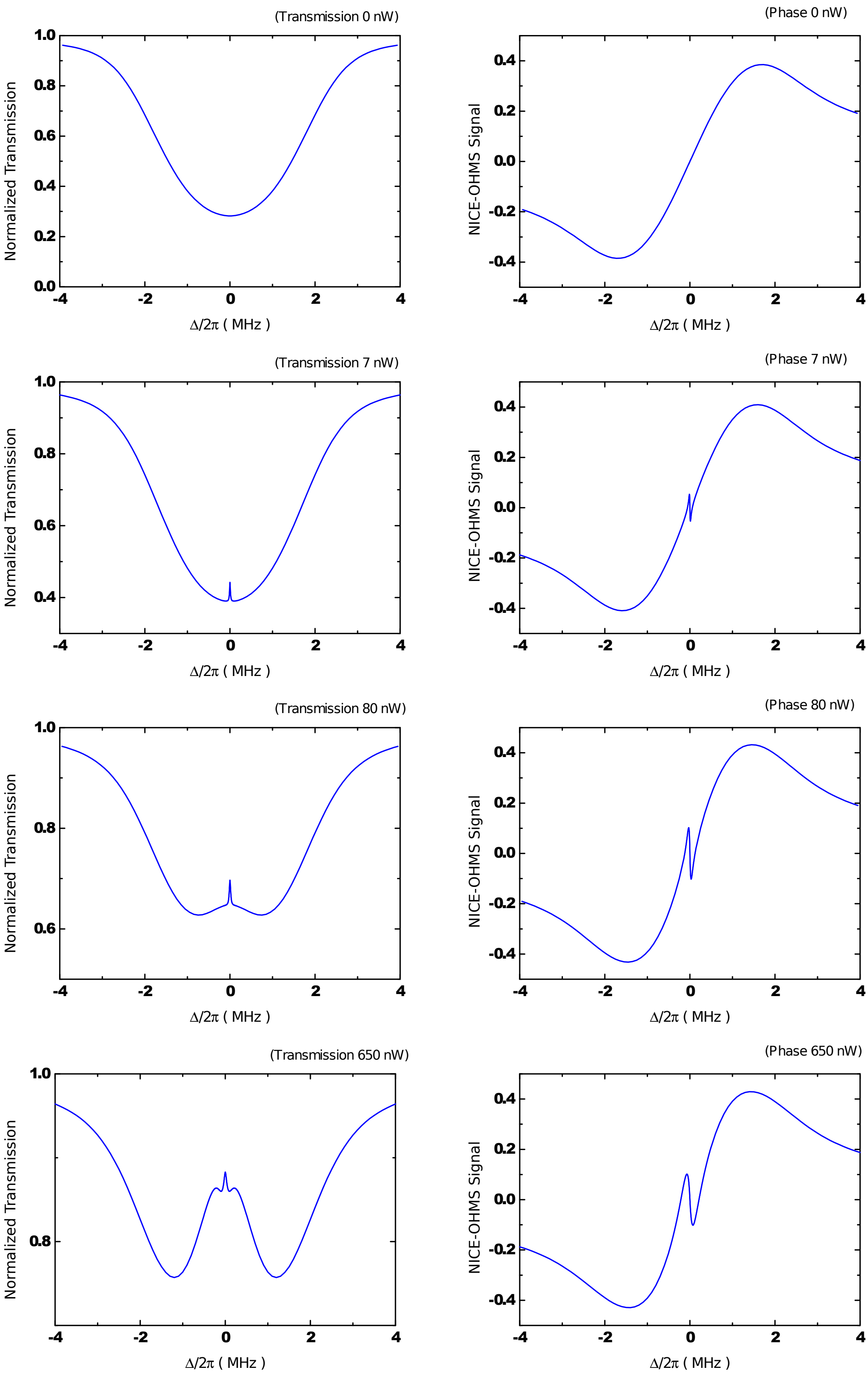

Figure 5.5: *Theoretical plots showing the change in transmission and phase signal as the input power is enhanced.*

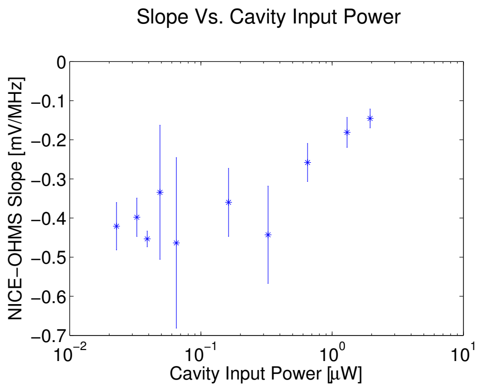

Figure 5.6: *A plot of the slope of the central phase feature for different cavity input powers. Each point is based on three frequency scans.*

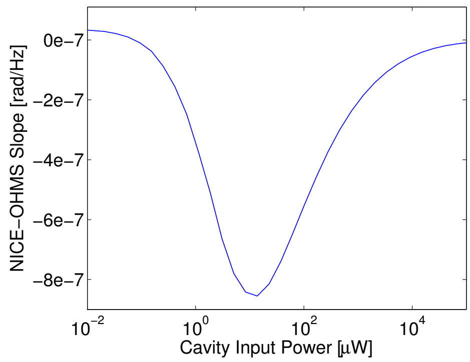

Figure 5.7: *The theoretical slope of the central feature of the phase signal versus the cavity input power.*

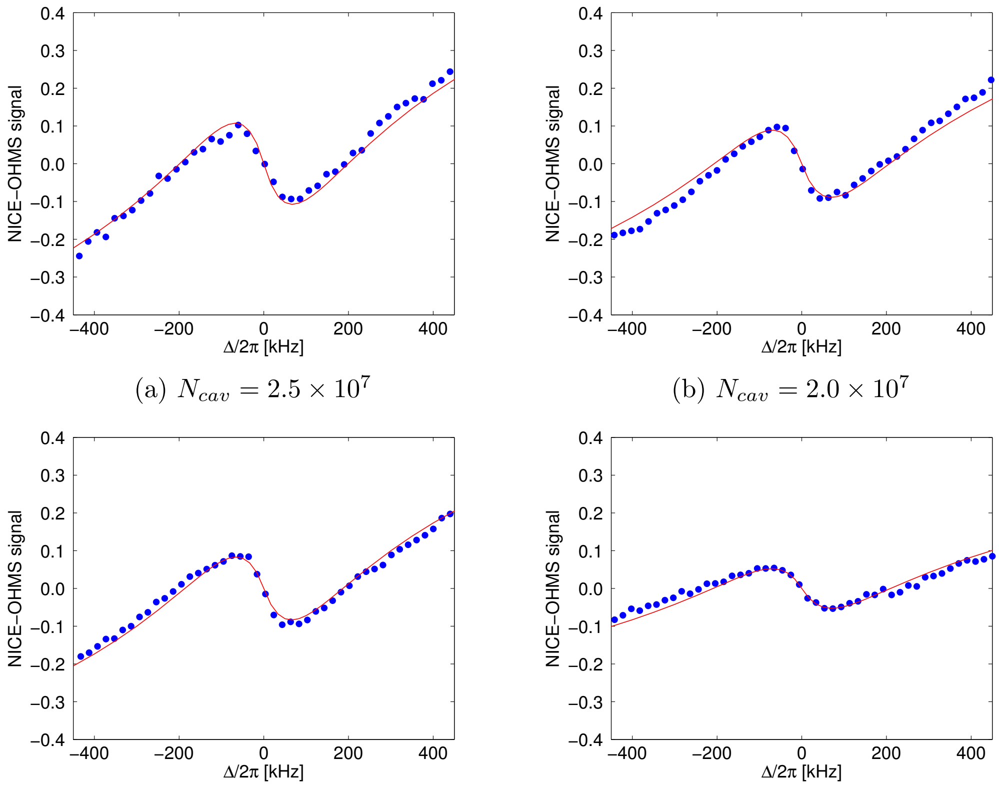

(a) $N_{cav} = 2.5 \times 10^7$

(b) $N_{cav} = 2.0 \times 10^7$

(c) $N_{cav} = 1.7 \times 10^7$

(d) $N_{cav} = 1.2 \times 10^7$

Figure 5.8: *Plots of data and theory for four different number of atoms in the cavity. The probe input power is fixed at 650 nW. The experimental data have been scaled to fit the theoretical plots.*

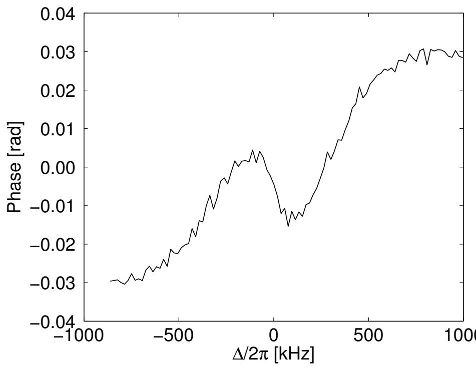

Figure 5.9: *Data of the NICE-OHMS signal converted to radians as described in section 4.3. The experimental parameters for this data are an input power of 1300 nW and 2.7 × 10*^{7} *atoms in the cavity.*

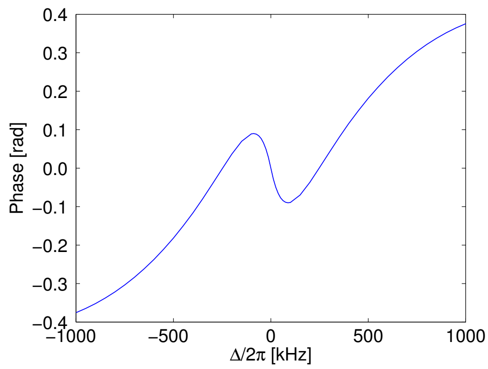

Figure 5.10: *A theoretical plot of the phase response where the parameters are an input power of 1300 nW and 2.7 × 10*^{7} *atoms in the cavity.*

Though the calibration of the NICE-OHMS signal leaves a lot to be desired, the theoretical model could also given an incorrect phase value. As mentioned, the theoretical model dose not account for the momentum change exerted on the atoms by the cavity photons. The consequences of the exclusion of this has not been investigated. The theoretical model also assumes that the populations of the exited and ground states are steady-state. The consequence of this is investigated in section 5.3.

5.3 Time Dependence

An assumption made in theoretical model is that the two level system being probed is in steady-state. To determine if this in fact is a valid assumption within the time scales of the experiment, the optical Bloch equations for a three level system is used to investigate the time evolution of the populations and coherences. These simulation are then compared to measurements of the NICE-OHMS signal's time evolution.

The optical Bloch equations are described in appendix E. Using a standard differential equation solving function in MATLAB the energy levels population evolution and their coherences are computed. In figure 5.11 the evolution of the interesting elements of the density matrix is shown for $\Delta = 0$ and $\Delta = 50$ kHz. The matrix element ρ_{22} corresponds to the population ratio of the $^1\mathrm{S}_0$ ground state and the matrix element ρ_{33} corresponds to the population ratio of the $^3\mathrm{P}_1$ state. The u and v parameters are defined as $u = \frac{1}{2}(\rho_{23} + \rho_{32})$ and $v = \frac{1}{2i}(\rho_{23} - \rho_{32})$

In these simulations the cavity field is constant through the process, calculated from and input cavity power of 325 nW. So the atomic effect on the intra-cavity field intensity is not taken into account. The MOT beams are turned on at $t = 0$ s and turned off at $t = 1$ ms. This time period is much smaller than the actual ≈ 800 ms of cooling and trapping time in the experiment, but as the system have reached steady-state after 1 ms, there is no point in simulating the full 800 ms. During the time where the MOT beams are on, the atom-cavity detuning is set to $\Delta + 2$ MHz to account for the AC-Stark effect. This frequency shift have been determined by comparing spectroscopy spectrum where the MOT beams are on and where they are off.

Looking at figure 5.11a and 5.11c it is evident that system is not in steady-state after 100 μs. Further more we see that the atoms are strongly saturated at $\Delta = 0$ as half the atoms are in the exited state and the other half is in the ground state.

From reading [22], we can deduce that u is proportional to the dispersion and v is proportional to the absorption. We can thus compare the evolution of these with what we actually measure. In figure 5.11b and 5.11d it is again evident that the system is not in steady-state. The dispersion (green curves) goes to zero at resonance as expected.

Though the system is clearly not in steady-state, the Rabi oscillation dose not have a significant effect. This is due to the interrogation period of 100 μs. In practise this means that we integrate the signal over 100 μs leading to a maximum frequency resolution of $1/(2 \cdot 100\ \mu\text{s})$. Near resonance the system's Rabi frequency is greater than the detection resolution, making it possible to neglect these oscillations.

In order to investigate what influence these population oscillations have on the NICE-OHMS signal, I performed a series of measurement. These measurements were made by taking the NICE-OHMS signal and feeding it to an oscilloscope instead of the computer in the experimental set-up. After setting the detuning the the experiment cycle was started and the evolution of the NICE-OHMS signal was recorded. The oscilloscope averaged the measurements of ≈ 60 experiment cycles (figure 2.15) for each detuning value. This was repeated for different detuning values until the central phase response feature was mapped out. Afterwards, the oscilloscope data was used to recreate the typical phase response spectrum, by integrating over a 100 μs starting at different times. Thus getting plots showing the evolution of the phase response signal for different probe delays. These measurements were done after the Pockels cell shutting technique (section 3.2.3) was implemented, but before the problem with the AOM VCOs was solved (section 3.3). In figure 5.12 the phase response corresponding to different probe delays is shown. Due to substantial noise in these measurement it is difficult see any signs of the atomic states population oscillations independent of the integration time chosen. We do however see that the signal reduces at long probe delays. This is consistent with what we expect as the number of atoms in the cavity get smaller with a longer probe delay.

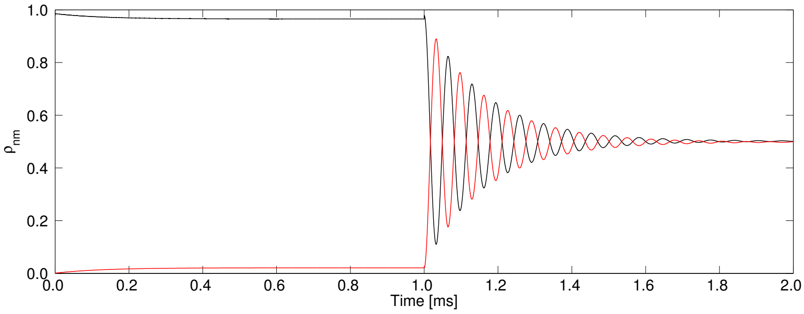

(a) *Time evolution of the* $^1S_0$ *state (black) and the* $^3P_1$ *state (red). Here the atom-cavity detuning is* $\Delta = 0$.

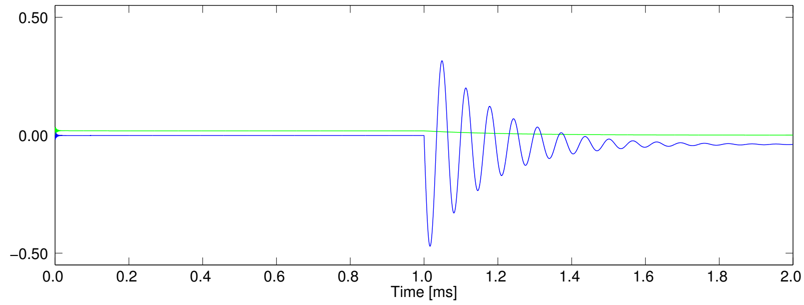

(b) *Time evolution of* u *(green) and* v *(blue). Here the atom-cavity detuning is* $\Delta = 0$.

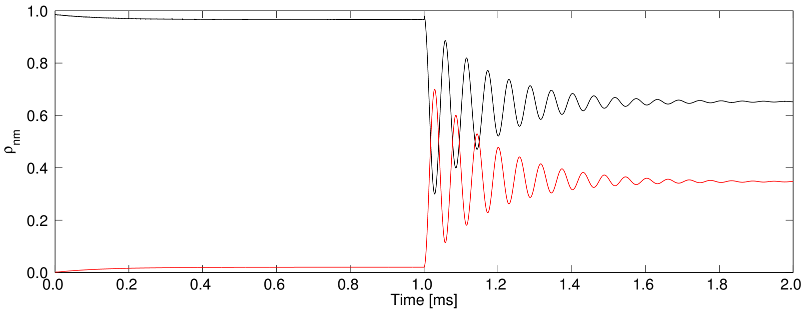

(c) *Time evolution of the* $^1S_0$ *state (black) and the* $^3P_1$ *state (red). Here the atom-cavity detuning is* $\Delta = 50$ *kHz.*

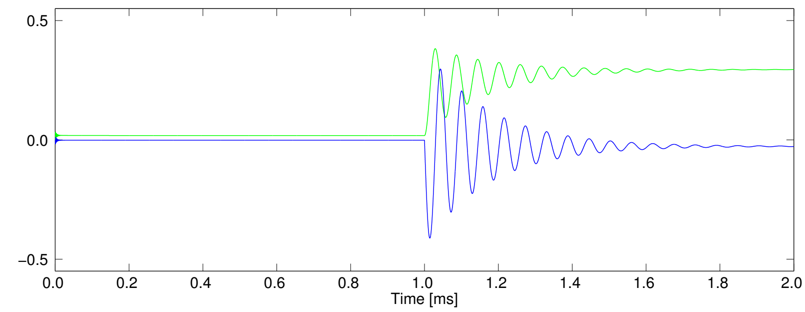

(d) *Time evolution of* u *(green) and* v *(blue). Here the atom-cavity detuning is* $\Delta = 50$ *kHz.*

Figure 5.11: *Solutions to the optical Bloch equations. The cavity input power is 325 nW.*

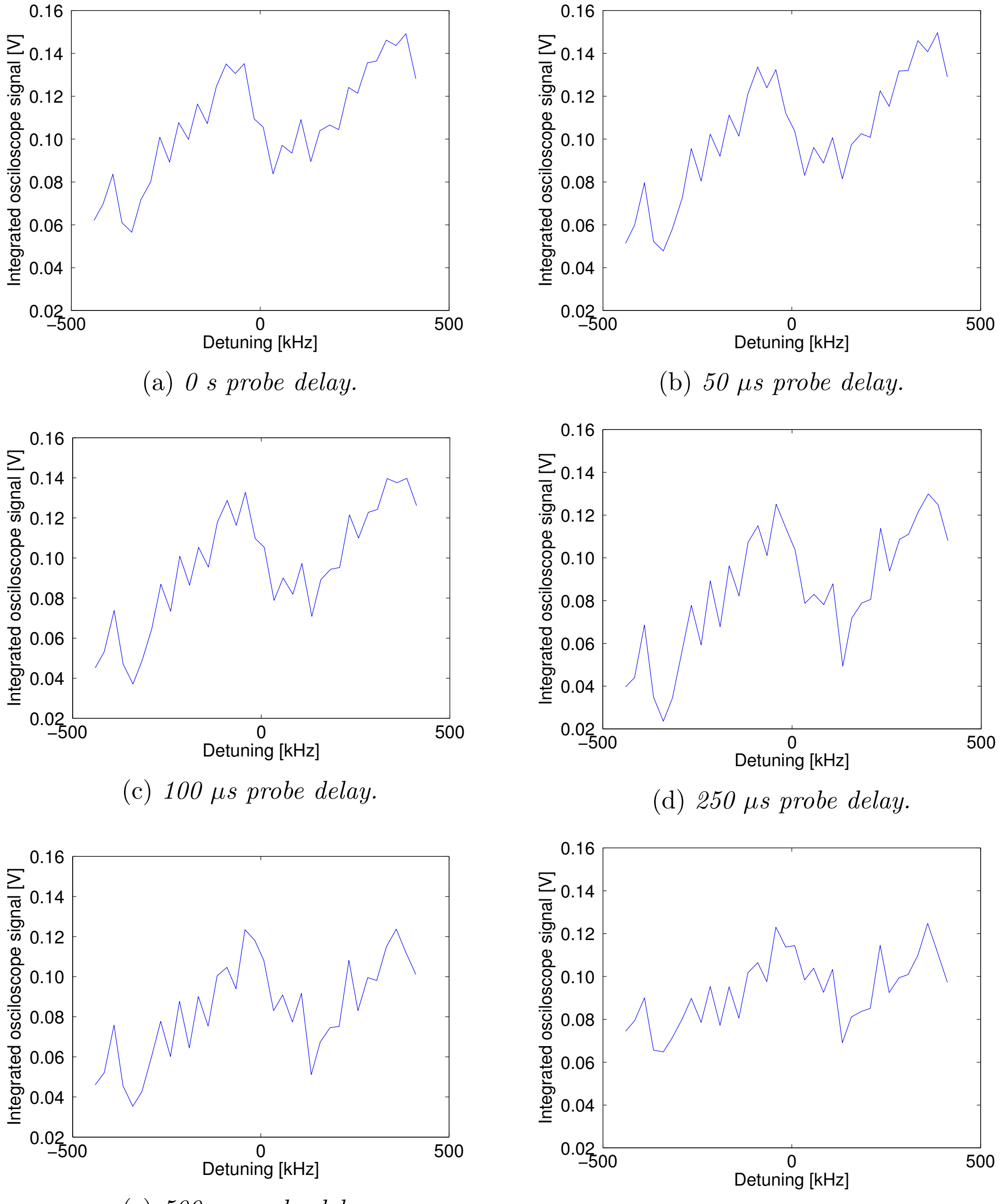

(a) *0 s probe delay.*

(b) *50 μs probe delay.*

(c) *100 μs probe delay.*

(d) *250 μs probe delay.*

(e) *500 μs probe delay.*

(f) *900 μs probe delay.*

Figure 5.12: *The evolution in probe delay values of the NCIE-OHMS signal.*

Chapter 6

Conclusion and Outlook

The work presented in this thesis has been concerned with the practical challenges and theory of cavity enhanced spectroscopy. This is motivated by the fact that the dispersion signal from atom-light interactions enhanced by a cavity provides an ideal error signal for a laser stabilisation scheme. As our understanding of the experimental system has grown, new areas of interest have emerged. As a result of this a number of new projects are under development.

6.1 Conclusion

The use of an ultra-narrow optical transition in Strontium has shown to have great potential as a possible locking scheme for future laser stabilisation. This is made possible by cavity enhanced FM spectroscopy where atomic phase response shows a resonance feature suited for application as an error signal. By use of the so-called NICE-OHMS technique a high signal-to-noise ratio is achieved. Presently the signal-to-noise ratio is 7000 at one second of integration. In comparison the directly measured transmission has a signal-to-noise ratio of only 400 at one second of integration. Furthermore a strong non-linear cavity power dependence of the phase response signal emphasizes the possibilities of a simple low finesse cavity set-up to deliver a tight locking scheme.

So far we have not seen clear evidence of collective effects where the atomic dipoles synchronise to form a macroscopic dipole. This would lead to system parameters, such as the phase response slope, depending non-linear on the number of involved atoms. We have found clear evidence that the slope of the phase response scales linearly with the number of atoms. A new theoretical model that accounts for a finite thermal distribution of the atoms, has shown new resonance features within the transmission spectrum, which can not be seen in the phase response.

An absolute measurement of the phase induced by the atoms in the cavity would be ideal for a detailed comparison between the theory and the experiment. The first comparison between the theory and the experiment was calibrated by an arbitrary factor to match the theoretical model. However, in this work a method to calibrate the absolute phase measurement via the empty cavity response has been develop. This calibration procedure is a non-trivial matter as it involves heavy mathematical expressions and could thus be improved through further analysis. One outcome of this analysis is the discovering of the possibility of using NICE-OHMS for measurements of the atomic absorption. This should make it possible to measure the transmission with the same signal-to-noise ratio currently achieved on the phase response signal.

As part of the experimental work a number of investigations into different aspects of the experimental set-up, have yielded the development of different parts all helping to improve the experimental performance. Among these is the development of a stable ECDL to be used as a repumper laser for the MOT. The goal of a 707 nm laser, with a minimum of mode jumps over an extended period of time, was achieved. As part of the ECDL a temperature stabilisation system was developed from scratch. This system successfully controlled the temperature fluctuations below 0.8 % of the uncontrolled version, minimising the temperature deviation of the ECDL mount to 0.548 mK. This small temperature drift contributes to the reduction of the ECDLs mode jumps.

One of the obvious future directions of the experiment would be to investigate time dependent effects, eventually the time dependence of synchronisation effects. In connection to this, different shutting mechanisms was investigate. A set-up using a Pockels cell was implemented in the experimental set-up, thus achieving effective shutting of the MOT beams within a few micro-seconds. Finally, a problem with frequency drift of the probe laser was identified to be caused by unstable VCOs driving the AOMs in the experimental set-up. This problem was rectified and a solution using a digital synthesizer was investigated.

6.2 Outlook

As shown in section 4.4, it is possible to obtain a NICE-OHMS signal proportional to the atomic absorption. This should give us the ability to detect the transmission signal with much greater signal-to-noise ratio than we have now. Hopefully this will make it possible to detect the Doppleron resonances directly.

The next step for the experimental set-up is the implementation of a high finesse cavity, thus going from a finesse of ≈ 65 to a finesse of 1000. In this new regime new physics is expected to appear as the collective cooperativity will be boosted with a factor of more than 100. One of things to investigate is possibility of superradiance. Here the atomic sample will be prepared in the exited state by a π-pulse. If the atoms are collectively synchronized via the cavity field, their collective phase should result in a coherent flash. In such a system we would expect a strong non-linear dependence on the number of atoms going as N^2. Superradiant effects have been reported in a Rb system in [23] and similar effects was recently reported as a superflash effect in a ^{88}Sr system in [24]. Similar to this, we expect collective effects to emerge as a result of the stronger atoms cavity field coupling in this system.

A laser stabilisation scheme using our current set-up would be limited by the Dick effect [25], as the cyclic manner in which it is operated gives a long dead time between measurements. A new set-up is under development where a beam of slowly moving atoms traverse a cavity field. This makes a continuous interrogation possible thus minimising the Dick effect. Furthermore, we could in this set-up investigate the possibilities of steady-state superradiant lasing. A necessity for superradiant lasing is an incoherent pumping mechanism for the atoms. This is difficult to achieve for a stationary atomic sample, but continuously feeding the cavity field with new exited atoms will correspond to an incoherent pumping.

Appendices

Appendix A

The MATLAB Script for Calculating Allan Deviation

A.1 Main Code

The main code for combining error signal data files and calculating the Allan deviation.

```
clear all
close all

% Parameters:
% omega_m is the Pound-Drever-Hall modulation frequency, d_omega is the laser frequency detuning,
% x_off is the x-axis off-set and A is an amplitude scaling parameter.

%Read data
error_cal=csvread('data130923/TEK00006.CSV');

d_omega_data = error_cal(:,1); %1516:5516
D_data = error_cal(:,2);

figure(1)
plot(d_omega_data, D_data)


% Guess for parameters: [omega_m Gamma A x_off y_off]
% gaet = [omega_m Gamma A x_off y_off]';
gaet = [0.0025 0.0001 -0.452 0.00592 -0.01]';

% Fitting. The fitted parameter is returned to x_fit. x and y data for the fitted curve is returned in error_fit. x and y data for the curve based on the guess-parameters is returned in error_gaet. The function errorSignalFitFunc() called in a separate script.
[x_fit error_fit error_gaet] = errorSignalFitFunc(gaet, [], [], [d_omega_data D_data]);

% Conversion of x-axis to hertz and centrering along the x-axis.
x_enhed = 10^7/(x_fit(1))
d_omega_data = (d_omega_data-x_fit(4)).*x_enhed;
D_data = D_data-x_fit(5);
error_fit(:,1) = (error_fit(:,1)-x_fit(5)).*x_enhed;
error_fit(:,2) = error_fit(:,2)-x_fit(4);
error_gaet(:,1) = (error_gaet(:,1)-x_fit(5)).*x_enhed;
error_gaet(:,2) = error_gaet(:,2)-x_fit(4);
```

```matlab

figure(3)
plot(d_omega_data, D_data)
hold on
grid on
plot(error_gaet(:,1), error_gaet(:,2), 'g')
plot(error_fit(:,1), error_fit(:,2), 'r')
set(gca,'Fontsize',12)
axis([-gaet(1)*x_enhed*1.6 gaet(1)*x_enhed*1.6 min(error_gaet(:,1))*1.6 max(error_gaet(:,1))*1.6]) % [x-min x-maks y-min y-maks]
xlabel('\Delta \omega [Hz]','Fontsize',14)
ylabel('Error signal [V]','Fontsize',14)
title('Dataset 2')

% Calculation of the slope at the centre of the error signal. a[V/Hz]
[min_val idx_0Hz] = min(abs(error_fit(:,2)));
linFit = fittype('a*x+b')
xLin = d_omega_data(idx_0Hz+2:idx_0Hz+7); % Here the data points included in the fit are choosen.
yLin = D_data(idx_0Hz+2:idx_0Hz+7);
g = [0 0];
[linFitError gof fitinfo] = fit(xLin,yLin,linFit,'StartPoint',g);
coef = coeffvalues(linFitError);
a = coef(1)
b = coef(2);
lin = a*d_omega_data(idx_0Hz-200:idx_0Hz+200)+b;

% This is a different method to find the slope using the differentiated error signal fit.
% diff_error_fit = diff(error_fit(:,1)) ./ diff(error_fit(:,2));
% a = min(diff_error_fit);

figure(2)
plot(d_omega_data(idx_0Hz-200:idx_0Hz+200)*10^-6, D_data(idx_0Hz-200:idx_0Hz+200),'black')
hold on
plot(d_omega_data(idx_0Hz+2:idx_0Hz+7)*10^-6, D_data(idx_0Hz+2:idx_0Hz+7),'LineWidth',2)
plot(d_omega_data(idx_0Hz-200:idx_0Hz+200)*10^-6,lin,'--r','LineWidth',2)
axis([-0.15 0.15 -0.6 0.6])
set(gca,'Fontsize',16)
n=get(gca,'xtick');
set(gca,'xticklabel',sprintf('%.2f |',n'))
xlabel('\Delta \omega [MHz]','Fontsize',16)
ylabel('Error signal [V]','Fontsize',16)
title('Linear Slope Fit','Fontsize',18)

format long
linFitError

%%
% ------ Read Data ------

% Data files are numbered in series, this sets the number of the first data and last data file to be included in the Allan deviation:
n_start = 7;
n_slut = 16;

% Read in data
sti = 'data130923/' % Filepath to data files.
```

```
for n = n_start:n_slut
  i = n + 1 - n_start;
  if n < 10
    filnavn = [sti 'TEK0000' num2str(n) '.CSV']; % Sets filename to be
        read.
  else
    filnavn = [sti 'TEK000' num2str(n) '.CSV'];
  end
  data{i} = csvread(filnavn);
  freq{i} = data{i}(:,2);
end

% Sets the length of the array containing the combined data.
lfreq = 0;
for j = 1:(n_slut-n_start+1)
  lfreq = lfreq + length(freq{j});
end

% Combines data into one array.
freq_samlet = zeros(lfreq,1);
for i = 1:(n_slut-n_start+1)
  if i == 1
    sta = 1;
  else
    sta = sta + length(freq{i-1});
  end
  freq_samlet(sta:sta+length(freq{i})-1) = freq{i}(:);
end

% Creates time array.
d_tid = abs(data{1}(2,1) - data{1}(1,1));
t_slut = d_tid * lfreq;
tid_samlet = [0:d_tid:t_slut-d_tid]';


%%
% ------ Conversion of Data From Volts to Hertz ------

freq_data = [tid_samlet,freq_samlet];
freq_data(:,2) = freq_data(:,2)./a;
freq_data(:,1) = freq_data(:,1) - freq_data(1,1);

figure(4)
plot(freq_data(:,1),freq_data(:,2)*10^-3)
hold on
% grid on
axis([0 0.95 -13 13])
set(gca,'Fontsize',16)
xlabel('Time [s]','Fontsize',16)
ylabel('Frekvens [kHz]','Fontsize',16)
title('Error Signal Under Lock', 'Fontsize', 18)


%%
% ------ Allan Deviation ------

[t_maks n_data] = max(freq_data(:,1));
n = floor(log(n_data)/log(2));
n_freq = 2^n;
freq_var = freq_data(1:n_freq,2);%./a+2000; % [Hz]

```

```
allanDevi = zeros(n-1,2);

for i = 1:n-1
  nKlump = n_freq/(2^i);
  means = 0;
  y = zeros(nKlump,1);
  for j = 0:nKlump-1
    yStart = 2^i*j+1;
    ySlut = 2^i*(j+1);
    y(j+1) = mean(freq_data(yStart:ySlut,2)); %/freq_data(2^i+1,1);
  end
  for j = 1:nKlump-1
    means = means + 0.5*(y(j+1)-y(j))^2/(nKlump-1);
  end

  allanDevi(i,1) = freq_data(2^i+1,1);
  allanDevi(i,2) = sqrt( means );
end

figure(5)
loglog(allanDevi(:,1) , allanDevi(:,2), '-*');
grid on
hold on
set(gca,'Fontsize',15)
xlabel('\tau [s]','Fontsize',15)
ylabel('Allan Deviation [Hz]','Fontsize',15)
title('Frequency Stability', 'Fontsize', 17)
```

A.2 errorSignalFitFunc()

This is the function used to fit the error signal frequency scan to equation (2.30).

```
function [ x error_fit error_gaet ] = errorSignalFitFunc( X0, lb, ub,
    error_data)
%ERRORSIGNALFITFUNC Riehle bog kapitel 9.2.2
% Argumenter:
% X0 containes the guesses on parameters [omega_m Gamma A x_off y_off],
     where lb
% and ub are arrays containing lower and uppe bounds.
% error_data conaines x-data in column 1 and y-data in column 2.

d_omega_data = error_data(:,1);
D_data = error_data(:,2);

x = lsqnonlin(@errorFunc, X0, lb, ub, [], d_omega_data, D_data);

error_fit(:,1) = d_omega_data;
error_fit(:,2) = errorFunc(d_omega_data, x(1), x(2), x(3), x(4), x(5));
error_gaet(:,1) = d_omega_data;
error_gaet(:,2) = errorFunc(d_omega_data, X0(1), X0(2), X0(3), X0(4),
    X0(5));

end
```

A.3 errorFunc()

This is the MATLAB function that returns equation (2.30).

```
function [ diff ] = errorFitFunc( x, d_omega_data, D_data )

omega_m = x(1);
Gamma = x(2);
A = x(3);
x_off = x(4);
y_off = x(5);

diff = y_off + A * omega_m.^2 .* Gamma/2 .* (d_omega_data-x_off) .* ...
    ((Gamma/2)^2 - (d_omega_data-x_off).^2 + omega_m.^2) ./ ...
    ( ((d_omega_data-x_off).^2 + (Gamma/2)^2) .* (((d_omega_data-x_off)
        + omega_m).^2 + ...
    (Gamma/2)^2) .* (((d_omega_data-x_off) - omega_m).^2 + (Gamma/2)^2)
        ) - D_data;

end
```

Appendix B

Raspberry Pi DAC/ADC Circuit

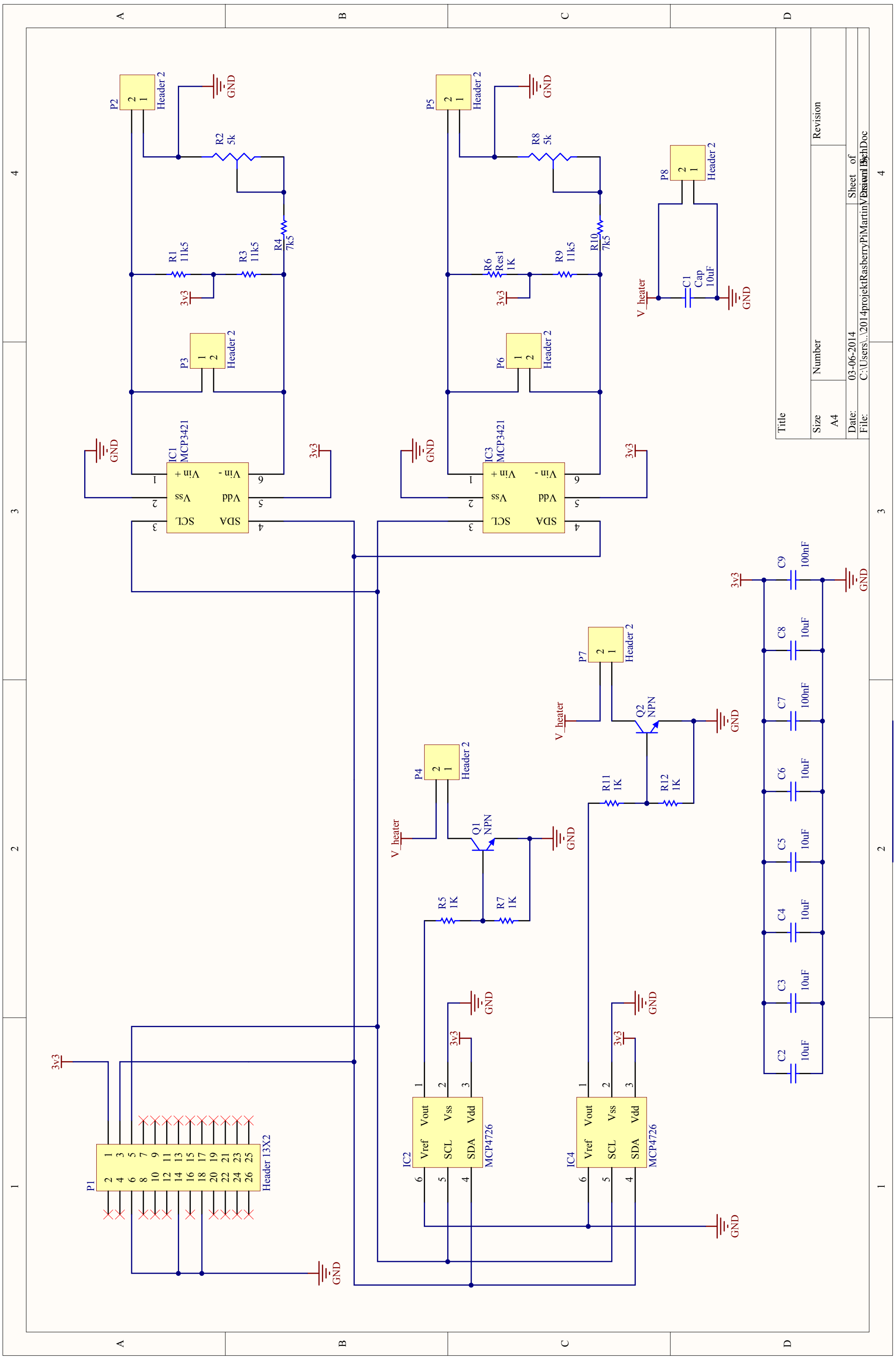

P1
Header 13X2
P2
Header 2
P3
P4
P5
P6
P7
P8
R1
11k5
R2
5k
R3
11k5
R4
7k5
R5
1K
R6
Res1
R7
R8
R9
R10
R11
R12
IC1
MCP3421
IC2
MCP4726
IC3
IC4
Q1
NPN
Q2
C1
Cap
10uF
C2
C3
C4
C5
C6
C7
100nF
C8
C9
GND
3v3
V_heater
Vin +
Vin -
Vss
Vdd
SCL
SDA
Vout
Vref
Title
Size
A4
Number
Revision
Date:
03-06-2014
File:
Sheet of
Drawn By:

Appendix C

Program Code for PID Temperature Controller of ECDL Mount

C.1 Main Code

The main code of the python program for PID-control.

```
#!/usr/bin/python

from DAC_ADC_pi import PiTemp
from discretePID import PID
from math import log
import time
import os
import matplotlib.pyplot as plt
import matplotlib.lines as Line2D
from collections import deque

def voltage2temp(voltage):
    R3 = R1 = 10000
    R2 = 9900
    V_DD = 3.3
    U = -voltage

    R_T = -R3*(R1*U + R2*U - R2*V_DD)/(R1*U + R1*V_DD + R2*U)
    #print('R_T: %02f' % R_T)

    a = 3.354017E-3
    b = 2.5617244E-4
    c = 2.1400943E-6
    d = -7.2405219E-8
    R_25C = 10000
    T = 1/(a + b*log(R_T/R_25C) + c*log(R_T/R_25C)*log(R_T/R_25C) + d*
        log(R_T/R_25C)*log(R_T/R_25C)*log(R_T/R_25C))-273.15

    return T

def printVar(CH,servo,outputVoltage):
    if (CH.getChannel()==1):
        print('Channel 1')
    if (CH.getChannel()==2):
        print('Channel 2')
```

```

    print('----------------------------------------')
    #print ("Input Voltage: %02f V" % CH.readVoltage())
    print ("Temperature: %02f Celsius" % voltage2temp(CH.readVoltage()))
    print ("Output voltage: %02f V" % outputVoltage)
    print ("Error: %02f V" % servo.getError())
    print ("PID value: %02f V" % servo.getPID())
    print (' ')
    print (' ')

def temperatureControl(CH,servo,plotArray,curve,plot):
            currentTemperature = CH.readVoltage()
            pidVal = servo.update(currentTemperature)
            error = servo.getError()

            outputVoltage = 1.85 + pidVal    # When output is at >2.6 V the current
                                             # thrugh the heater is 0 mA and when
                                             # the output is < 0.9 V the heatercurrent
                                             # is ~350 mA.
            CH.setVoltage(outputVoltage)

            realTemp = voltage2temp(currentTemperature)

            if (plot):
                plotTimeStart = time.time()
                if (len(plotArray)>99):
                    plotArray.popleft()

                plotArray.append(realTemp)
                curve.clear()
                curve.plot(plotArray)
                plt.draw()
                plotTime = time.time()-plotTimeStart
                #print plotTime
                wait = 4-plotTime
                if (wait>0):
                    time.sleep(wait)
                j=0

            return outputVoltage


def main():
    # DAC and ADC initialization of channel 1 and 2
    ch1 = PiTemp(1)
    ch2 = PiTemp(2)

    # Plotting parameters
    plot = False
    startTemp1 = voltage2temp(ch1.readVoltage())
    startTemp2 = voltage2temp(ch2.readVoltage())
    array1 = deque([startTemp1]*50)
    array2 = deque([startTemp2]*50)
    fig = plt.figure()
    curve1=fig.add_subplot(2,1,1)
    curve2=fig.add_subplot(2,1,2)
    if (plot):
```

```
        plt.title('Title')
        plt.ion()
        plt.ylim([-0.3,0.3])

    # PID parameters
    p1 = PID(750,4,170) # (P,I,D) 750,10,450
    p1.setPoint(0.0)# If the pot-meter is set correctly, the ADC will give 0 V
                    # at 10,63 Ohm thermistor resistence, corresponding to
                    # ~24 degress celsius.

    p2 = PID(1.0,0.0,0.0)
    p2.setPoint(0.0)

    t_start = time.clock()

    while (True):
        try:
            tStart = time.time()
            output1 = temperatureControl(ch1,p1,array1,curve1,plot)
            tDone = time.time() - tStart
            wait = 1-tDone
            #print(tDone)
            if (wait>0):
                    time.sleep(wait)

            output2 = temperatureControl(ch2,p2,array2,curve2,plot)
            if (wait>0):
                time.sleep(wait)

            # clear the console
            os.system('clear')
            printVar(ch1,p1,output1)
            printVar(ch2,p2,output2)
        except KeyboardInterrupt:
            print 'Exiting'
            break


if __name__ == '__main__':
    main()
```

C.2 DAC/ADC Communication

This section contains the code where the function used to communicated with the MCP3421 and MCP4725 chip is defined. The protocol used is the I^2C.

```
#!/usr/bin/python

import smbus
import re

class PiTemp :
  # internal variables

  __addressADC = 0x68 # address for MCP3421A0
```

```
__addressADC = 0x69 # address for MCP3421A1
__configADC = 0x8f # PGAx8, 18 bit, one-shot conversion
__DACwriteReg = 0x40 # Register for DAC (MCP4725)
__maxDAC = 3.3 # Maximum output voltage equal to Vdd.
__lsb = 0.000015625 # default lsb value for 18 bit
CH = 0

# create byte array and fill with initial values to define size
__adcreading = bytearray()
__adcreading.append(0x00)
__adcreading.append(0x00)
__adcreading.append(0x00)
__adcreading.append(0x00)

# Define I2C bus and init. For Raspberry PI model B, I2C bus is 1.
global bus
bus = smbus.SMBus(1);

def __checkPGA(self, configByte): # To check which multiplication factor the PGA uses.
  if (configByte & 2):
    if (configByte & 1):
      return 8
    else:
      return 4
  else:
    if (configByte & 1):
      return 2
    else:
      return 1

def __init__(self,channel):
  self.CH = channel
  if (channel == 1):
    self.__addressADC = 0x68 # address for MCP3421A0
    self.__addressDAC = 0x62 # address for MCP4725A1
    bus.write_byte(self.__addressADC, self.__configADC)
  elif (channel == 2):
    self.__addressADC = 0x69 # address for MCP3421A1
    self.__addressDAC = 0x64 # address for MCP4725A2
  else:
    return 0

def readVoltage(self):
  t = 0.0

  __adcreading = bus.read_i2c_block_data(self.__addressADC,self.__configADC)
  h = __adcreading[0] # databit 17 (MSB) and 16
  m = __adcreading[1] # databit 15 to 8
  l = __adcreading[2] # databit 7 to 0
  s = __adcreading[3] # configuration byte

  pga = self.__checkPGA(s)
  # print pga

  t = ((h & 0b00000001) << 16) | (m << 8) | l # converting form binary

  if (h & 2): # if MSB is 1 measured voltage it negative.
    return -(131070-t)*self.__lsb/pga # conversion to voltage
```

```
    else:
      return t*self.__lsb/pga

  def setVoltage(self, volt):
    if (volt > 3.3):
        volt = 3.3
    if (volt < 0):
        volt = 0

    val = int(round(volt/(self.__maxDAC/4095)))
    data = [(val >> 4) & 0xFF, (val << 4) & 0xFF]
    bus.write_i2c_block_data(self.__addressDAC, self.__DACwriteReg,
        data)

  def getChannel(self):
    return self.CH
```

C.3 PID-code

This section contains the function that calculate the PID output value based on the temperature measured by the thermistor. This code is written another who put up on the code sharing site github.com for others to use freely [26]. I have made small altercations to the code.

```
#The recipe gives simple implementation of a Discrete Proportional-
    Integral-Derivative (PID) controller. PID controller gives output
    value for error between desired reference input and measurement
    feedback to minimize error value.
#More information: http://en.wikipedia.org/wiki/PID_controller
#
#cnr437@gmail.com
#
####### Example #########
#
#p=PID(3.0,0.4,1.2)
#p.setPoint(5.0)
#while True:
#     pid = p.update(measurement_value)
#
#


class PID:
  """
  Discrete PID control
  """

  def __init__(self, P=2.0, I=0.0, D=1.0, Derivator=0, Integrator=0,
      Integrator_max=500, Integrator_min=-500):

    self.Kp=P
    self.Ki=I
    self.Kd=D
    self.Derivator=Derivator
    self.Integrator=Integrator
    self.Integrator_max=Integrator_max
    self.Integrator_min=Integrator_min
```

```

        self.set_point=0.0
        self.error=0.0

    def update(self,current_value):
        """
        Calculate PID output value for given reference input and feedback
        """

        self.error = self.set_point - current_value

        self.P_value = self.Kp * self.error
        self.D_value = self.Kd * ( self.error - self.Derivator)
        self.Derivator = self.error

        self.Integrator = self.Integrator + self.error

        if self.Integrator > self.Integrator_max:
            self.Integrator = self.Integrator_max
        elif self.Integrator < self.Integrator_min:
            self.Integrator = self.Integrator_min

        self.I_value = self.Integrator * self.Ki

        self.PID = self.P_value + self.I_value + self.D_value

        return self.PID

    def setPoint(self,set_point):
        """
        Initilize the setpoint of PID
        """
        self.set_point = set_point
        self.Integrator=0
        self.Derivator=0

    def setIntegrator(self, Integrator):
        self.Integrator = Integrator

    def setDerivator(self, Derivator):
        self.Derivator = Derivator

    def setKp(self,P):
        self.Kp=P

    def setKi(self,I):
        self.Ki=I

    def setKd(self,D):
        self.Kd=D

    def getPoint(self):
        return self.set_point

    def getError(self):
        return self.error

    def getIntegrator(self):
        return self.Integrator

    def getDerivator(self):
```

```
    return self.Derivator

  def getPID(self):
                return self.PID
```

Appendix D

Diagram of Driving Circuit for the Mechanical Shutter

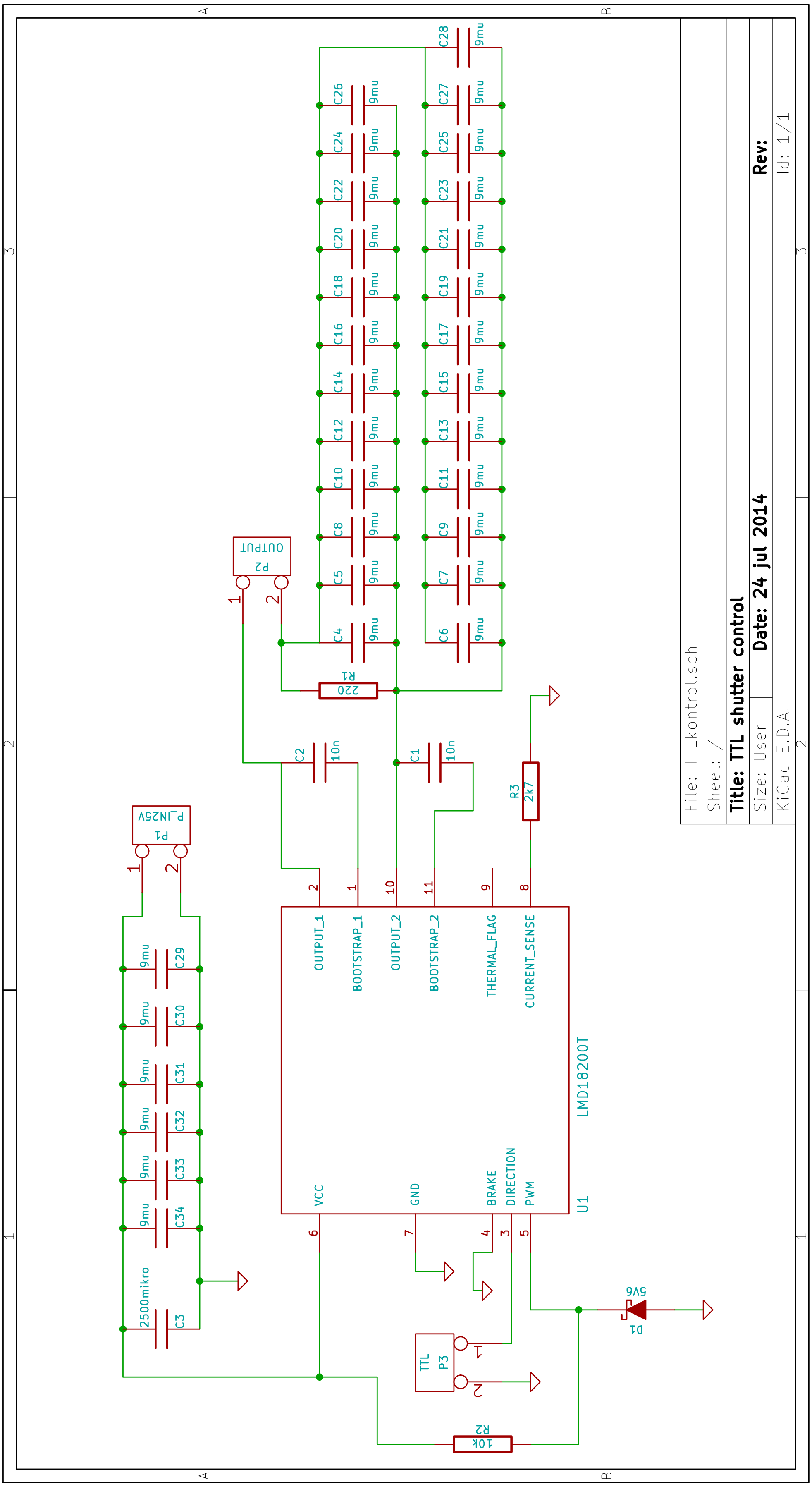
File: TTLkontrol.sch
Sheet: /
Title: TTL shutter control
Size: User
Date: 24 jul 2014
KiCad E.D.A.
Rev:
Id: 1/1
LMD18200T
U1
OUTPUT_1
BOOTSTRAP_1
OUTPUT_2
BOOTSTRAP_2
THERMAL_FLAG
CURRENT_SENSE
VCC
GND
BRAKE
DIRECTION
PWM
P1
P_IN25V
P2
OUTPUT
P3
TTL
R1
220
R2
10k
R3
2k7
D1
5V6
C1
10n
C2
10n
C3
2500mikro
9mu

Appendix E

The Optical Bloch Equation

The interaction that the theoretical model describes is a simple two-level system. However, in order to get a precise picture of the time evolution in our experiment the cooling transition has to be included. The time evolution of the density matrix describing the level structure in figure E.1 is computed through nine coupled differential equations, one for each matrix element. These differential equation are called the Optical Bloch Equations (OBE).

The time evolution of the density matrix ρ can be found using Liouville's Theorem

$$\frac{\partial}{\partial t}\rho_{nm} = -\frac{i}{\hbar}\langle n| [H, \rho] |m\rangle , \tag{E.1}$$

where the semiclassically Hamiltonian is given as

$$H = H_\circ + H_{int}. \tag{E.2}$$

Here $H_\circ$ describes the unperturbed state of the three level atom

$$H_\circ = \hbar\omega_1 |1\rangle\langle 1| + \hbar\omega_2 |2\rangle\langle 2| + \hbar\omega_3 |3\rangle\langle 3| \tag{E.3}$$

and H_{int} describes the interaction with a classical electric field oscillating as $E(\mathbf{r}, t) = \mathbf{E}(\mathbf{r})\cos(\omega t)$

$$H_{int} = e\mathbf{r}\cdot\mathbf{E_I}(\mathbf{r})\cos(\omega_I t) + e\mathbf{r}\cdot\mathbf{E_{II}}(\mathbf{r})\cos(\omega_{II} t), \tag{E.4}$$

where e is the charge of the electron.

In [27] the derivation leading to the OBE is carried though ending up with these

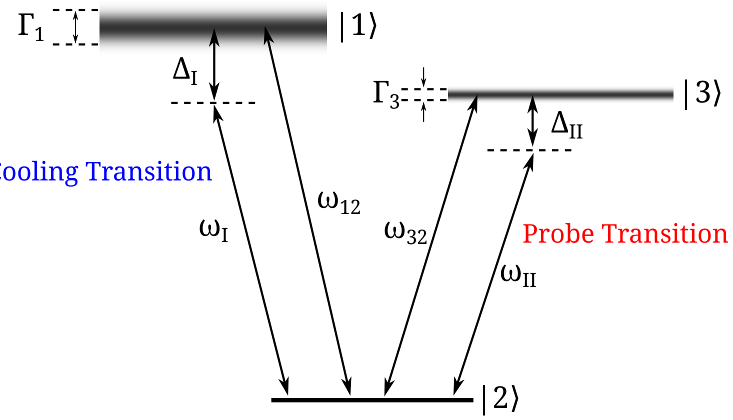

Figure E.1: *The level structure of the three level system to be described by the OBE. The* $|1\rangle$ *state and the* $|3\rangle$ *state corresponds respectively to the* $^1P_1$ *level and the* $^3P_1$ *level in* ^{88}Sr*. The* $|2\rangle$ *state corresponds to the* $^1S_0$ *ground state.*

coupled differential equations

$$\begin{aligned}
\dot{\rho}_{11} =& i\frac{\Omega_I}{2}(\rho_{21}-\rho_{12}) - \Gamma_1\rho_{11} \\
\dot{\rho}_{22} =& -i\frac{\Omega_I}{2}(\rho_{21}-\rho_{12}) - i\frac{\Omega_{II}}{2}(\rho_{23}-\rho_{32}) + \Gamma_1\rho_{11} + \Gamma_3\rho_{33} \\
\dot{\rho}_{33} =& i\frac{\Omega_{II}}{2}(\rho_{23}-\rho_{32}) - \Gamma_3\rho_{33} \\
\dot{\rho}_{21} =& i\Delta_I\rho_{21} - i\frac{\Omega_I}{2}(\rho_{22}-\rho_{11}) + i\frac{\Omega_{II}}{2}\rho_{31} - \frac{1}{2}\rho_{21}\Gamma_1 \\
\dot{\rho}_{12} =& -i\Delta_I\rho_{12} + i\frac{\Omega_I}{2}(\rho_{22}-\rho_{11}) - i\frac{\Omega_{II}}{2}\rho_{13} - \frac{1}{2}\rho_{12}\Gamma_1 \\
\dot{\rho}_{23} =& i\Delta_{II}\rho_{23} - i\frac{\Omega_{II}}{2}(\rho_{22}-\rho_{33}) + i\frac{\Omega_I}{2}\rho_{13} - (\frac{1}{2}\Gamma_3 + \Gamma_l)\rho_{23} \\
\dot{\rho}_{32} =& -i\Delta_{II}\rho_{32} + i\frac{\Omega_{II}}{2}(\rho_{22}-\rho_{33}) - i\frac{\Omega_I}{2}\rho_{31} - (\frac{1}{2}\Gamma_3 + \Gamma_l)\rho_{32} \\
\dot{\rho}_{13} =& -i(\Delta_I - \Delta_{II})\rho_{13} + i\frac{\Omega_I}{2}\rho_{23} - i\frac{\Omega_{II}}{2}\rho_{12} - \frac{1}{2}\rho_{13}(\Gamma_1 + \Gamma_3) \\
\dot{\rho}_{31} =& i(\Delta_I - \Delta_{II})\rho_{31} - i\frac{\Omega_I}{2}\rho_{32} + i\frac{\Omega_{II}}{2}\rho_{21} - \frac{1}{2}\rho_{31}(\Gamma_1 + \Gamma_3)
\end{aligned}$$

Bibliography

[1] T Kessler et al. "A sub-40-mHz-linewidth laser based on a silicon single-crystal optical cavity". In: *Nature Photonics* 6.10 (2012), pp. 687–692.

[2] J. J. O'Connor and E. F. Robertson. *Regnier Gemma Frisius*. 2002. URL: `http://www-history.mcs.st-and.ac.uk/Biographies/Gemma_Frisius.html`.

[3] Fritz Riehle. *Frequency Standards: Basics and Applications*. Wiley-VCH, 2004.

[4] *BIPM, Resolution 1 of the 13th Conférence Générale des Poids et Mesures (CGPM)*. 1967.

[5] BJ Bloom et al. "An optical lattice clock with accuracy and stability at the 10-18 level". In: *Nature* (2014).

[6] M. J. Martin et al. "Extreme Nonlinear Response of Ultranarrow Optical Transitions in Cavity QED for Laser Stabilization". In: *Physical Review A (Atomic, Molecular and Optical Physics)* 84.6 (2011), p. 063813. ISSN: 1050-2947. DOI: `10.1103/PhysRevA.84.063813`.

[7] Jun Ye, Long-Sheng Ma, and John L Hall. "Ultrasensitive detections in atomic and molecular physics: demonstration in molecular overtone spectroscopy". In: *JOSA B* 15.1 (1998), pp. 6–15.

[8] Xinye Xu et al. "Cooling and trapping of atomic strontium". In: *JOSA B* 20.5 (2003), pp. 968–976.

[9] Christopher J. Foot. *Atomic Physics*. Oxford University Press Inc., 2008.

[10] Rastin Matin. "Towards Continuous Cavity-Enhanced Nonlinear Spectroscopy in Strontium". MA thesis. The Niels Bohr Institute, University of Copenhagen, 2013.

[11] Xinye Xu et al. "Single-Stage Sub-Doppler Cooling of Alkaline Earth Atoms". In: *Phys. Rev. Lett.* 90 (19 2003), p. 193002. DOI: `10.1103/PhysRevLett.90.193002`. URL: `http://link.aps.org/doi/10.1103/PhysRevLett.90.193002`.

[12] T. W. Hansch and B. Couillaud. "Laser frequency stabilization by polarization spectroscopy of a reflecting reference cavity". In: *Optics Communications* 35.3 (1980), pp. 441–444.

[13] Eric D Black. "An introduction to Pound–Drever–Hall laser frequency stabilization". In: *American Journal of Physics* 69.1 (2001), pp. 79–87.

[14] Cunyun Ye. *Tunable External Cavity Diode Lasers*. World Scientific Publishing, 2004.

[15] L. P. Maguire, S. Szilagyi, and R. E. Scholten. "High performance laser shutter using a hard disk drive voice-coil actuator". In: *Rev. Sci. Instrum.* 75.9 (2004).

[16] B.E.A. Saleh and M.C. Teich. *Fundamentals of Photonics*. Wiley Series in Pure and Applied Optics. Wiley, 2007. ISBN: 9780471358329.

[17] Peter W. Milonni and Joseph H. Eberly. *Laser Physics*. Wiley, 2010. ISBN: 9780470409701.

[18] Jun Ye and Theresa W Lynn. “Applications of optical cavities in modern atomic, molecular, and optical physics”. In: *Advances in Atomic, Molecular, and Optical Physics* 49 (2003), pp. 1–83.

[19] Philip G. Westergaard et al. “Observing of Motion-Dependent Nonlinear Dispersion with Narrow Linewidth Atoms in an Optical Cavity”. Submitted to Nature Physics. 2014.

[20] Erkki Kyröla and Stig Stenholm. “Velocity tuned resonances as multi-Doppleron processes”. In: *Optics Communications* 22.2 (1977), pp. 123–126.

[21] Andrée Tallet. “Raman emission versus dopplerons in a two-level atomic cell”. In: *JOSA B* 11.8 (1994), pp. 1336–1349.

[22] Mikhail et al. Lukin. *Lecture Notes for Quantum Optics 2*.

[23] Justin G Bohnet et al. “A steady-state superradiant laser with less than one intracavity photon”. In: *Nature* 484.7392 (2012), pp. 78–81.

[24] Chang Chi Kwong et al. “Cooperative emission of a coherent superflash of light”. In: *arXiv preprint arXiv:1405.5413* (2014).

[25] Philip Westergaard, Jerome Lodewyck, and Pierre Lemonde. “Minimizing the Dick effect in an optical lattice clock”. In: *Ultrasonics, Ferroelectrics and Frequency Control, IEEE Transactions on* 57.3 (2010), pp. 623–628.

[26] Unknown author. *Discrete PID control*. 2012. URL: `https://github.com/daltonrenaldo/berea_flight/blob/master/pid.py`.

[27] Per Lunnemann Hansen. “Experimental Determination of Metastable $^3P_1$ in Magnesium”. MA thesis. The Niels Bohr Institute, University of Copenhagen, 2006.